

# **Influence of Fuel Introduction Parameters on the Reactivity and Oxidation Process of Soot from a Gasoline Direct Injection Engine**

by

Jordan E. Easter

A dissertation submitted in partial fulfillment  
of the requirement for the degree of  
Doctor of Philosophy  
(Mechanical Engineering)  
in The University of Michigan  
2018

Doctoral Committee:

Professor Andre Boehman, Co-Chair  
Research Scientist Stani Bohac, Co-Chair  
Professor Herek Clack  
Jim Daley, Fiat Chrysler Automotive  
Research Scientist John Hoard  
Professor Angela Violi

Jordan E. Easter

[jeeaster@umich.edu](mailto:jeeaster@umich.edu)

ORCID iD: 0000-0003-4366-1805

© Jordan E. Easter 2018

## **Acknowledgement**

Honestly I can't believe the time has come! I thought the day I would compile my findings and prepare to close the chapters of my thesis might stay forever frozen in a dream. What an exciting time! Though I am the one putting pen to paper, or more literally fingers to keys, this work is hardly the result of an isolated journey. I have many dear people to thank and reviewing their love and support is nearly overwhelming, in the best of ways.

To Dr. Stani Bohac, thank you for your patience and dedication to the details, you were a solid guide and great compliment to my personality. To John Hoard, thank you for your constant contributions to my research and life. Your wealth of knowledge is impressive, but your willingness to use it for the good of those who are young is even more so. To Dr. Andre Boehman, your positivity surrounding every issue, excitement at every interesting challenge and brilliance are inspiring. I'm so thankful you were able to support as my faculty chair and your comments regarding my thesis work were extremely important.

To the additional committee members, Dr. Herek Clack and Dr. Angela Violi, thank you for your time and guidance during this process.

To Jim Daley, your support of my thesis has really been important to me. You were vital to my success, ensuring there were no pressures from HR or upper management, open to talking with me regarding thesis ideas and of all things, taking a spot on my committee! In addition, your constant support and push to be more confident will stay with me. To Jeff Wuttke, many of

the same things may be said for you. You have been so supportive during this time, granting me the time and resources I needed. I am very excited to work for you full time following the thesis, and I feel so thankful to have such a positive, kind, invested and capable manager.

To those who have helped directly build the experiment, I am deeply indebted. To Doug Viele, thank you for assisting with the concept generation for builds and for your quality craftsmanship. Your dedication to the task at hand and intelligence are directly shown in this work, and I am certain this project would have taken much longer without you. To Bill Kirkpatrick, your willingness to help me on the spot with issues in the test cell and your knowledge on various mechanical systems were invaluable. I will miss hearing your crazy stories.

To those at the Michigan Center for Materials Characterization, you are central to the achievement in this work. To Dr. Kai Sun, thank you for your patience and expert work with the electron microscopes. To Dr. Haiping Sun, thank you for your time in teaching me how to operate the instruments and assisting with various issues, your kindness is much appreciated. To Bobby Kerns, thank you talking me through data analysis and supporting me when I needed help with a technique.

To those students within the Autolab who have worked with me at various times, thank you. Your help was crucial in my ability to run and devise experiments. To Chenxi Sun, thank you for sharing your expertise and for teaching me how to operate various equipment. I often missed you in my final year. To Shuqi Cheng, thank you for sharing the long hours running the engine and building the test cell. You made the time fun. To Angela Fiano and Elizabeth Bernhardt, thank you for sitting at the test cell with me and for your contributions in completing

the sponsored portion of the work. I greatly enjoyed working with you. To those at the Autolab for which friendship was provided, I thank you as well. Justin Koczak and Ripu Singh, I hope we continue to stay in touch even after our graduations, and I would like to thank you for the great conversations and support.

To my parents, you have always allowed me to find my own path but knew when to push at just the right time, ever so lightly. Thank you for flying half way across the country to see me defend and for providing such a stable home in the years of my youth. To my dad in particular, thank you for bringing your daughter along to ride and work on dirt bikes. This clearly pushed me into mechanical engineering and engine research. It meant the world to me. To Michael Tung, I want to thank you for being such a support in my life. You are an amazing person, full to the brim with drive, playfulness, love and dreams. I am still in awe that one person can possess so much and with such effortless balance, nevertheless, you help me find the direction when needed and inspire me to stay dedicated to the most difficult of tasks. You have certainly influenced my life and this work.

I would also like to thank God for the ability, circumstances and health that allowed me to do this work. I have been given more than I deserve, and I hope to make the most of this. I know many are not so lucky.

This work has been supported by the Department of Mechanical Engineering and the College of Engineering at the University of Michigan. Support has also been given by the National Science Foundation and the Rackham Graduate School.

I hope my life can remain as rich in support and friendships as it was during the past 4.5 years.

## Table of Contents

Acknowledgement .....	ii
List of Figures .....	viii
List of Tables .....	x
List of Appendices .....	xi
Abstract .....	xii
Chapter 1. Introduction .....	1
1.1 Background.....	1
1.2 Hypothesis.....	3
1.3 Research Methods.....	3
Chapter 2. Literature Review .....	5
2.1 Gasoline Direct Injection Engines and Particulates.....	5
2.2 Gasoline Particulate Filters .....	7
2.3 PM Composition and Formation .....	9
2.4 Impact of Operating Condition on Soot Nanostructure .....	11
2.5 Impact of Operating Condition on Soot Formation Rates .....	12
2.6 Soot Reactivity.....	14
2.6.1 Nanoparticle Structure .....	14
2.6.2 Surface Functional Groups and Oxygen Content .....	15
2.6.3 Volatile Organic Fraction .....	16
2.6.4 Ash .....	16
2.6.5 Particle Surface Area .....	17

2.6.6 Variations in the Soot Oxidation Process .....	18
2.6.7 This Thesis.....	20
Chapter 3. Experimental Set-Up.....	21
3.1 Test Cell Set-Up .....	21
3.2 Engine Operating Conditions .....	24
3.3 Particle Size Distribution .....	26
3.4 Soot Concentration .....	26
3.5 Particulate Collection .....	27
3.6 PM Characterization Instruments/Methods.....	29
3.6.1 Thermogravimetric Analysis (TGA).....	29
3.6.2 Transmission Electron Microscope (TEM) .....	35
3.6.3 Raman Spectroscopy .....	35
3.6.4 X-Ray Photoelectron Spectroscopy (XPS).....	36
3.6.5 Scanning Transmission Electron Microscope with Energy Dispersive Spectroscopy (STEM – EDS).....	40
3.6.6 BET Specific Surface Area .....	43
3.6.7 Inductively Coupled Plasma – Mass Spectrometry .....	44
Chapter 4. Particulate Matter Reactivity.....	46
4.1 Isothermal Oxidation.....	46
4.2 Temperature Programmed Oxidation.....	49
4.3 Quantification of Reaction Rate Parameters .....	51
4.4 Summary .....	54
Chapter 5. Impact of Operating Conditions on Combustion and PM Properties.....	56
5.1 Combustion .....	56
5.2 Particulate Emissions .....	58
5.2.1 Particle Size Distribution.....	58
5.2.2 Soot Concentration.....	59
5.3 Nanostructure .....	61
5.3.1 TEM.....	61

5.3.2 Raman Spectroscopy .....	66
5.4 Surface Area .....	69
5.4.1 Primary Particle Size - TEM.....	69
5.4.2 BET .....	73
5.5 Volatile Organic Fraction.....	75
5.6 Chemical Composition .....	78
5.7 Ash.....	87
5.7.1 ICP-MS.....	88
5.7.2 XPS .....	89
5.7.3 Carbonaceous Soot Concentrations.....	90
5.7.4 STEM-EDS.....	91
5.8 Summary .....	98
Chapter 6. Partial Oxidation Results.....	99
6.1 Particle Characteristics during Oxidation.....	99
6.1.1 Nanostructure and Particle Interactions .....	99
6.1.2 Chemical Composition.....	105
6.2 Ash Content.....	107
6.2.1 XPS .....	108
6.2.2 STEM+EDS.....	108
6.3 Summary .....	114
Chapter 7. Ash Influence on the Oxidation Process .....	115
Chapter 8. Conclusions .....	122
Chapter 9. Future Work .....	127
Appendices.....	129
Appendix A .....	129
Appendix B .....	132
Bibliography .....	134



## List of Figures

Figure 1. Gasoline Direct Injection (Left) and Port Fuel Injection (Right) .....	5
Figure 2. Schematic of a Particulate Filter.....	8
Figure 3. Illustration of the Two Different Modes of Filtration for Engine-Out Particulates .....	8
Figure 4. Cartoon of Particulate Matter .....	11
Figure 5. Impact of Fuel Injection Timing on Fuel Impingement .....	13
Figure 6. Soot Oxidation from the Interior Outward .....	19
Figure 7. Images of the LNF Engine used for Soot Collection .....	22
Figure 8. Illustration of Teflon Filter Loading Set-Up .....	28
Figure 9. Sampling apparatus for TEM grids .....	29
Figure 10. Example of Comparison of Bright and Dark Field Images for Ash Detection .....	42
Figure 11. Repeatability and Reproducibility of ICP-MS Analysis on Engine Oil Sample by Element .....	45
Figure 12. Isothermal Oxidation Events in TGA for Soot Samples in Ultra-Zero Grade Air: (a) 500 °C, (b) 550 °C, (c) 600 °C .....	47
Figure 13. $t_{10-90}$ Times for Soots from the Various Engine Operating Conditions .....	49
Figure 14. TGA Oxidation of Soot Samples using a Temperature Ramp. ....	50
Figure 15. Comparison of Oxidation Parameters for a Fit to Arrhenius Type Equation using TGA Results from Iso-Thermal Oxidation at 500 °C .....	52
Figure 16. Curve Fits to Determine the Apparent Rate Constant .....	53
Figure 17. In-Cylinder Pressure Trace for All Four Operating Conditions .....	57
Figure 18. Particle Size Distribution for the Four Operating Conditions .....	58
Figure 19. Soot Concentration from the Four Engine Operating Conditions .....	60
Figure 20. TEM Imaging Results from the Baseline Operating Condition: (a), (b) .....	62
Figure 21. TEM Imaging Results from the Late Start of Injection Operating Condition: (c), (d) .....	63
Figure 22. TEM Imaging Results from the Early Start of Injection Operating Condition: (e), (f) .....	64
Figure 23. Peak Analysis Performed on Baseline Raman Spectra .....	67
Figure 24. $A_{D1}/A_G$ and $I_{D1}/I_G$ ratio for the Four Operating Conditions .....	68
Figure 25. TEM Images of Primary Particles at 60k-85k for (a) Baseline (b) Late Start of Injection (c) Early Start of Injection (d) Low Injection Pressure. ....	70
Figure 26. BET Surface Area.....	73
Figure 27. Comparison of Soot Reactivity to BET Surface Area.....	75
Figure 28. Average Volatile Organic Fraction for the Four Operating .....	76
Figure 29. Comparison of Reactivity against VOF for the Soots from the Four Engine Operating Conditions .....	78

Figure 30. Carbon and Oxygen Values for Four Operating Conditions based on XPS.....	79
Figure 31. Peak Deconvolution for the C1s Peak (Early SOI Sample) .....	80
Figure 32. Peak Deconvolution for the O1s Peak (Early SOI Sample) .....	80
Figure 33. Atomic Percentage of Various Bonding States for both Oxygen and Carbon .....	81
Figure 34. Comparison of Sp <sup>3</sup> Results from XPS and Raman.....	83
Figure 35. Comparison of Sp <sup>3</sup> /Sp <sup>2</sup> with the BET Surface Area (m <sup>2</sup> /g) .....	84
Figure 36. Comparison of Sp <sup>3</sup> /Sp <sup>2</sup> ratios to Sample Oxygen Percentage for the Four Operating Conditions .....	85
Figure 37. Comparison of Reactivity (T10-T90 time for 500C oxidation) to the Sp <sup>3</sup> /Sp <sup>2</sup> ratio...	86
Figure 38. Concentration of Various Elements from a Sample of the Engine Oil .....	88
Figure 39. Soot Oxidation Time, t10-90, Plotted against Engine-Out Soot Levels as Measured by the AVL Filter Smoke Meter .....	91
Figure 40. STEM+EDS Results Baseline: (a) Bright Field Image, (b) Dark Field Image, (c) EDS Spectra.....	93
Figure 41. STEM+EDS Elemental Mapping of Baseline Sample: (a) O, (b) Ca, (c) Cu, (d) Mg, (e) Zn, (f) Overlay .....	94
Figure 42. STEM+EDS Results Early SOI Condition: (a) Bright Field Image, (b) Dark Field Image, (c) EDS Spectra.....	96
Figure 43. TEM Images Taken of the Soot Oxidation Process: (a) Baseline 0% - 65k, (b)Early SOI 0% - 65k, (c) Baseline 40% - 65k, (d) Early SOI 40% - 80k, (e) Baseline 75% - 80k, (f) Early SOI 75% - 80k.....	100
Figure 44. Pellet of Early SOI 40% Oxidized Soot from TGA Crucible .....	101
Figure 45. TEM Images Taken at a Magnification at 300k of the Soot Oxidation Process: (a) Baseline 0% - 300k, (b) Early SOI 0% - 200k, (c) Baseline 40% - 160k, (d) Early SOI 40% - 160k, (e) Baseline 75% - 160k, (f) Early SOI 75% - 160k.....	104
Figure 46. Sp <sup>3</sup> /Sp <sup>2</sup> Ratio during Soot Oxidation for the Baseline and Early Start of Injection Condition.....	106
Figure 47. Surface Functional Groups present for the Baseline and Early SOI Condition during Oxidation.....	107
Figure 48. STEM+EDS Results Baseline Condition 75% Oxidized: (a) Bright Field Image, (b) Dark Field Image, (c) EDS Spectra .....	109
Figure 49. STEM+EDS Elemental Mapping of Baseline Sample: (a) O, (b) Cu, (c) Na, (d) Zn, (e) Ca, (f) Overlay .....	111
Figure 50. STEM+EDS Results Early SOI Condition 75% Oxidized: (a) Bright Field Image, (b) Dark Field Image, (c) EDS Spectra .....	113
Figure 51. Influence of Small Amounts of Ash on Soot Reactivity .....	116
Figure 52. Determination of Phases of Oxidation .....	117
Figure 53. Cartoon Illustrating the Soot-Ash Interaction during the Soot Oxidation Process ...	119
Figure 54. Influence of Baseline Ash Amounts on the Oxidation Process.....	120
Figure A- 1. Raman Spectroscopy Peak Deconvolution for Low Injection Pressure.....	130
Figure A- 2. Raman Spectroscopy Peak Deconvolution for Late Start of Injection.....	130
Figure A- 3. Raman Spectroscopy Peak Deconvolution for Early Start of Injection .....	131
Figure B- 1. XPS Peak Deconvolution for Baseline Condition: (a) C 1s (b) O 1s.....	133

## List of Tables

Table 1. Engine Specifications .....	22
Table 2. Stock Engine Parameters at 1600 RPM- 8 Bar BMEP .....	25
Table 3. Operating Parameters for the TGA Work.....	30
Table 4. Peak Assignment for C 1s Spectra.....	39
Table 5. Apparent Rate Constant Values from Three Portions of the Oxidation Profile .....	54

## List of Appendices

Figure A- 1. Raman Spectroscopy Peak Deconvolution for Low Injection Pressure.....	130
Figure A- 2. Raman Spectroscopy Peak Deconvolution for Late Start of Injection.....	130
Figure A- 3. Raman Spectroscopy Peak Deconvolution for Early Start of Injection .....	131
Figure B- 1. XPS Peak Deconvolutions from Baseline: (a) C 1s (b) O 1s .....	133

## **Abstract**

Upcoming regulations, such as Euro 6c, decrease limits on allowable tailpipe particulate number emissions. These regulations may place some current gasoline engine technologies above the legal limit, especially those vehicles using direct fuel injection. Therefore, gasoline particulate filters (GPF) may be necessary for future emissions compliance. The key functionality of the GPF is filtration efficiency and control of this function is dependent on the soot build-up within the filter. The more soot present, the higher the filtration efficiency. As soot will often oxidize during much of the engine operation due to high temperatures and available oxygen, an understanding of soot reactivity and the degree to which reactivity may vary is key for designing after-treatment architecture and explaining low filtration efficiency results in real world situations.

In this work, soot was evaluated from four conditions incorporating changes in the fuel injection pressure and timing, and the influence these parameter variations had on soot reactivity was evaluated through well-controlled isothermal and ramped oxidation events. It was determined that soot reactivity and the temperature by which oxidation would commence were quite different for the four samples. Following this, soot parameters known to influence reactivity were investigated. It was determined that nanostructure, volatile organic fraction and surface functional groups were similar between all four samples and though surface area was different, it did not correlate with reactivity. It was determined through estimations of the ash

content that soot reactivity was likely influenced by the ash to soot ratio of the particulate matter. Ash is a known catalyst, found to enhance soot oxidation rates. The presence of ash and the interaction of soot and ash were investigated using a scanning transmission electron microscope coupled with energy dispersive x-ray spectroscopy (STEM+EDS).

To carry further the investigation, soot samples from the most and least reactive condition underwent partial oxidation and the partially oxidized soots were analyzed to obtain information regarding the oxidation process. During oxidation, the soot particles appeared more amorphous and began to meld into each other, forming larger non-spherical particles.

It was determined that beyond a sufficient ash-soot ratio, a ratio likely below 1% and easily reached for a modern gasoline direct injection engine, the soot oxidation process is marked by three distinct phases relating to interactions of ash and soot particles. In the first phase, the oxidation rate is enhanced by the presence of close soot to ash contact. Soot in close contact with the ash will oxidize first, leaving a loose contact between the ash and soot. This loose contact causes the observed distinction in the second stage. In the second stage, despite increases in the ash to soot ratio due to the loss of soot, the oxidation rate decreases due to the loose ash to soot contact. As oxidation proceeds, soot particles begin to meld together, forcing the ash to be in close contact with any remaining soot. This renewed close soot to ash contact causes the observed distinction in the third stage. In the third stage, soot oxidation rates increase until the end as the close soot to ash contact is maintained and the ash to soot ratio increases with oxidation of the soot

## **Chapter 1. Introduction**

### **1.1 Background**

The use of direct injection systems for gasoline engines has been widely adopted by various automotive manufacturers for good reason. This technology is proven to enhance fuel efficiency due to charge cooling and more precise fuel control when compared to its port fuel injection counterpart. However, the reduced time for fuel and air to mix and the impingement of fuel on piston tops and cylinder bore walls will cause an increase in vehicle particulate emissions. When this increase in particulate emissions is coupled with an increasing regulatory stringency for allowable particle number emissions such as found with the Euro 6c regulations that limit particulate number values to  $6.0 \times 10^{11}$  #/km, gasoline particulate filters (GPF) enter the market place as a serious option for future emissions compliance.

An understanding of gasoline soot reactivity is essential for effective implementation and protection of the GPF. Prior to the development of an ash layer along the walls of the gasoline particulate filter from incombustible lubrication additives, catalyst precious metals and engine wear metals that accumulate as the filter ages, the state of soot build-up on the filter will be essential for understanding variations in particulate filtration efficiency. A new filter without a soot layer may have only 60% or so filtration efficiency, but as the soot layer builds, even to just

a small amount, filtration efficiency can be dramatically improved (Spiess, et al. 2013). This characteristic of low filtration efficiency when clean may push system numerical simulations to use the soot reactivity to generate models that dictate GPF placement and engine control changes. This information may also be useful in explaining anomalies in testing data as sometimes the soot may easily oxidize and filtration efficiency is low, while at other times soot may remain on the filter and filtration efficiency will be high.

Active regeneration, by which the engine controller intentionally manipulates engine parameters to achieve soot oxidation, possibly through changes in spark timing, valve timing and fuel control, presents another reason soot reactivity should be understood. GPFs are more porous and have smaller wall thicknesses as compared to their diesel counter-part, thus resulting in lower levels of allowable soot build-up before filter damage may occur (Johnson 2014). It is likely that under some conditions gasoline filters may fill with soot to this allowable limit. The understanding of what that allowable limit may be before filter damage will occur and what the control strategy for regeneration should be to ensure protection of the filter from thermal damage is highly dependent on an understanding of soot reactivity and why it may vary.

Given these concerns, gasoline soot reactivity has become a topic of exploration within recent years and a variety of researchers have advanced the understanding of soot reactivity. Researchers have identified the gasoline soot particles to be much lower in number relative to diesel with immature and amorphous nanostructures, likely forming in low temperature regions (Farron, et al. 2011), (Seong, Lee and Choi 2013). They have also identified that gasoline soot particles are more reactive than diesel soot particles, possibly due to their amorphous nature and high ash-soot ratio (Choi and Seong 2016). Works regarding the influence of fuel injection



parameters on soot reactivity and works to understand the oxidation process of the gasoline soot have yet to be performed. This work sets out to explore these topics.

## **1.2 Hypothesis**

Variations in soot reactivity for a gasoline direct injection engine may occur due to different operating parameters that dramatically affect the soot formation rate, such as fuel injection pressure and timing. Any corresponding differences in reactivity may be attributed to particulate matter (PM) properties such as nanostructure, surface area, surface functional groups, volatile organic fraction and ash content. The reactivity may be further explained by observing and understanding mechanisms within the oxidation process.

## **1.3 Research Methods**

This work sets out to answer these questions through the collection of soot produced from a modern 2.0 liter inline four-cylinder turbo-charged gasoline direct injection engine. Reactivity will be evaluated with isothermal and temperature ramped oxidation events utilizing a thermogravimetric analyzer (TGA).

As the variation in reactivity may be attributed to the various soot properties, these will be evaluated with a variety of methods. General soot characteristics such as the particulate number and carbonaceous soot content will be evaluated through a scanning mobility particle sizer (SMPS) and a smoke meter, respectively. Evaluation of nanostructure will be performed using Raman spectroscopy and image collection with a high-resolution transmission electron microscope (TEM). Evaluation of surface area will be explored through analysis of primary

particle size and BET surface area techniques. Surface functional groups (SFG) will be evaluated through x-ray photoelectron spectroscopy (XPS) core scans of energy levels representing carbon and oxygen bonding. Volatile organic fraction (VOF) content will be evaluated through high purity nitrogen and analysis using the TGA. Ash content will be investigated through XPS survey scans and scanning transmission electron microscopy coupled with energy dispersive spectroscopy (STEM+EDS).

Understanding of the mechanisms behind the variation in soot reactivity will be explored by analyzing the oxidation process. This will include partial oxidation events performed using the TGA and analysis of primary particle interaction and particle nanostructure evolution using TEM and XPS core scans. In addition, evaluation of the soot-ash interaction will be conducted on partially oxidized samples using STEM+EDS.

## Chapter 2. Literature Review

### 2.1 Gasoline Direct Injection Engines and Particulates

Direct injection systems conventionally introduce fuel either through a sidewall mounted injector with a piston top designed to guide the flow or through a centrally mounted location in the cylinder head. A visual comparison for the reader is given between the port fuel and direct injected systems in Figure 1 (Zhao, Lai and Harrington 1999).

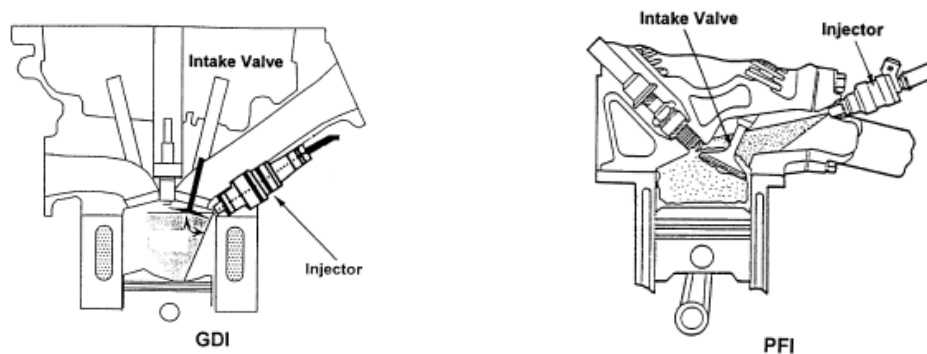


*Figure 1. Gasoline Direct Injection (Left) and Port Fuel Injection (Right)*

This method of direct injection of gasoline fuels (GDI) has fuel efficiency and performance benefits over the port fuel injection system (PFI). The fuel can be controlled to a higher metering accuracy as all fuel sent through the injector will enter the combustion chamber. In addition, charge cooling will occur during fuel vaporization in the chamber thus allowing for a higher compression ratio and more efficient engine design (Zhao, Lai and Harrington 1999).

Though the growth in market share for gasoline applications is recent, this technology has been around for some time, with a conception and implementation dating back to gasoline powered aircraft in the start of the 20<sup>th</sup> century. It was during this time that direct injection was employed to prevent engine stalling on aircraft (Hartmann 2007). The more recent gains in market volume regarding vehicle applications are likely attributed to the reduction in cost and elevation in efficiency for modern injection systems. These two factors eventually reached a point where the benefits regarding fuel control and economy outweighed the cost of adding a more complex injection system and fuel pump.

The adoption of this technology made sense to many automakers, and so the market share of the technology grew. Though this growth continues, integration and future compliance regarding emissions regulations has provided some interesting problems requiring further technology evolution. There is a significant increase in particulate emissions as the fuel fails to mix to the homogeneous state found with a PFI system and fuel impingement on cylinder walls or piston tops may occur (Myung and Park 2012). This lack of proper mixing often results in particulate matter (PM) emissions at an order of magnitude higher for a GDI system when compared to PFI (Zhang and McMahon 2012). This particulate emission constituent, PM, was previously of little concern for gasoline engine compliance. However, with the introduction of

future emissions regulations focused on reducing the cardiovascular and respiratory health risks posed by particulate matter (Schwarze, et al. 2006), this no longer holds true. These upcoming regulations, such as Euro 6c, require certification of vehicles with particulate number (PN) emissions below  $6 \times 10^{11}$  #/km. These upcoming regulations are below current engine out values of gasoline direct injection equipped vehicles, therefore some action will need to be taken for future compliance to be achieved (Zhang and McMahon 2012).

## **2.2 Gasoline Particulate Filters**

Though enhanced calibration or hardware changes may allow for compliance with future regulations (Su, et al. 2014), there is one solution emerging in literature that is likely to guarantee compliance. As regulations continue to lower particulate emissions limits even beyond the aforementioned Euro 6C, its integration with future gasoline direct injection equipped vehicles may become impossible to avoid. This solution is a gasoline particulate filter (GPF). Similar to the diesel particulate filter (DPF) that has been used with success in diesel applications since 2007, the GPF is a ceramic “wall flow” filter often made of cordierite or silicon carbide (Seo, Park and Lee 2012). To allow for a better understanding of this filter, an image is shown in Figure 2 (Wall-Flow Monoliths n.d.). A GPF has alternately plugged channels that force the exhaust to flow through its porous wall. As the particles flow through the filter, they collect along the pores. The GPF has been evaluated by research groups and has been shown to reduce particulate emissions to levels below the most stringent future particulate emissions standards (Chan, et al. 2012).

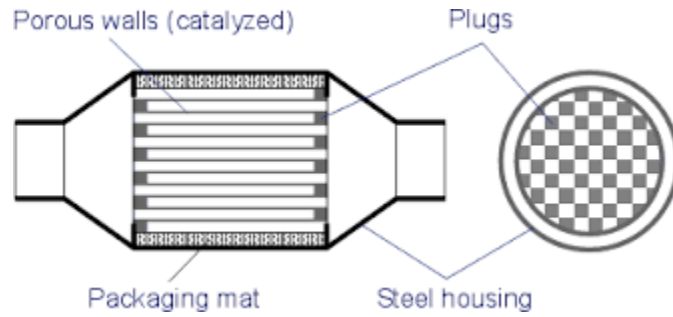


Figure 2. Schematic of a Particulate Filter

The GPF should not be added to vehicle exhaust architectures without some additional understanding of the physics behind its filtration performance and control by exhaust conditions if it is to be implemented correctly. One factor that must be considered is the development of the soot layer to aid in the filtration efficiency. Figure 3 (Majewski 2013) is given to help illustrate the particle-filter interactions for the two modes of filtration: depth filtration (pore filtration) and cake filtration (bed filtration).

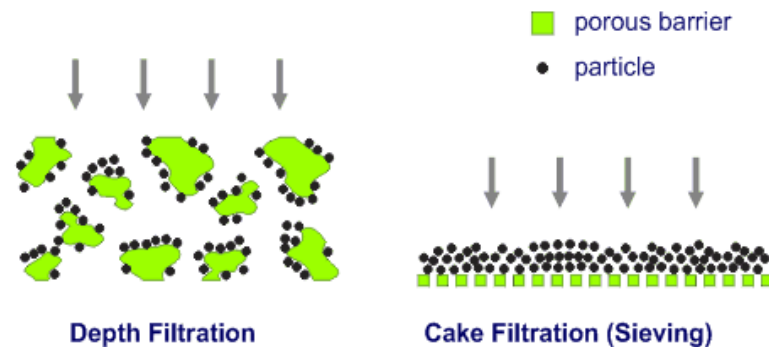


Figure 3. Illustration of the Two Different Modes of Filtration for Engine-Out Particulates

As the soot collects along the pores of the GPF during pore filtration, a soot layer forms. As this soot layer grows and bed filtration is achieved, so does the ability of the filter to capture a higher rate of soot particles, thus improving the GPF filtration efficiency. Historically diesel engines have low exhaust temperature and high levels of soot, therefore the DPF is loaded quickly and filtration efficiency is very high for much of the life of the vehicle. Given the lower soot level and higher exhaust temperature of the gasoline engine, the layer of soot on the filter may vary quite a bit (Nicolin, et al. 2015). As a result, soot dependent filtration efficiencies may fluctuate from 40% to near 100% as collected soot may be oxidized to CO and CO<sub>2</sub> before high filtration efficiencies may be maintained (Zhong, et al. 2012). However, for situations where the exhaust temperature remains low enough or oxygen is not present, the soot layer will build, thereby causing a rise in filtration and a rise in engine backpressure as the engine must work harder to overcome the flow restriction generated by the soot coated filter wall. To alleviate this high backpressure, often accompanied by a fuel economy penalty, a regeneration process is controlled through some means of the engine controller to elevate exhaust temperatures and oxygen values in the exhaust (Seo, Park and Lee 2012).

Both the filtration efficiency and the regeneration process are heavily influenced by the reactivity of the soot, a topic only emerging recently in the literature for gasoline applications and a topic explored in detail with this thesis work.

### **2.3 PM Composition and Formation**

Soot reactivity is a product of the formation process, fuel composition and relevant lubrication/engine wear metals present in the combustion chamber.

Soot particles originate with the formation of tiny nucleation particles derived from precursors found within incomplete combustion often resulting from fuel rich zones. In the absence of oxygen and at temperatures above 400 °C, the hydrocarbon compounds from fuel or lubrication oil are decomposed into radicals and smaller hydrocarbon molecules through pyrolysis (Bosckhorn 1994). These small particles grow through radical addition and under the correct conditions of radical pool and temperature, will form the large aromatic molecules (Haynes, Bartok and Sarofim 1991) found at the nucleus of soot particles.

The combination of these precursors with other hydrocarbon molecules and any available polyaromatic hydrocarbons (PAHs) from the fuel coagulate to form small soot particles. Further dehydrogenation and combination of these particles leads to a rapid development of large particles (Frenklach 2002). During and after development, these particles may accumulate lubrication and wear metals. Following particle growth, these individual particles begin to form branched particle agglomerates of a non-spherical shape. When soot particles leave the combustion chamber, hydrocarbon vapors may bond physically or chemically to the surface of the particle and thereby increase the particle size and mass (Plee and MacDonald 1980).

These pathways within the combustion chamber and exhaust of an internal combustion engine lead to development of complex particles often referred to as particulate matter (PM). The resulting PM is a complex mixture of volatile/soluble organics, sulfates, nitrates, carbonaceous soot and ash. A cartoon image of a PM agglomerated particle with labeled components is given in Figure 4 (Mohankumar and Senthikumar 2017).



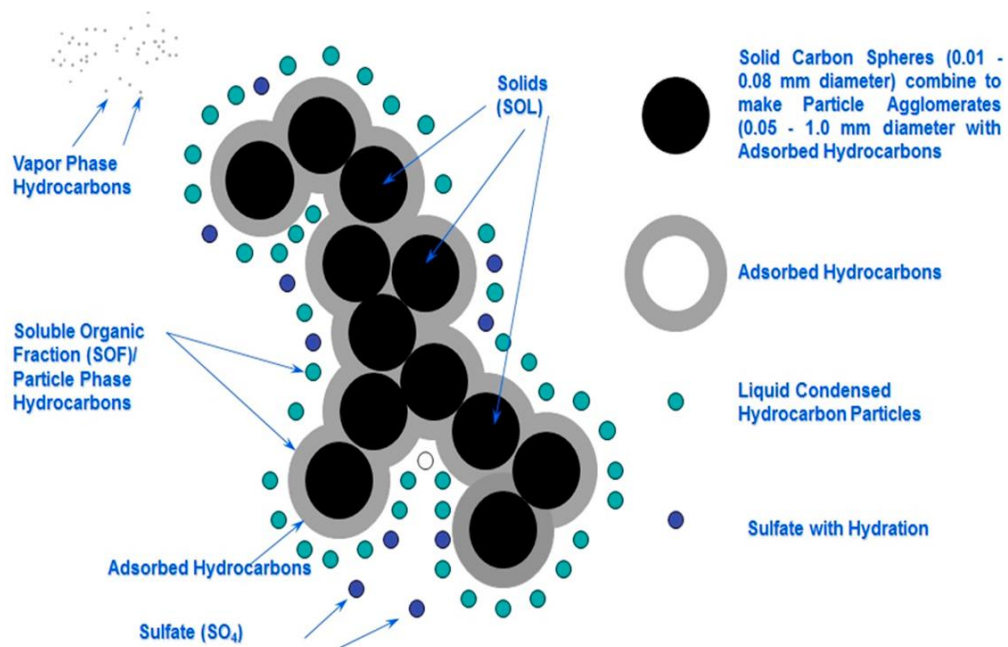


Figure 4. Cartoon of Particulate Matter

Furthermore, parameters affecting the combustion process such as the fuel structure, combustion temperatures, fuel injection timing and fuel injection pressure often play a role in the characteristics of the resulting complex PM.

## 2.4 Impact of Operating Condition on Soot Nanostructure

Soot nanostructure will be dependent upon the conditions by which the nucleation mode is formed and the processes by which the soot mass grows during soot formation (Vander Wal and Tomasek 2004). Temperature during formation has been observed to have a large effect. Low temperature conditions (<1250 °C) tend to produce highly amorphous soot regardless of fuel type as polycyclic aromatic hydrocarbon (PAH) formation dominates soot formation. However, during high temperatures (>1650 °C) both a highly graphitic and a highly curved

nanostructure may result. The resulting particle nanostructure at high temperatures is a product of the fuel chemistry and species formed during pyrolysis. PAH formation is again linked to a highly amorphous structure, while smaller hydrocarbon species such as  $C_2H_2$  are linked to more ordered graphene layers.

Gasoline soot particles tend to exhibit an amorphous nanostructure that is nearly unchanged by changes in injection pressure or timing as soot formation is likely to occur late in the combustion event and at relatively low temperatures (Bogarra, et al. 2017) where PAH formation would dominate soot growth. In addition to this, the gasoline soot may fail to undergo structural re-arrangement toward a more ordered structure that may happen during the life of a soot particle in diesel combustion as the nascent diesel particle may encounter temperatures high enough to promote a restructuring after formation (Zhu, et al. 2005).

## **2.5 Impact of Operating Condition on Soot Formation Rates**

As stated before, the level of engine-out soot for a gasoline engine is much lower than that found for diesel engines. Spark-ignited combustion, by which gasoline is burned, is dominated by a premixed flame instead of the diffusion flame as observed within diesel engines. Given the higher fuel/air mixing state for pre-mixed combustion within the spark-ignited engine, less soot is likely to form as less pyrolysis will take place. In addition, for pre-mixed flames, soot formation is often dictated by the quality of fuel/air mixing. Given this, injection timing and fuel pressure have been identified as two factors having a strong influence on engine out soot values (Su, et al. 2014).

Lower injection pressure will result in increased fuel droplet size given less shearing forces are exerted on the droplets sent by the fuel injector into the air charge in the chamber. These larger droplets will result in higher rates of fuel molecules undergoing pyrolysis, resulting in higher levels of soot formation (Su, et al. 2014).

Early and late fuel injection timings will also result in elevated PM levels. In Figure 5 taken from previous literature (Miyashita, et al. 2015), the influence on fuel impingement and mixing from changes in fuel injection timing parameters can be viewed for a wall guided injection system, as is used in this work.

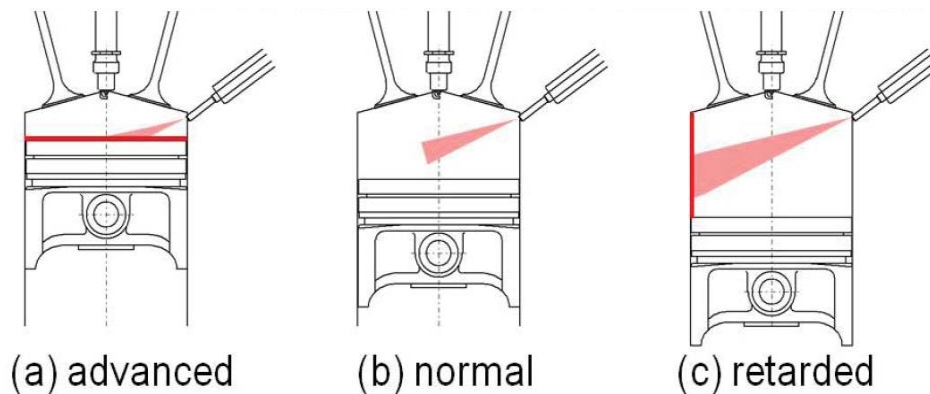


*Figure 5. Impact of Fuel Injection Timing on Fuel Impingement*

When the fuel injection timing is very early, advanced, fuel impingement will occur on the piston top causing a locally rich fuel puddle. Engine-out particulate values will continue to decrease as injection timing is retarded until some point at which proper fuel/air mixing becomes an issue again (Seong, Lee and Choi 2013). As timing is retarded, less time will be available for the fuel/air mixing to occur and the piston top may no longer be close enough to the injector to enhance mixing. Additionally, the spray may impinge on the cylinder walls forming a fuel film.

Therefore, engine-out soot values may continue to increase as the timing continues to be retarded.

## **2.6 Soot Reactivity**

Certain PM characteristics have been noted within literature to influence reactivity. These properties are as follows: nanoparticle structure, surface functional groups, volatile organic fraction, ash and particle surface area. Though there is still ongoing work to discuss the contribution to reactivity made by each property, what is currently known from past works is presented here.

### **2.6.1 Nanoparticle Structure**

The chosen definition for particle matter nanostructure was taken from work by Dr. Vander Wal (Vander Wal and Tomasek 2004). Furthermore, this chosen work defines nanostructure as “the degree of atomic order as manifested by graphitic layer plane segments and their physical relation to each other”. On one end of this term, amorphous soot, the layer plane segments are short and randomly oriented, by the other end of the term, graphitic soot, layer plane segments are several nanometers in lengths and stacked as you progress from the inner to the outer portion of the soot particle. The influence of nanoparticle structure on soot oxidation behaviors has been studied by various groups and the findings indicate the oxidation behavior may be strongly influenced by the soot morphology (Vander Wal and Tomasek 2003). The more amorphous the soot is structured, the higher chance for reactive carbon layer edge sites to be involved with H-atom abstraction followed by molecular (acetylene) addition (Frenklach and

Wang 1990) or for reaction with O<sub>2</sub> or OH as oxidation occurs (H.B. and C.F. 1965). Likewise, long graphene layers found in graphitic soot often result in a reduction of these potential reaction sites (Donnet 1982).

Curvature has also been showed to play a role regarding reactivity. Curvature may occur due to a 5-membered ring within the aromatic framework (Kroto, et al. 1985). This curvature can introduce bond strain as the orbitals overlap, and the electronic resonance stabilization is lessened. Therein the C-C bonds are weakened and individual atoms are more exposed and therefore less resistant to oxidation (Chiang, et al. 2001).

## **2.6.2 Surface Functional Groups and Oxygen Content**

Literature is unclear on the exact role surface functional groups may play on enhancing soot oxidation. Multiple pathways have been introduced through which the chemisorbed oxygen may affect the rate of the soot oxidation process. Some work suggests that bound oxygen in the form of carboxyl, lactone and carbonyl groups may enhance the soot reactivity as the energy required to oxidize some of the carbon to CO or CO<sub>2</sub> has been reduced (Keifer, et al. 1981). According to other findings, functional groups may enhance the oxidation process through electron exchange (Boehm 1994). Surface oxygen groups have been found in some work to enhance reactivity through structural change during soot oxidation. In work performed with biodiesel fuels it was found that soot derived from neat biodiesel soot, despite having an ordered structure prior to oxidation, was five times more reactive than soot derived from Fischer-Tropsch diesel due to the stronger presence of surface functional groups. These surface functional groups allowed for a unique oxidation pathway as they led to the removal of the outermost ordered shell

thus allowing access for the oxygen to the inner portion of the soot particles. This resulted in an internal restructuring of the soot to short and defective graphene layers that could be more easily oxidized (J. Song, et al. 2006).

### **2.6.3 Volatile Organic Fraction**

A high volatile organic fraction (VOF) has also been linked to enhanced reactivity (Kandas, et al. 2005). Early on in the oxidation process, porosity within the structure may develop due to a loss of this volatile matter. This improvement in porosity may allow oxygen to enter the inner portions of the soot, by which the formation of larger and turbostratic crystallites in the direction normal to the graphene layer may occur as layers within the soot rearrange. Through this crystallite growth there may be a stripping of the inner layers and a resulting faster oxidation rate (Walker 1990).

### **2.6.4 Ash**

Ash in the field of internal combustion engine research is a term referring to all materials in the PM that would not be oxidized during the regeneration of the particulate filter. This is a non-combustible contribution to the particles comprised of engine wear materials (Fe, Al or Si), lubrication additives (Ca, P, Na, Zn, B, Mo, etc) and any material from an upstream catalyst (Pt, Pd, Rh) (Lambert, et al. 2016). Metallic additives are present in most oil and have important functions such as: decreasing friction, preventing corrosion and regulating the oil acidity as combustion gases escape past the piston rings and enter the oil pan. The elements found within ash have been known to both enhance and inhibit soot oxidation (Neeft, Makkee and Moulijn

1996), (McKee, Spiro and Lamby 1984), (Neeft, Makkee and Moulijn 1996), (Miyamoto, Hou, et al. 1987). Additives containing calcium, zinc and sodium have been found to act as a catalyst for soot oxidation when in close contact, being directly involved with combustion. However, compounds such as phosphorus have been known to inhibit soot oxidation, possibly by coating the soot and forming a physical barrier to the oxygen. Calcium was identified as having the greatest impact on enhancing soot oxidation rates and reducing ignition temperatures (Choi and Seong 2016), (Miyamoto, Hou, et al. 1987). Even small amounts of calcium containing additives led to reductions of in-cylinder soot and increases in soot reactivity (Miyamoto, Hou, et al. 1987), (Choi and Seong 2015). As both oxidizing (Ca, Zn, Na) and inhibiting (P) compounds are present in standard oil formulations, it may be tricky to assume the overall impact of the ash on soot oxidation. However, given the high percentages of calcium in most oil additives and the highly catalytic nature of compounds containing the metallic element, works exploring the impact of lubrication oil on soot oxidation have found clear enhancements to reactivity when standard engine oil is doped into fuel and combusted for analysis of soot particles formed (Choi and Seong 2016), (Jung, Kittleson and Zachariah 2003).

Work with soot from gasoline engines have suggested that in comparison to findings for diesel soot, gasoline soot may have an elevated impact from the ash as the ash to soot ratio is much higher due to lower engine out soot levels (Choi and Seong 2015).

### **2.6.5 Particle Surface Area**

Particle specific surface is a product of primary particle size and primary particle overlap within the soot particle agglomerate (Lall, et al. 2008). The larger the particle size, the lower the

specific surface area. The more the particles overlap, the lower the specific surface area. The relationship with specific surface area and soot reactivity is not well understood and the impact on reactivity is not clear. Some researchers have found specific surface area or primary particle size to have no correlation with soot reactivity (Ye, et al. 2016), while others have found that there is a relationship with primary particle size and soot reactivity (Leidenberger, et al. 2012). Given that some works do suggest that specific surface area may affect soot reactivity and that it is known active surface area will influence carbon oxidation (Radovic, Walker and Jenkins 1983), and active surface area is a factor of specific surface area, the specific surface area is considered in this thesis.

## **2.6.6 Variations in the Soot Oxidation Process**

Though the soot oxidation process is often a factor of the aforementioned properties, an understanding of this process often provides additional clues as to why reactivity is affected. Rearrangement of the soot nanostructure during oxidation has an impact on soot oxidation rates and is not consistent for all soot samples. Differences in surface functional groups, volatile organic fraction and nanostructure prior to the oxidation process are key factors identified as being responsible for these observed variations in oxidation pathways. For some oxidation processes, the soot is burned from the outside in (T. Ishiguro, et al. 1991). This may be referred to as a shrinking core model. While others have observed oxidation occurring from the inside out (J. Song, et al. 2006). Figure 6 is given below to illustrate this inside out oxidation process for neat biodiesel soot (J. Song, et al. 2006).



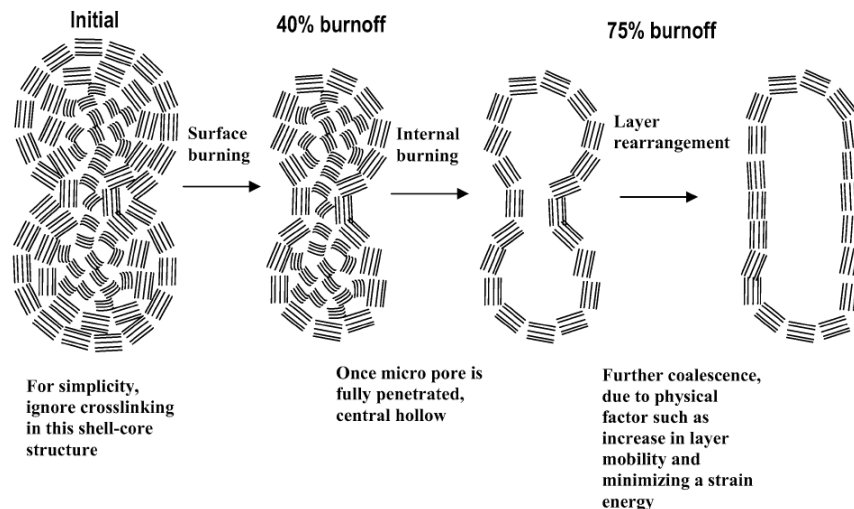


*Figure 6. Soot Oxidation from the Interior Outward*

Internal micropore development occurring for the oxidation of volatile organic materials embedded on the soot surface during the start of the oxidation process were shown to contribute to higher internal surface area available for oxygen and subsequent rearrangement of graphene layers to form turbostratic crystallites. In some works, it was shown that this turbostratic structure change resulted in “flaking” off of outer shells of the carbon particle as a result of strain energy in the layer plane (T. Ishiguro, et al. 1991). It was suggested that the soot continued to oxidize in this manner. While in other works, soot high in surface functional groups was found to oxidize from the inside out as the outermost layer “flaked” off and micropore development allowed access for oxygen to the inner more reactive carbon at the particle core (J. Song, et al. 2006). This internal burning was found to expedite the oxidation process with respect to the oxidation occurring from the outside in.

These findings are only complemented by previous works such as those by Heckmen et al. in studying carbon materials with differing synthesis conditions (H.B. and C.F. 1965). In this

work, graphitized thermal carbon black particles exhibited an oxidation process occurring from the outside in whereas as thermal carbon black that had been oxidized at 450 °C in 50% O<sub>2</sub> oxidized through internal burning.

The oxidation process for soot produced from gasoline direct injected engine has not been evaluated to date. This is a contribution of this thesis work as an understanding of this process seems essential to understanding differences in oxidation rates.

### **2.6.7 This Thesis**

Though there are existing works that have determined the reactivity and relating properties for soot from spark ignited gasoline engines, there is much left to be uncovered. This work sets out to explore the impact of changes to fuel injection pressure and fuel injection timing on soot reactivity and to explore the soot oxidation process and mechanisms responsible for observed variations in oxidation rates.

## **Chapter 3. Experimental Set-Up**

The experimental set-up was devised to enable characterization of particulates. Particulate mass and number were analyzed through measurements taken directly at the engine test cell. In addition, particulate reactivity and characteristics that may relate to reactivity such as nanoparticle structure, chemical composition, ash content and physical surface area were reviewed using sample collection methods and post processing with instruments located in laboratory type settings.

### **3.1 Test Cell Set-Up**

For this work a 2.0 MY 2010 GDI GM Ecotec LNF inline four cylinder turbocharged engine was used. A listing of the engine specifications are given in Table 1.

Bore	86 mm
Stroke	86 mm
CR	9.2
Fuel Injection	side mounted wall guided
Turbocharger	K04
Valvetrain	dual VVT with 50°CA phasing

*Table 1. Engine Specifications*

Images of the LNF engine used are given in Figure 7. A custom exhaust was added to allow for sampling sites for particulate emissions and soot collections.



*Figure 7. Images of the LNF Engine used for Soot Collection*

The fuel injection system used for this engine includes a side mounted wall guided system and Bosch HDEV5 injectors. The injector pressure for fuel introduction has the ability to reach 15.5 MPa. The oil used was Mobil 1 High Mileage Full Synthetic 5W-30. The same oil was maintained for the duration of the project.

The fuel used for this study was a “Spring/Fall” premium unleaded E10 pump gasoline. The same blend was used for the entire study. Details were obtained through an analysis done by Paragon Laboratories in Livonia, Michigan.

**Type: Premium Unleaded E10 Pump Gas**

LHV: 41.872 MJ/kg

Density: 0.7303 g/mL

HC type (FIA): 76.5% saturates, 1.7% olefins, 12.1% aromatics (% v/v)

Elemental analysis: 81.69% carbon, 14.52% hydrogen, 3.79% oxygen (% m/m) → CH<sub>2.12</sub>O<sub>0.0348</sub>

Oxygenates by GC: 9.67% ethanol (% v/v)

Distillation: 10% at 57.9°C, 50% at 104.4°C, 90% at 164.0°C

In-cylinder pressure data was collected using a ground isolated piezoelectric Kistler PiezoStar pressure sensor, of the type 6125C11, mounted in cylinder #1, cylinder closest to the bell housing. The charge amplifier used is also from Kistler and is of the type 5010. Combustion analysis was performed with the use of a high-speed combustion analysis system (CAS) by Phoenix. Pressure data was recorded with this system using a resolution of 0.1 crank angle degrees.

### 3.2 Engine Operating Conditions

For this work, the engine was held at 1600 RPM and 8 Bar Brake Mean Effective Pressure (BMEP). This specific speed and load was chosen as it represents a moderately high load and a moderately low speed. This combination allows for the desired balance point between the need of high particulates generated (from high loads and low speeds) with the need for low exhaust temperatures (as GPF loading was part of an independent set of this work using the determined variations in soot reactivity). To maintain similar levels of oil consumption, and as oil consumption is speed/load dependent, the speed and load values were not changed but the fuel injection pressure and injection timings were. The changes in injection timing included moving the stock set point of  $287^\circ$  before top dead center of the gas exchange event to either the early injection timing condition of  $325^\circ$  before top dead center of the gas exchange event or the late injection timing event of  $150^\circ$  before top dead center of the gas exchange event. The low injection pressure condition was a change in operation to a fuel pressure of 2 MPa over the stock set-point of 6 MPa. In this work, spark timing was maintained rather than CA50 so that the mixing dynamics of the fuel and air due to differing operation would dominate. Engine parameters and relevant values are given in Table 2 for the stock condition.

<b>Condition</b>	<b>Value</b>
Dyno Speed rpm	1600
Dyno Torque Nm	127
Coolant Temperature °C	85
Fuel Flow kg/hr	5.4
Intake Manifold Temperature °C	37.4
Intake Valve Opening CA aTDC	-34.6
Exhaust Valve Closing CA aTDC	26.1
Fuel Pressure Mpa	4.8
BSFC g/kWh	251.7
Start of Injection CA bTDC	287.2

*Table 2. Stock Engine Parameters at 1600 RPM- 8 Bar BMEP*

Fuel injection pressure and timing were chosen as these parameters have been proven in previous work to have the greatest impact on engine-out soot values for a GDI engine with a given fuel (Su, et al. 2014).

### **3.3 Particle Size Distribution**

The engine-out particle size distribution was determined through a scanning mobility particle sizer (SMPS) by TSI. This analyzer works by passing particles through a neutralizer to achieve charge equilibrium, followed by separating the particles using their electrical mobility and counting the separated particles with a condensation particle counter. The instrument used for this work contained a plutonium neutralizing source, 3080 model classifier, 3081 long DMA and 3776 model counter. The sheath flow rate was set at 15 SLPM and the sample flow rate was set at 1.5 SLPM. The particle size range evaluated was from 8nm to 300nm. Error bars were determined by the standard deviation of at least 3 samples taken at the same operating condition on the same day.

### **3.4 Soot Concentration**

An AVL Smoke Meter was used for measuring engine-out soot values. The soot concentration is also referred to as the black carbon or carbonaceous soot concentration. During our operation of the variable sampling smoke meter, a sample volume of 3000 mL was selected and the recorded value is an average of three independent samples. The AVL Smoke Meter was connected through a heated sample line to the exhaust. An 8 mm sample probe attached to the instrument was placed into the centerline of the exhaust pipe for exhaust collection. The AVL Smoke Meter pulls a volume of exhaust gas over white filter paper. This exhaust will blacken the paper and the amount of blackening is measured by a reflectometer. A lamp will illuminate the blackened paper, and the remitted light is captured by a photodiode in the reflectometer head. The output voltage of the photodiode is a function of remitted light, and the amount of light remitted is a function of how black the paper has become, with the darker the paper, the lower



the voltage output. The Christian correlation (Christian, et al. 1993) was used to convert the smoke number value to soot concentration as previous works suggested this correlation would work well at low engine-out soot levels (Northrop, et al. 2011). The instrument has a proposed detection limit around  $0.02 \text{ mg/m}^3$ , much lower than the estimated soot values for even the lowest soot producing condition explored in this work. Error bars are determined by the standard deviation in at least three samples taken at the same operating condition on the same day.

### **3.5 Particulate Collection**

Preparation of partially oxidized samples was assisted by Dr. Kai Sun at the Materials Characterization Center. This preparation included grinding of soot particles and distribution onto a grid through swiping of the grid over a light dusting of particles on a clean glass slide. Grinding was needed as aggregate particles tend to clump together during bulk collection, making imaging difficult without aggregate particle separation.

For collection of bulk particulate matter samples for analysis with the thermogravimetric analyzer (TGA) and X-ray photoelectron spectroscopy (XPS), a filter holder was installed on the exhaust system as shown in Figure 8. An Emerson  $\frac{1}{2}$  hp vacuum air pump was used to pull exhaust over a Pallflex Emfab<sup>TM</sup> Teflon filter that was 90mm in diameter. There was a one-way valve leading to the filter from the exhaust so that filter loading would only occur when steady state operation was achieved. After a desired period of filter loading, the valve was turned again to block exhaust flow and a fan was turned on to cool off the filter holder so that filter transfer could occur. Soot was then scraped from the Teflon filters into a glass vial with a sealing lid until the bulk soot samples were needed for analysis.

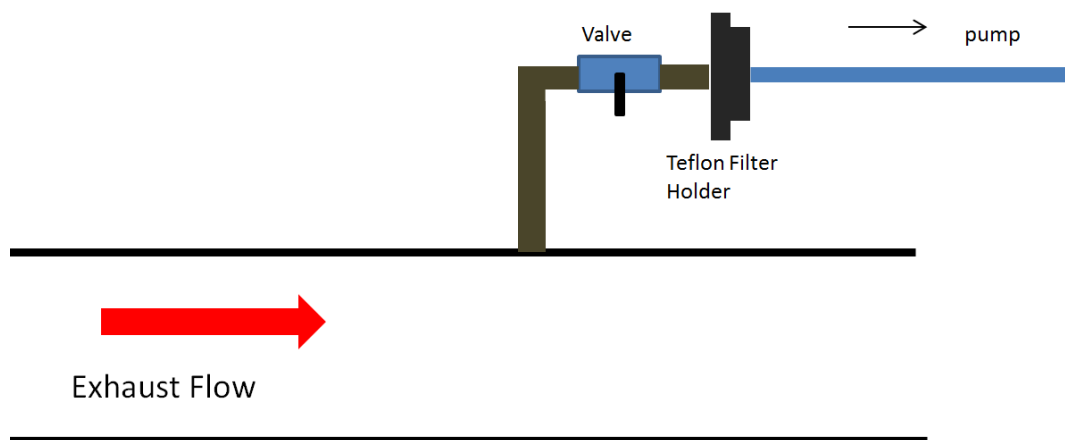


*Figure 8. Illustration of Teflon Filter Loading Set-Up*

For collection of particulate matter for imaging with a transmission electron microscope (TEM) and scanning transmission electron microscope coupled with energy dispersive spectroscopy (STEM+EDS), a 200 mesh lacy copper grid from Electron Microscopy Sciences was loaded using thermophoresis and a sampling apparatus designed by previous members of the group as shown in Figure 9. This apparatus can be placed in the exhaust through a quick connect fitting and will push the TEM sampling portion into the centerline of the exhaust for roughly 12 seconds. The sampling location was chosen to be near the outlet of the turbo in the exhaust to have the greatest temperature difference between the TEM grid and the exhaust soot particles, thereby enhancing the temperature driven mass diffusion effect (thermophoresis) driving the particulate collection on the grid. Given the low engine-out soot levels for gasoline engines relative to diesel, where most of these collection methods were developed, it is important to enhance the rates of collection so enough particles are collected for analysis.

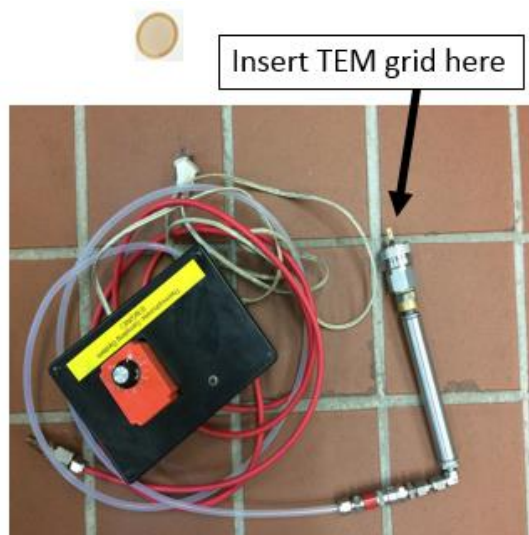


*Figure 9. Sampling apparatus for TEM grids*

### **3.6 PM Characterization Instruments/Methods**

A variety of instruments and methods were used to characterize the particulate matter from the four different operating conditions. These instruments and methods are discussed in the following paragraphs with respect to each instrument.

#### **3.6.1 Thermogravimetric Analysis (TGA)**

Soot reactivity was evaluated using a thermogravimetric analyzer (TGA) made by TA instruments. The model used in this work is a SDT Q600. At the start of each session, the instrument was zeroed using the empty crucible. Approximately 2.5-3.5 mg of soot powder collected from the engine was placed in a ceramic crucible and loaded into the TGA. A thermal treatment under Nitrogen at 500 °C was completed to drive off the volatile organic fraction, and the soot reactivity was explored through the introduction of ultra-zero grade air at various

temperatures. The loss in mass during the oxidation process was recorded, and for proper comparison of samples, the mass loss was normalized by the mass of the sample at the start of the oxidation process. TGA operating parameters are given in

Table 3.

Condition	TGA Procedure	Gas
De-volatilization	Ramp from ambient to 500 °C at a ramp rate of 10 °C/min. Hold at 500 °C for 30 min	Nitrogen
Isothermal - 500 °C	After De-volatilization, introduce Ultra Zero Grade Air and hold for 300 minutes	Air
Isothermal - 550 °C	After De-volatilization, ramp under Ultra High Purity Nitrogen to 550 °C at 10C/min. Hold at 550 °C for 10 minutes. Introduce Ultra Zero Grade Air and hold for an additional 100 minutes	Nitrogen / Air
Isothermal - 600 °C	After De-volatilization, ramp under Ultra High Purity Nitrogen to 600 °C at 10C/min. Hold at 550 °C for 10 minutes. Introduce Ultra Zero Grade Air and hold for an additional 30 minutes	Nitrogen / Air
Thermal Ramp	After De-volatilization, ramp to 350 °C under Ultra High Purity Nitrogen at 30 °C/min. Hold at 350 °C for 15 minutes. Introduce Ultra Zero Grade Air. Ramp temperature from 350 °C to 750 °C at 1 °C/min	Nitrogen / Air

*Table 3. Operating Parameters for the TGA Work*

Data was interpreted through differing techniques. The most straightforward technique was to determine  $t_{10-90}$ , or the time required during oxidation to take the normalized mass from

90% to 10%. This is the most direct value for comparing reactivity and soot property trends. This value,  $t_{10-90}$ , was collected from the data curves of normalized soot mass versus time for all isothermal cases. The normalized soot mass is given in Equation 1 and the  $t_{10-90}$  time is given in Equation 2. For these equations,  $m_n$  is the normalized soot mass and  $m_c$  is the mass in the crucible. The subscript  $i$  represents the instantaneous mass,  $f$  represents the final mass and  $s$  represents the mass in the crucible at the start of the oxidation experiment. For the time ( $t$ ) variable,  $m_n$  designates that the time is in reference to the normalized mass value specified.

Equation 1

$$m_n = \frac{m_{c,i} - m_{c,f}}{m_{c,s} - m_{c,f}}$$

Equation 2

$$t_{10-90} = t_{m_n=0.1} - t_{m_n=0.9}$$

An Arrhenius-type equation is often pursued for fitting kinetic parameters of soot oxidation with oxygen as it is often found to produce a good fit with experimental data. Equation 3 presented here was taken from the following work (Stanmore, Brilhac and Gilot 2001), (Choi and Seong 2015). In the following equations,  $r$  is the rate of reaction ( $s^{-1}$ ),  $A$  is a pre-exponential factor,  $E_a$  is the activation energy ( $\text{kJ mole}^{-1}$ ),  $R$  is the universal gas constant ( $\text{kJ mol}^{-1} \text{K}^{-1}$ ),  $\alpha$  is the degree of conversion and  $n$  is the reaction order.

Equation 3

$$r = A e^{\frac{-E_a}{RT}} (1 - \alpha)^n$$

Equation 4

$$\alpha = 1 - m_n$$

A logarithm of Equation 3 was performed to allow for TGA data curve fitting to result in values for  $E_a$ ,  $A$  and  $n$ . The result is shown in Equation 5.

Equation 5

$$\ln \frac{d\alpha}{dt} - n \ln(1 - \alpha) = \frac{-E_a}{RT} + \ln(A)$$

Correlations between  $\ln(d\alpha/dt)$  are compared to  $\ln(1-\alpha)$  to determine the needed kinetic parameters and fit of the soot samples to an Arrhenius type equation. Unfortunately, most of the soot samples exhibited a non-linear change in oxidation rate and therefore a linear regression was not achieved without high errors. Given this, an additional and more direct approach was taken to compare soot oxidation rates.

The use of a more simplified equation, using an apparent rate constant, by which the rate in change of soot mass is determined by the normalized soot mass, partial pressure of the oxidant present and an empirically determined rate constant has been used by a variety of works to explore soot reactivity (Sun 2017), (Radovic, Walker and Jenkins 1983). Equation 6 is taken from these works. The apparent rate constant,  $k_s$  in  $\text{min}^{-1} \text{Pa}^{-1}$ , is determined by data plotting from isothermal oxidation events. The other variables are defined as follows: the normalized soot mass,  $m_n$ , and the partial pressure of the oxygen within the TGA during oxidation,  $P_{o_2}$  in Pa.

Equation 6

$$\frac{dm_n}{dt} = -m_n k_s P_{O_2}$$

As  $P_{O_2}$  and  $k_s$  are constants, the equation can be rearranged and a logarithm taken in such a way that the following equation, Equation 7, results. The following values are used:  $m_n$  is the normalized soot mass,  $m_{n,0}$  is the initial normalized mass value,  $k_s$  is the rate constant,  $P_{O_2}$  is the partial pressure of the oxygen within the TGA during oxidation in Pa,  $t$  is time in minutes and  $t_0$  is the initial time. The initial time,  $t_0$ , is 0 and the initial normalized mass,  $m_{n,0}$ , is 1 as values are taken at the start of oxidation.

Equation 7

$$\ln\left(\frac{m_n}{m_{n,0}}\right) = -k_s P_{O_2} (t - t_0)$$

A plot of  $\ln(m_n)$  vs  $t$  was viewed to obtain,  $-k_s P_{O_2}$ , through a linear curve fit of the results. Though the rate constant and  $R^2$  values for the overall oxidation process are given in the results section, this data was again non-linear. Given this, the oxidation was broken into three sections and curve fits were again applied. These sections were mostly linear and had  $R^2$  values mostly above 0.99 with some curves still having values as low as 0.98. The high  $R^2$  value provided confidence that the linear fit could be applied to the three sections of the data and no further breakdown of the plots was needed. Therefore, a discussion of rate constants will be

performed based on the following intervals:  $m_n$  (0.9  $\rightarrow$  0.65),  $m_n$  (0.65  $\rightarrow$  0.35) and  $m_n$  (0.35  $\rightarrow$  0.1). Essentially these intervals are the initial, middle and final thirds of the oxidation process.

A test was performed to see the effect of the de-volatilization process on the soot reactivity. The de-volatilization process was held for both 60 minutes and 5 hours, rather than the standard 30 minutes. The reactivity was not affected by the duration of de-volatilization and 30 minutes was found to be sufficient to drive off all volatiles.

The SDT Q600 TGA was used to evaluate the volatile organic fraction (VOF). This value was collected during the de-volatilization process. The mass of the particulate matter sample was taken once the temperature reached 45 °C during the ramp to 500 °C and again after 30 minutes of exposure to nitrogen at 500 °C, the end of the de-volatilization step. The difference of the two weights divided by the initial weight is taken as the VOF fraction.

Engine-out soot samples will be compared to Printex-U. Printex-U is a carbon black pigment used within various industries for solvent and water borne coatings. It is commonly used across various entities pursuing research with engine-out soot as a way of comparing results across labs as this substance is very similar to engine-out soot but can be produced with consistent properties and purchased easily.

Soot reactivity within this work will often be discussed using the  $t_{10-90}$  time. Error analysis was applied to this value through repeated isothermal oxidation events with the TGA using select conditions. This data led to an average difference in  $t_{10-90}$  time between samples of 4%, and this value is applied as error bars for all relevant graphs.



### **3.6.2 Transmission Electron Microscope (TEM)**

Imaging with a JEOL 3011 ultra-high resolution capable transmission electron microscope with a lanthanum hexaboride thermoelectric emission gun was used for qualitative evaluation of the nanostructure of the particles from three of the different operation conditions. The JEOL 3011 has an objective focal length of 2.5mm, accelerating voltage of 300kV, point-to-point resolution of 0.17 nm and lattice resolution of 0.14 nm. A single tilt holder was used for all analysis. Images were acquired with a slow scan CCD camera. Magnification occurred at 60k to 85k for primary particle and aggregate evaluations and at either 200k, 250k or 300k for evaluation of particle nanostructure.

### **3.6.3 Raman Spectroscopy**

Raman Spectroscopy is a spectroscopic technique capable of observing vibrational, rotational and other low frequency modes in a system through the inelastic scattering of monochromatic light. The use of Raman for analyzing the nanostructure of carbon powders has been well documented (J. Song, et al. 2006), (Sadezky, et al. 2005), (Cuesta, et al. 1994), (Schwan, et al. 1996) . Raman spectroscopy should detect changes to edge sites present in the graphene layers and previous works have validated this hypothesis.

In this work, a Renishaw in Via Microscope was used with a high sensitivity low noise RenCam CCD detector to perform a first order Raman spectra. The laser was set at 10% intensity after burning of the sample occurred at 100% intensity. No burning was observed at 10% intensity. An argon laser producing light at a wavelength of 532 nm was chosen. Spectra collection for all samples was obtained through a static scan for Raman shift from 1086  $\text{cm}^{-1}$  to

1888  $\text{cm}^{-1}$ , centered at 1500  $\text{cm}^{-1}$ . Exposure was set at 5 seconds for a scan and 25 scans were taken for each measurement. Five measurements were taken for each sample so that error bars could be applied to the data using the standard deviation from the separate measurements. Spectral resolution capability for the instrument used was better than 1  $\text{cm}^{-1}$ . The analysis depth of the scattered monochromatic light is approximately a few microns.

For interpretation of Raman spectra, curve fits are typically applied to quantify specific peaks. In this work, one Gaussian and three Lorentzian peaks were identified. These peaks are described in order of lowest to highest Raman shift: the D4 peak (Lorentzian) at 1200  $\text{cm}^{-1}$  representing amorphous carbon or organic molecules, the D1 peak (Lorentzian) at 1350  $\text{cm}^{-1}$  representing disordered graphitic lattice, the D3 peak (Gaussian) at 1500  $\text{cm}^{-1}$  representing stretched carbon to carbon bonding and the G peak (Lorentzian) at 1590  $\text{cm}^{-1}$  representing a graphitic like structure. Traditionally the order of the soot nanostructure is defined by either the ratio of the areas or peak intensity for the D1 and G bands. With the higher the D1/G value, the more disordered the nanostructure. Curve fitting was performed with Origin Pro 2016 using the Peak Analyzer toolset.

### **3.6.4 X-Ray Photoelectron Spectroscopy (XPS)**

XPS is a surface sensitive quantitative spectroscopic technique that can be useful in analyzing elemental composition and the chemical state of those elements present in a bulk sample. XPS works through the inelastic scattering of photoelectrons. Atoms on the sample surface are bombarded with photons from the X-ray source, and upon absorption of the energy from the X-ray by a core-level electron, the sample atoms will emit a photon with a kinetic

energy dependent on the incident X-ray and binding energy of the atomic orbital from which the core electron had been residing. The energy and intensity (counts) of the emitted photoelectrons are used to determine the concentrations of elements or binding states present in the portion of the sample affected.

In this work, an Axis Ultra XPS from Kratos was used with a monochromatic Al source. Samples were placed on indium foil, that was then placed onto a double sided conductive carbon tape and then onto a copper bar. The energy resolution is around .5 eV for this system. For analysis of elemental composition, a survey scan was performed for each sample using a pass energy of 160 eV and a binding energy range from 0 eV to 1200 eV with 2 sweeps. Peak intensities and relative areas under those peaks were evaluated using CASA XPS software.

Sampling depth is defined as the depth by which 95% of all photoelectrons have been scattered by the time they reach the surface of the sample. Sampling depth is known to be between 3nm and 10nm with reported values for graphite finding a sampling depth of 8.7 nm (Tanuma, et al. 2005). Though X-rays may penetrate at greater depths into the sample, beyond the determined sampling depth, there is a low chance the ejected electron will leave the surface without undergoing some energy loss event and will therefore just contribute to the background noise. This depth is quite small and relegates this technique to analyzing the surface of the material of interest, in fact much of the work done with this technique is for thin films. Nevertheless, information should be relevant from the analysis of even the top layer of the soot particles. Measurement accuracy is often assigned as 10% for atomic concentrations (XPS 2013), and the detection limit is often assigned at 1%. Given the lack of repeated data sets for each condition, the error bars were set at 10%.

For analysis of chemical states regarding the C 1s and O 1s peaks, a binding energy range from 280 eV to 300 eV was chosen for the C 1s peak and a binding energy range from 528 eV to 540 eV was chosen for the O 1s peak. Spectra for both peaks were obtained using a pass energy of 20 eV. During data collection for the two peaks, 10 scans were used to resolve the O 1s peak and 3 scans were used to resolve the C 1s peak due to the higher intensity of the C 1s peak.

Curve fitting for various peaks within the C 1s and O 1s spectra was methodically performed. All peaks used were fitted with a 30% Gaussian and 70% Lorentzian peak. Curve fitting for the following bondings: C-C, C-O, C=O and O-C=O were used for this work as combustion derived carbonaceous matter is typically composed of aliphatic based C-C bonding, aromatic C-C bonding and various oxygen functional groups most dominantly through carboxylics, carbonyls, alcohols, ethers and phenolic species (Vander Wal, Bryg and Hays 2011), (Lee, et al. 2009).

Table 4 presents the peak assignment for the C 1s peaks. The C-C peak was easy to differentiate from the core scan as the value was much higher than the C and O bonding peaks. The differentiation between  $Sp^2$ - $Sp^3$  hybridization was approached using the relative values given in work by Gaddam et al. as it is the only published work identified to have performed XPS analysis on gasoline soot attempting  $Sp^2$ - $Sp^3$  hybridization (Gaddam and Vander Wal 2013). The values proposed closely aligned with those cited in other works for carbonaceous combustion matter (Vander Wal, Bryg and Hays 2011), (Wild, Pfander and Schlogl 1997). The C-O surface functional group was also fit by finding what appeared to be the second peak aside from the C-C and confirming that the chosen value of 286.5 matched various literature sources (Gaddam and Vander Wal 2013), (Vander Wal, Bryg and Hays 2011), (Biniak, et al. 1997). The

remaining two peaks were determined by consulting the same literature as mentioned for the C-O peak as well as a few others (Yue, et al. 1999) (Zhou, et al. 2007) and shifting the peaks to fill in where the counts dropped to the background level. Values for the C=O and O-C=O were in good agreement with literature reported values. Table 4 reviews the chosen peak assignments for the carbon bonding.

<b>C 1s Spectra</b>	<b>Peak Assignment (eV)</b>
<b>C-C Sp<sup>2</sup> (Graphitic or Aromatic)</b>	<b>284.4</b>
<b>C-C Sp<sup>3</sup> (Aliphatic or Amorphous)</b>	<b>285.2</b>
<b>C-O (alcohol, ether)</b>	<b>286.5</b>
<b>C=O (Carbonyls)</b>	<b>288.5</b>
<b>O-C=O (ester, carboxyl, lactone )</b>	<b>291</b>

*Table 4. Peak Assignment for C 1s Spectra*

The O 1s spectra was resolved into two peak assignments. One at 531.5 eV for the C=O bonding and one at 533.3 eV for the C-O bonding. These peak assignments were a result of two peaks apparent at certain operating conditions of the engine and by consulting again a variety of previous works using XPS with carbonaceous material (Lakshminarayanan, Toghiani and Pittman 2004), (Plomp, et al. 2009), (Smith, et al. 2016). The peak assignments matched literature reported values well.

### **3.6.5 Scanning Transmission Electron Microscope with Energy Dispersive Spectroscopy (STEM – EDS)**

A scanning transmission electron microscope (STEM) focuses the electron beam used to probe a specimen as in conventional TEM to a fine spot and then scans the sample in a designated pattern. This set-up allows for analytical techniques such as energy dispersive spectroscopy (EDS) to be employed as very small portions of the sample are being viewed with high beam energies. The high energy electron beam will excite inner shell electron of atoms in the sample and these electron may eject from their inner shell. Following this electronic ejection, an outer electron will fill the resulting hole, leaving its higher energy outer shell for the lower energy inner shell. During this relocation, energy is released in the form of an x-ray. The energy of this emitted x-ray is unique to the atom that was affected and can be detected with an EDS system.

In this work, soot samples were analyzed to determine the presence of lubrication and engine wear metals with a JEOL 2100 Probe-Corrected Analytical Microscope using a zirconated tungsten thermal field emission tip. The accelerating voltage was set to 200kV, the collection angle was set to 40 mrad and the beam convergence angle was set to 20 mrad. The image resolution is 0.19 nm point to point. The EDS system is an EDAX r-TEM Detector with EDAX acquisition software. This EDS system uses a Horizontal Ultra-thin Window Si-Li X-Ray Detector with an active area of 30 mm<sup>2</sup> and is capable of detecting elements with an atomic number greater than 5. Images were further processed using Gatan Microscopy Suite Software.

X-rays will be produced during inelastic interaction of the electron beam with the sample. This backscattering reduces the energy of the electrons within the beam until they are brought to

rest within the sample. The depth at which this takes place is termed the penetration depth. Beyond this depth, information cannot be obtained regarding the sample composition (Egerton 2005). Casino v2.51 was used in this work to model the interactions of the electron beam with the sample. Casino is a well-documented Monte Carlo simulation tool (Sokolov, et al. 2016) that allows the user to simulate the electron trajectory within the sample upon providing the details of the sample composition and electron beam energy and width used. It simulates enough electron trajectories that the user can determine at what depth the x-ray signals observed by the detector had been generated. With inputs from this experimental work: a 1nm probe diameter, 2000 electrons, an accelerating voltage of 200kV and an example 100nm carbon particle, it was determined that the entire example particle would be well within the penetration depth. This simulated particle is larger than any particle observed in this work.

The obtained EDS spectra were reviewed qualitatively due to the selection of specific portions of the sample, those that appeared to contain ash. This selective analysis renders any quantitative analysis useless. Peak detection within the spectra was determined by first assigning each observed peak an element as determined by well documented values provided by EDAX, the manufacturer of the EDS system. This was followed by ensuring the peak was within three sigma of the background and lastly confirmed through the presence of both an alpha and beta peak for the element in question, with the exception of carbon and oxygen as they would not have a second beta peak. Regarding the alpha and beta peak differences, an example will be given to highlight their meaning and the reason both peaks exist. Say an atomic electronic transition occurs for a “K” or innermost electron shell, the electron will either transition from the second shell to the inner “K” shell and release a K-alpha emission line, or the electron will

transition from the third shell to the inner “K” shell and release a K-beta emission line.

Therefore, researchers suggest a good technique for confirming the existence of an element is through confirming the presence of both peaks.

Detection of lubrication materials and engine wear metals was approached broadly at first, through comparisons of dark field and bright field digital images taken with the JEOL 2100 microscope. Metals can be detected through the presence of a bright spot in the digital dark field image with a corresponding dark spot in the digital bright field image. An example of this is given in Figure 10.

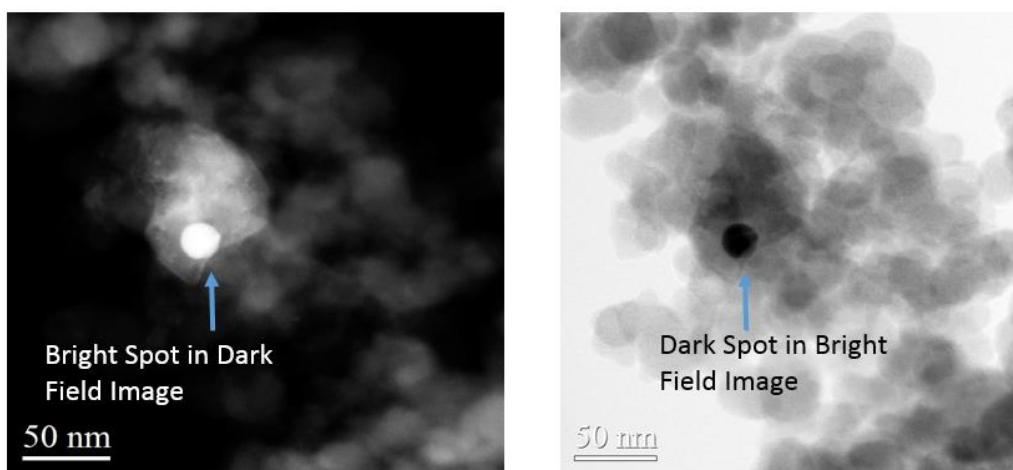


*Figure 10. Example of Comparison of Bright and Dark Field Images for Ash Detection*

Sections of the soot particles that appeared to have metals and sections for which there was uncertainty were subjected to spectra collection using the EDS system. In addition, the most interesting samples were analyzed using elemental mapping, for which x-ray counts for specific elements were retrieved for each point of the sample in the beam path and placed onto a discretized image matrix. Images were created showing a specific elements distribution



throughout the analyzed sample portion as well as overlays of all relevant elements. Images without the presence of metals were used to understand the background for the detected metal elements. It was determined that the background noise for the images taken during elemental mapping was on average 83 pixels with a standard deviation of 34 pixels. Given the images contain 232,521 pixels, this comes to 0.04% of the image.

### **3.6.6 BET Specific Surface Area**

Brunauer-Emmett-Teller (BET) surface area is a technique used for the measurement of specific surface area. It attempts to provide information regarding the physical adsorption of gas molecules on a solid surface. In this case, nitrogen is used as an adsorbate. The sample is kept at the boiling point of the adsorbate so that the adsorbate gas will condense on the sample thus creating uniform layers. Any decrease in pressure should result in desorption of nitrogen. Given the adsorption dependence on pressure and the known size of nitrogen atoms, the specific surface area can be determined as the pressure of the sample is changed.

For this work, a Nova 4200e BET surface analyzer was used. Nitrogen as an adsorbate was used at a temperature of 77 °K, the atmospheric boiling point of nitrogen. Analysis time for the sample runs was around 3 hours per sample. The relative pressure range (P/Po) used for the BET surface area calculations were different for each sample but within 0.0060 P/Po and 0.065 P/Po. Values for the BET calculations were taken at seven different relative pressures within the relative pressure range mentioned. The minimum relative pressure resolution for this instrument under the testing conditions specified is  $2 \times 10^{-5}$  P/Po.

Given the cost and time necessary to complete a measurement, hundreds of dollars and days at a time, only one measurement was taken for each sample and no reference sample was analyzed. Error was determined in previous works for which a standard material with a known surface area was evaluated across several laboratories (Hackley and Stefaniak 2013). Measurement error was found to be +/- 5% of the certified surface area and this value is used for error bars applied to data in this work.

### **3.6.7 Inductively Coupled Plasma – Mass Spectrometry**

Inductively coupled plasma – mass spectrometry (ICP-MS) is a mass spectrometry technique capable of detecting metals and several nonmetals at ultra-low values. This technique ionizes the sample with inductively coupled plasma then uses a mass spectrometer to separate and quantify the present ions. In this work, engine oil samples were sent to Shell for analysis of additives present. Analysis using ICP-MS followed the ASTM – D5185 procedure. Below is a table of the repeatability and reproducibility values for the various elements found in the oil analyzed. In Figure 11 these values are given as a percentage of the average value found during the sample analysis. As can be seen from the figure, the specific analysis of oil using the ASTM D5185 procedure has been found not to produce highly accurate answers but rather a general direction for the values present in the oil sample.

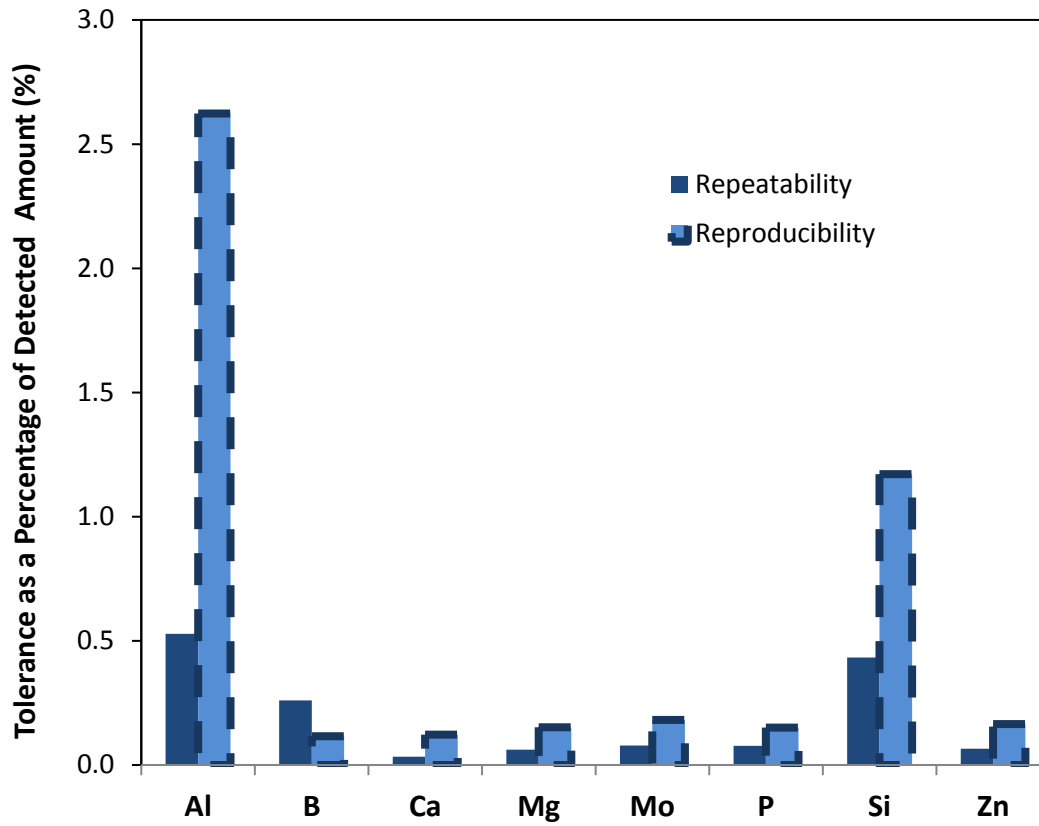


Figure 11. Repeatability and Reproducibility of ICP-MS Analysis on Engine Oil Sample by Element

## **Chapter 4. Particulate Matter Reactivity**

### **4.1 Isothermal Oxidation**

Soot reactivity was explored with a SDT Q600 Thermogravimetric Analyzer (TGA). Soot samples were loaded into the ceramic crucible of the TGA and oxidation experiments in ultra-zero air were performed through isothermal conditions at 500 °C, 550 °C and 600 °C. Figure 12 contains the results from that oxidation work. The normalized soot mass,  $m_n$ , was used to compare samples.

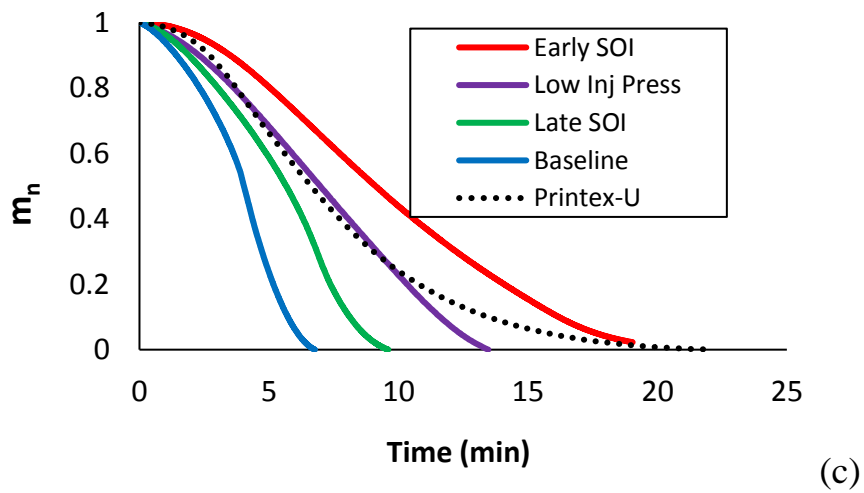
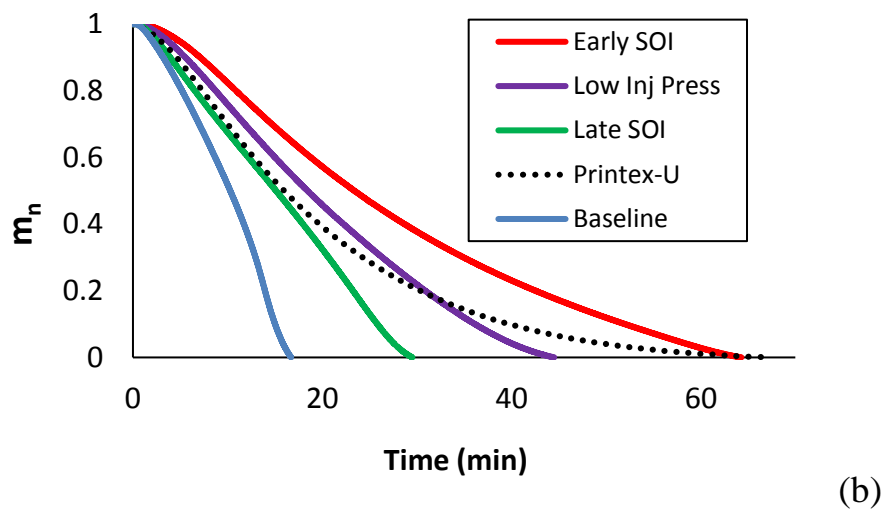
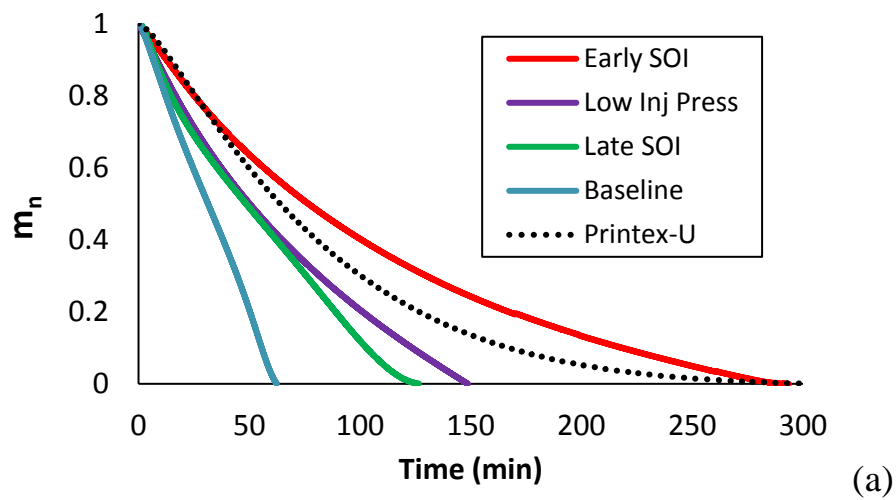


Figure 12. Isothermal Oxidation Events in TGA for Soot Samples in Ultra-Zero Grade Air:  
 (a) 500 °C, (b) 550 °C, (c) 600 °C

When reviewing Figure 12, it can be seen that variations in the soot reactivity exist between all samples. These variations persist for all oxidizing temperatures. For all isothermal conditions, the following reactivity order followed for the four operating conditions, given in order from most to least reactive: Baseline > Late SOI > Low Inj Press > Early SOI. The Printex-U showed a different oxidation profile from the four soot samples and was consistently less reactive than the low injection pressure condition and more reactive than the early start of injection condition. It is interesting that the Printex-U, model soot, was more reactive than the gasoline soot samples as the model soot should have a much lower volatile organic fraction, no ash and likely, a more ordered structure. Other researchers also identified this trend, and they have proposed this may be due to a unique soot structure for gasoline soot that is not well understood. This unique structure is assumed given the unique matrix bound organics found for GDI soot (Choi and Seong 2015). Given previous literature in which soot from conventional ultra-low sulfur diesel fuel combusted at a low speed and load was evaluated regarding reactivity (Sun 2017) in a very similar manner to this work, it seems that the variation in the gasoline soot presented here spans in reactivity to the diesel soot, with some conditions being more reactive and others being less reactive by comparison.

The  $t_{10-90}$ , or time it takes for the normalized soot mass value,  $m_n$ , to go from 0.9 to 0.1 in minutes, was calculated for all operating conditions and is given in Figure 13. The values at 500 °C, the lowest temperature condition and therefore highest resolution in oxidation times, are used in future correlations to soot reactivity. Figure 13 further highlight the change in oxidation rates with temperature changes. The  $t_{10-90}$  times from oxidation at 600C are only 6%-9% of the values observed from oxidation at 500 °C.

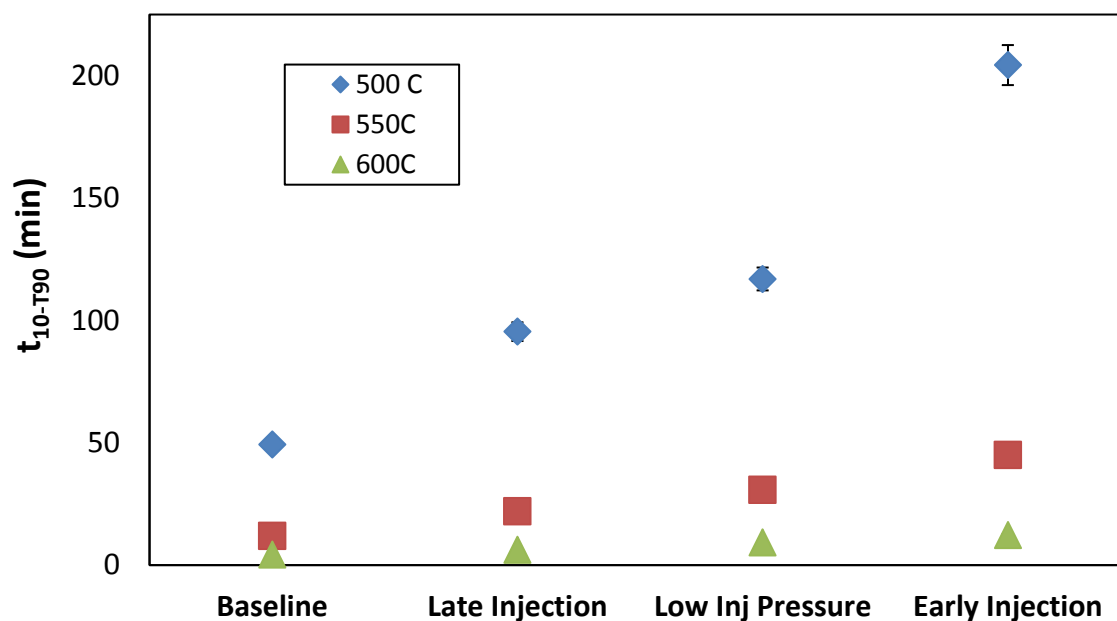


Figure 13.  $t_{10-90}$  Times for Soots from the Various Engine Operating Conditions

## 4.2 Temperature Programmed Oxidation

Soot reactivity was also evaluated by determining the light-off temperature of the soot samples in pure air using temperature ramps from 350 °C to 750 °C at a ramp rate of 1 °C/min. The results from these tests are given in Figure 14.

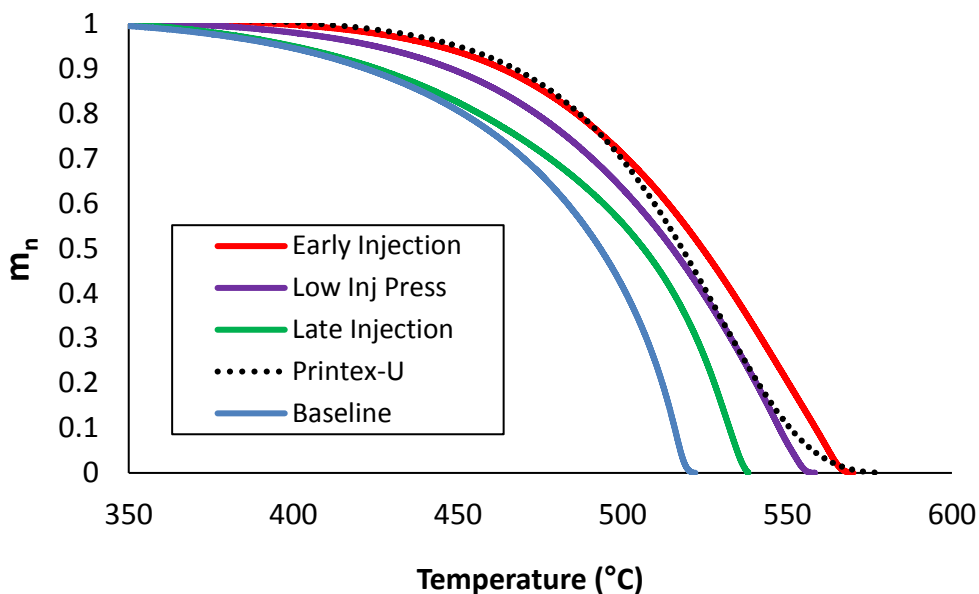


Figure 14. TGA Oxidation of Soot Samples using a Temperature Ramp.

The temperature ramp was not used for correlations to reactivity or derivation of kinetic parameters, but it is useful for understanding differences in the oxidation characteristics between samples. The baseline and late start of injection condition both reach light-off at a similar temperature, around 370 °C, though the baseline condition starts to oxidize more quickly at lower temperatures as they diverge around 450 °C. The low injection pressure condition reaches light-off around 400 °C. Both the Printex-U and early start of injection condition reach light-off around 425 °C, with a deviation in their oxidation rates occurring around 500 °C. It appears that some factor is causing the baseline, low injection pressure and late start of injection conditions to possess a lower light-off temperature than the model soot, while the early start of injection condition is not affected in this way.



### 4.3 Quantification of Reaction Rate Parameters

Reaction kinetics of carbonaceous soot are often resolved using fits to an Arrhenius-type equation (Stanmore, Brilhac and Gilot 2001). Within the research community, this seems to have developed into a commonly accepted form of quantifying the soot oxidation rates dependence on temperature. The details regarding this Arrhenius-type expression are given in Chapter 3. Experimental Set-Up. The final expression, Equation 5, pursued for obtaining the desired variables,  $E_a$ ,  $A$  and  $n$ , is given again.

*Equation 5*

$$\ln \frac{d\alpha}{dt} - n \ln(1 - \alpha) = \frac{-E_a}{RT} + \ln(A)$$

Slope and y-intercept values for linear regression fits to data in the plot of  $\ln (d\alpha/dt)$  vs.  $\ln (1-\alpha)$  are used to determine the necessary variables. The plot of  $\ln (d\alpha/dt)$  vs.  $\ln (1-\alpha)$  for the soot samples from the four operating conditions and Printex-U during oxidation in the TGA at 500 °C in ultra-zero air are given in Figure 15.

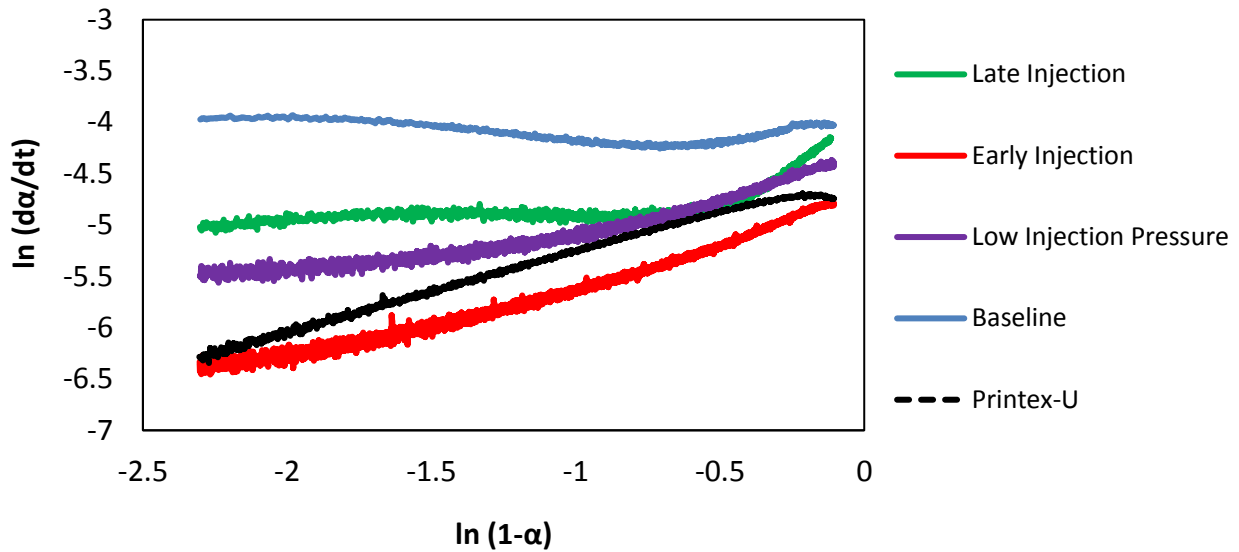


Figure 15. Comparison of Oxidation Parameters for a Fit to Arrhenius Type Equation using TGA Results from Iso-Thermal Oxidation at 500 °C

Though the Printex-U and early injection condition could support a linear regression, the other three conditions produce a very non-linear result. Thus suggesting the proposed variables,  $E_a$ ,  $A$  and  $n$ , would be obtained with high error. It is apparent something is affecting the oxidation rate in a fashion that is not consistent throughout the oxidation process. Given this result, a different approach was taken to pursue quantitative differences for the oxidation rate as discussed in Ch.3 Experimental Set-Up. The expression used to obtain the apparent rate constant, Equation 7, is given again.

Equation 7

$$\ln\left(\frac{m_n}{m_{n,0}}\right) = -k_s P_{O_2}(t - t_0)$$

A plot of  $\ln(m_n)$  vs  $t$  is given in Figure 16. Linear regressions to the data are used to obtain  $(-k_s P_{o2})$  through determination of the slope.

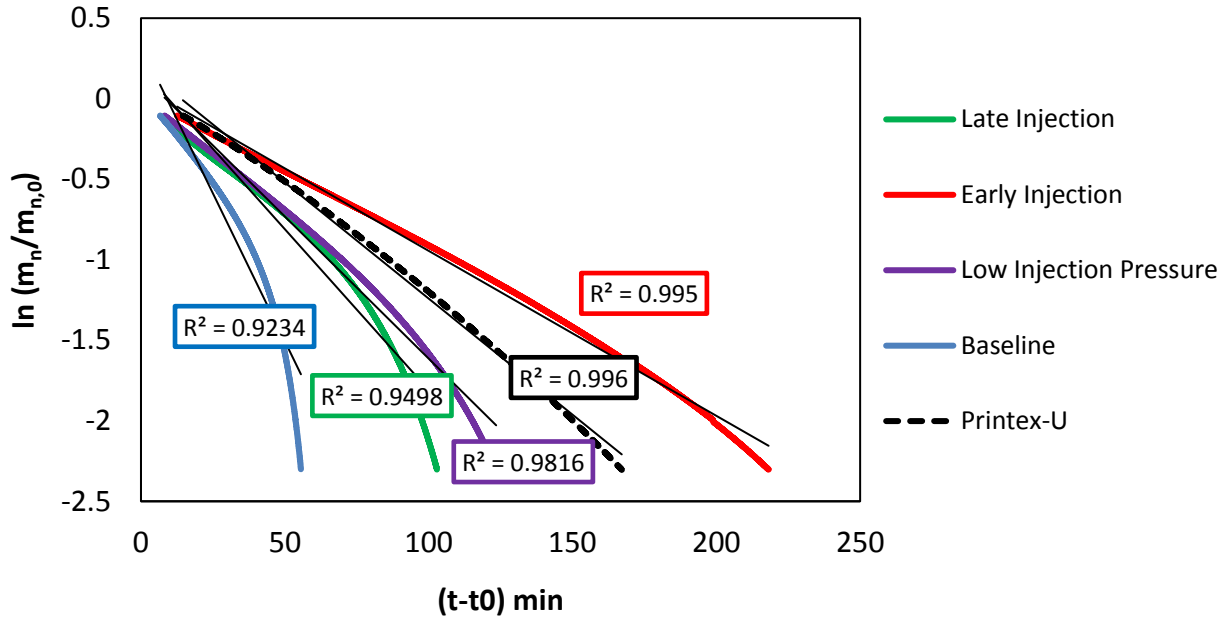


Figure 16. Curve Fits to Determine the Apparent Rate Constant

Again, the fits are linear for the early start of injection condition and the Printex-U case. Beyond this, the linear regressions begin to have low  $R^2$  values. Given this, the oxidation was broken into three sections and curve fits were again applied. These sections were roughly linear and had  $R^2$  values that were mostly above 0.99 with some fits still having values as low as 0.98. Table 5 provides values for these rate constants and their  $R^2$  values as determined by using the following intervals:  $m_n (0.9 \rightarrow 0.65)$ ,  $m_n (0.65 \rightarrow 0.35)$  and  $m_n (0.35 \rightarrow 0.1)$ . Essentially these intervals are the initial, middle and final thirds of the oxidation process.

Condition	Ox Interv	kc (1/(Pa/min))	R <sup>2</sup>
Late Injection	10%-35%	6.89E-07	1.00
Late Injection	35%- 65%	7.22E-07	1.00
Late Injection	65% - 90%	1.67E-06	0.98
Early Injection	10%-35%	4.36E-07	1.00
Early Injection	35%- 65%	4.31E-07	1.00
Early Injection	65% - 90%	5.53E-07	0.99
Low Injection Pressure	10%-35%	6.52E-07	1.00
Low Injection Pressure	35%- 65%	6.98E-07	0.99
Low Injection Pressure	65% - 90%	1.13E-06	0.99
Baseline	10%-35%	1.09E-06	1.00
Baseline	35%- 65%	1.45E-06	0.99
Baseline	65% - 90%	3.90E-06	0.96
PrintexU	10%-35%	5.34E-07	1.00
PrintexU	35%- 65%	6.23E-07	1.00
PrintexU	65% - 90%	7.59E-07	1.00

*Table 5. Apparent Rate Constant Values from Three Portions of the Oxidation Profile*

## 4.4 Summary

The TGA was used to perform isothermal and ramped oxidation events. Through this, reactivity and soot oxidation profiles were explored for the four operating conditions and compared to Printex-U, a model soot. From the most reactive to the least reactive, the following order was determined: Baseline > Late SOI > Low Inj Press > Printex-U > Early SOI. Light-off temperature was different among samples, with all gasoline soot samples having a lower temperature in reference to the Printex-U, with the exception of the early start of injection condition. It appears the factor influencing reactivity may also lower the temperature by which oxidation may occur. This factor may not be present for the early start of injection condition.

A linear regression fit to data using an Arrhenius type equation or an apparent rate constant for three of the operating conditions, baseline, low injection pressure and late start of injection, was not possible without high error. These soots may possess a factor influencing reactivity that was not dependent on temperature alone, but also on the amount of soot present. This is counter to what has been observed for other works using carbonaceous soot, as variables determined through linear regressions are commonly used for Arrhenius type expressions and apparent rate constants with good results. Given this, the oxidation process was broken into three parts. Linear curve fits could then be obtained, followed by the determination of an apparent rate constant for each third of the oxidation process. The early start of injection and Printex-U did produce linear regressions without the need to portion the oxidation process, thus suggesting their oxidation process is not affected in the same manner as the others. Furthermore, any discussion within this document regarding reactivity trends will use the  $t_{10-90}$  time, the time it takes for the normalized soot mass to go from 0.9 to 0.1, as this is the most intuitive value collected in the reactivity analysis.

## **Chapter 5. Impact of Operating Conditions on Combustion and PM Properties**

### **5.1 Combustion**

Combustion was not affected to a large degree by the changes in the various operating conditions. The coefficient of variation for the indicated mean effective pressure was maintained below 2% so that combustion stability was kept. This was the limiting factor for the set points of the low injection pressure and late start of injection event. The pressure traces for the four operating conditions as taken by the in-cylinder pressure sensor located in cylinder 1 are given in Figure 17.

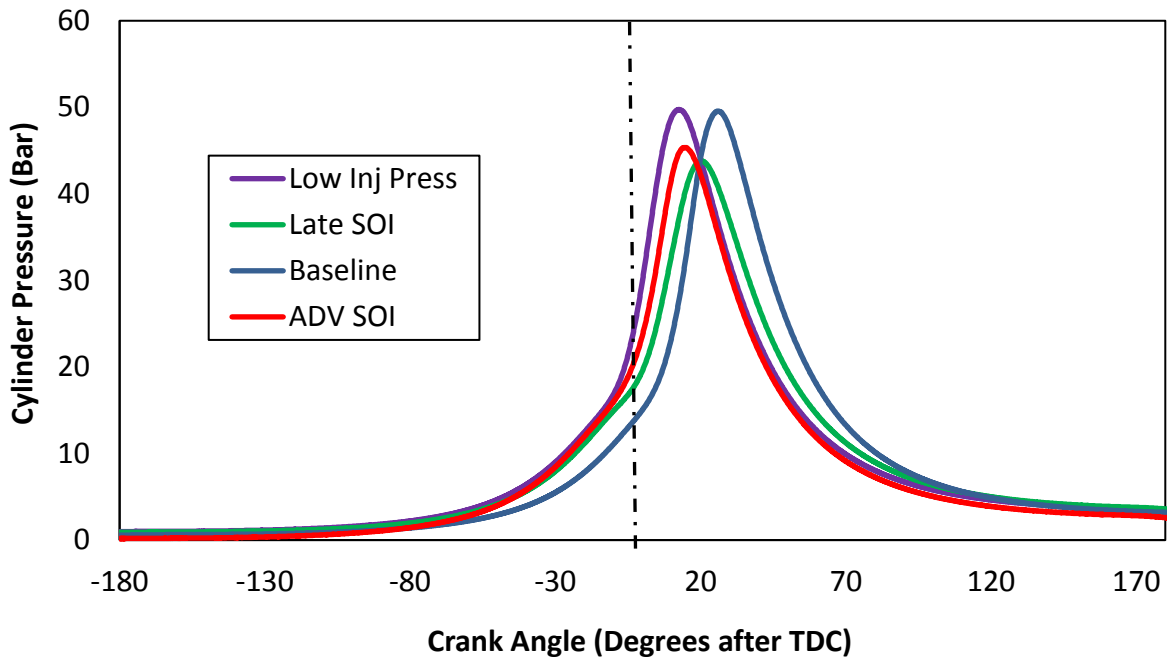


*Figure 17. In-Cylinder Pressure Trace for All Four Operating Conditions*

The pressure traces in Figure 17 differ marginally from each other. Each trace is an average of 10 to 15 cycles. It is clear that though the fuel/air mixing are very different for the four operating conditions, combustion was not dramatically impacted. As the operating conditions were selected to represent realistic combustion conditions, achieved through low coefficient of variation for the indicated mean effective pressure, these similarities are to be expected. Any variability present is likely due to data being taken on different days at different test cell temperatures. It may be expected that with aggressive late injection timing and low injection pressure, the combustion would eventually shift to a more broad pressure trace with a peak occurring at later crank angles as it would take longer for the fuel within local fuel rich areas to become oxidized. However, the operating conditions within this work were not aggressive enough to produce such a result within combustion.

## 5.2 Particulate Emissions

Particulate emissions were evaluated for particulate number and carbonaceous soot content differences among the four samples. The effect of fuel injection parameters on the particulate formation rate is key to this body of work. The effect, if present, would be observed in both the number and size of particles formed and the amount of carbonaceous soot that was formed.

### 5.2.1 Particle Size Distribution

The particle size distribution was determined with a TSI Scanning Mobility Particle Sizer (SMPS). Data was collected using the SMPS for all four operating conditions and is shown in Figure 18.

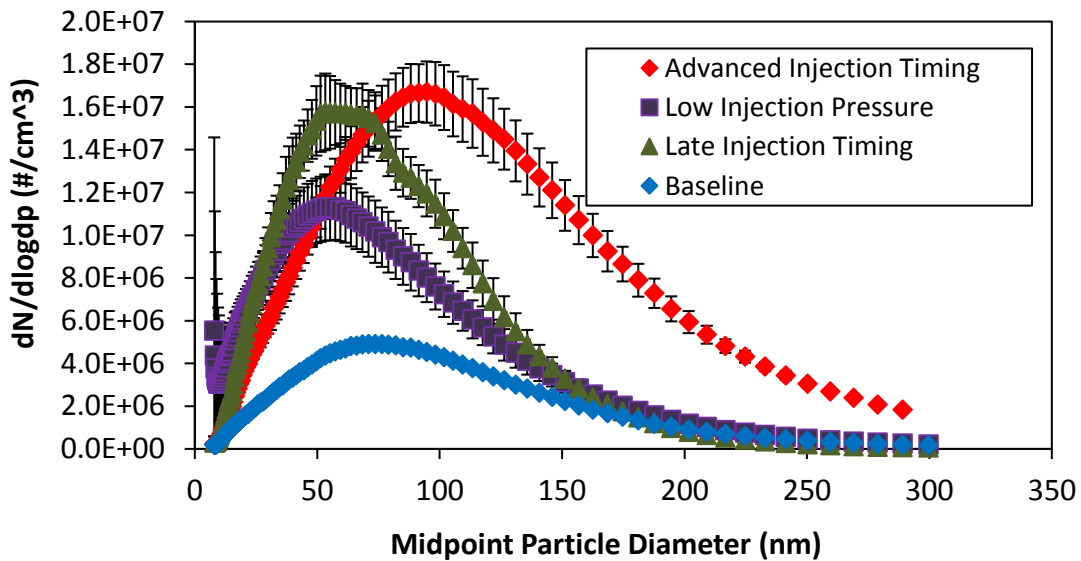


Figure 18. Particle Size Distribution for the Four Operating Conditions



From Figure 18 it can be observed that the four operating conditions produce different distributions of particle sizes. The baseline condition produced the lowest particulate number with a peak occurring near 71 nm. This was followed by the low injection pressure, where the peak particle size shifted to 55 nm. The late start of injection condition produced a higher number of small particles with a peak shifted to 57 nm, but it contained less large particles as those in the low injection pressure condition. The early start of injection condition contained less small particles as the late start of injection condition, however it had a peak particle size near 91 nm and significant values for the large particle size range, well above the other three operating conditions. Impact of operating condition on particle size formation will be discussed later in this document.

### **5.2.2 Soot Concentration**

Carbonaceous soot concentration was determined using an AVL Filter Smoke Meter and correlations of the Filter Smoke Number (FSN) to soot concentration using the Christian Correlation. The results from the four operating conditions are shown in Figure 19.

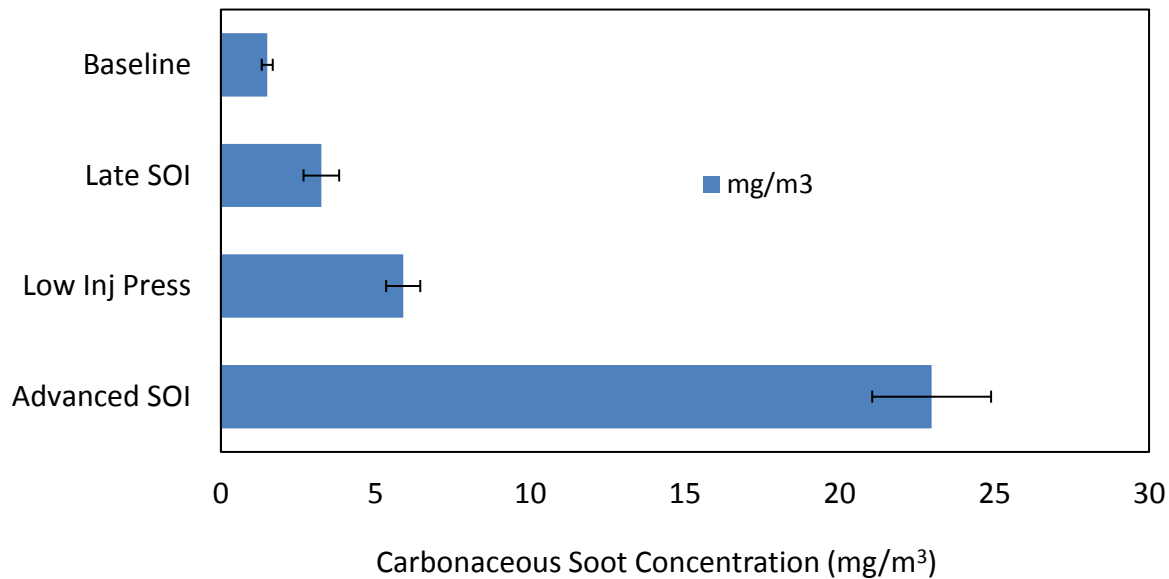


*Figure 19. Soot Concentration from the Four Engine Operating Conditions*

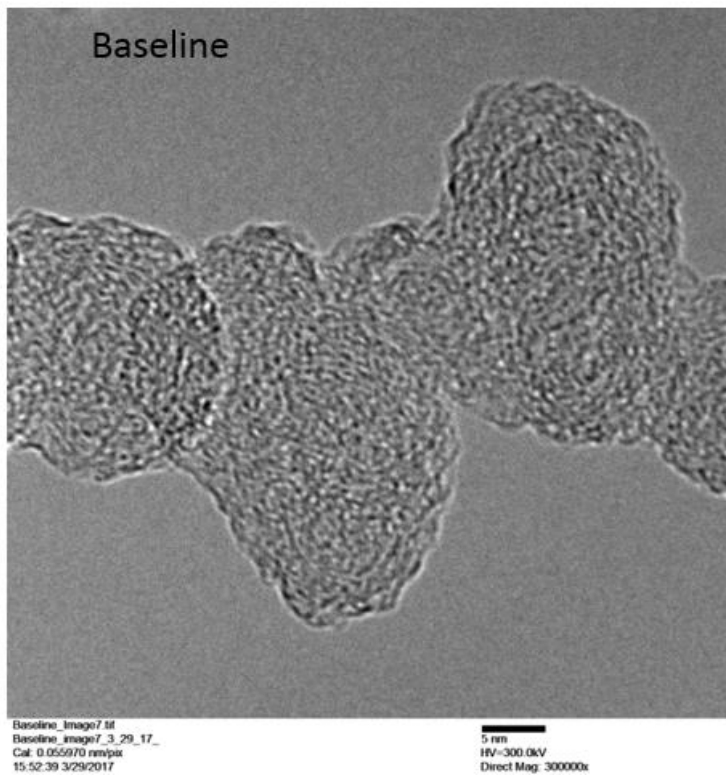
Engine out soot concentrations were lowest for the baseline condition as air/fuel mixing and formation of fuel rich areas are the most limited in this case. Following baseline, the soot concentrations increase in the following order, from lowest soot concentration to highest: Late SOI < Low Inj Press < Early SOI. When fuel is injected late it may impinge on the cylinder walls as the piston is no longer used to enhance mixing, thus resulting in fuel rich areas at the cylinder wall. There is also less time for mixing for the late start of injection condition, thus generating more fuel rich areas within the combustion chamber. For the low injection pressure condition, fuel droplets are larger in size and less atomized, therefore resulting in a larger portion of the fuel in a fuel rich area within the droplets. Regarding the early start of injection, the greatest value in soot concentration was found, with a value 15 times that of the baseline case.

## **5.3 Nanostructure**

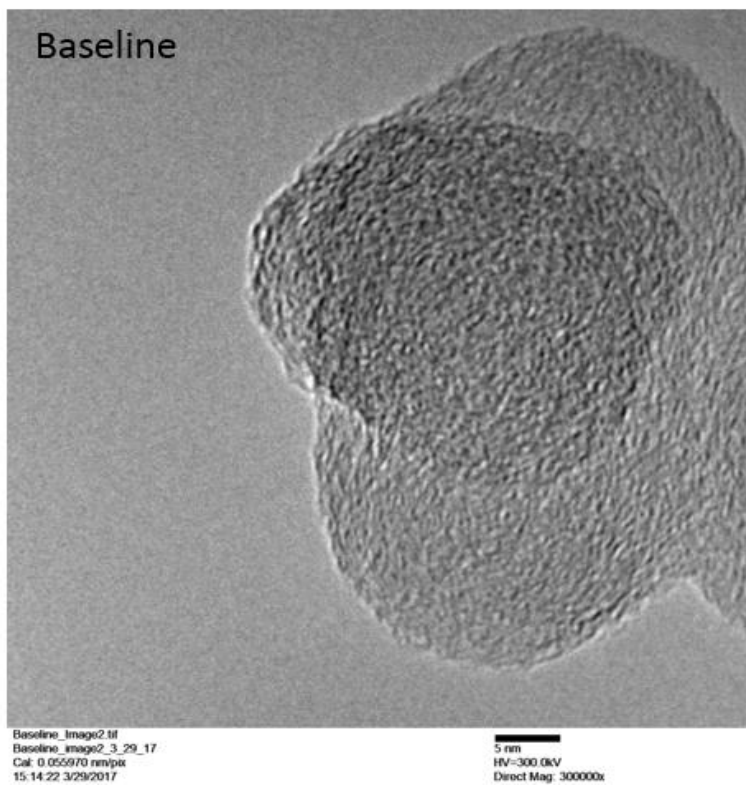
Soot nanostructure was qualitatively evaluated through analysis of high-resolution TEM images and semi-quantitatively analyzed through Raman spectroscopy and comparisons between ordered and disordered peak heights and areas.

### **5.3.1 TEM**

Figure 20, Figure 21 and Figure 22 show selected TEM images from the soot analysis. Imaging was done using an ultra-high resolution capable transmission electron microscope at a magnification of either 250k, 300k or 350k. All of the images collected for each operating condition were similar to the two respective images shown and no anomalies regarding nanostructure were found. These selected images are used to highlight the findings. Soot was analyzed using TEM for three operating conditions: late start of injection, baseline and early start of injection.

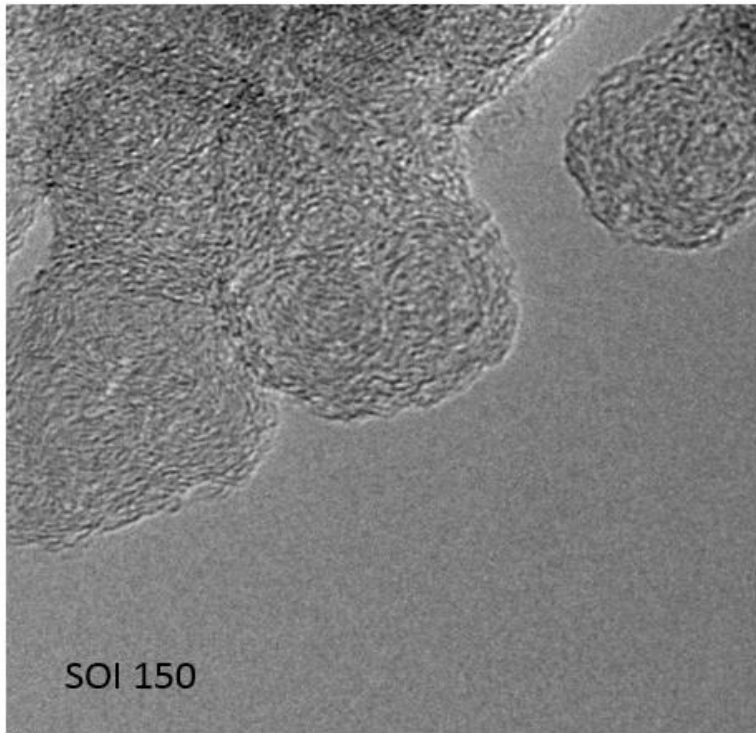


(a)

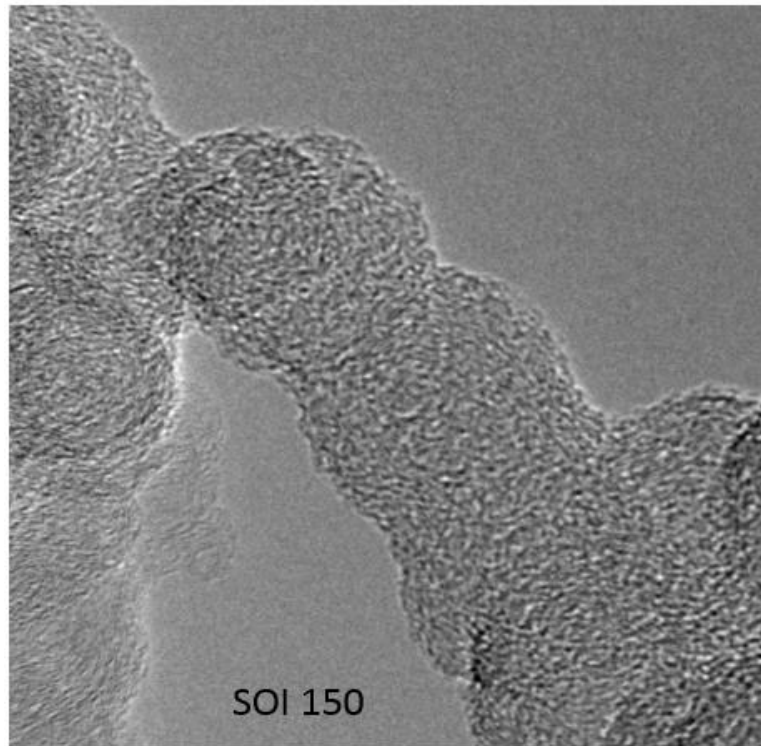


(b)

Figure 20. TEM Imaging Results from the Baseline Operating Condition: (a), (b)

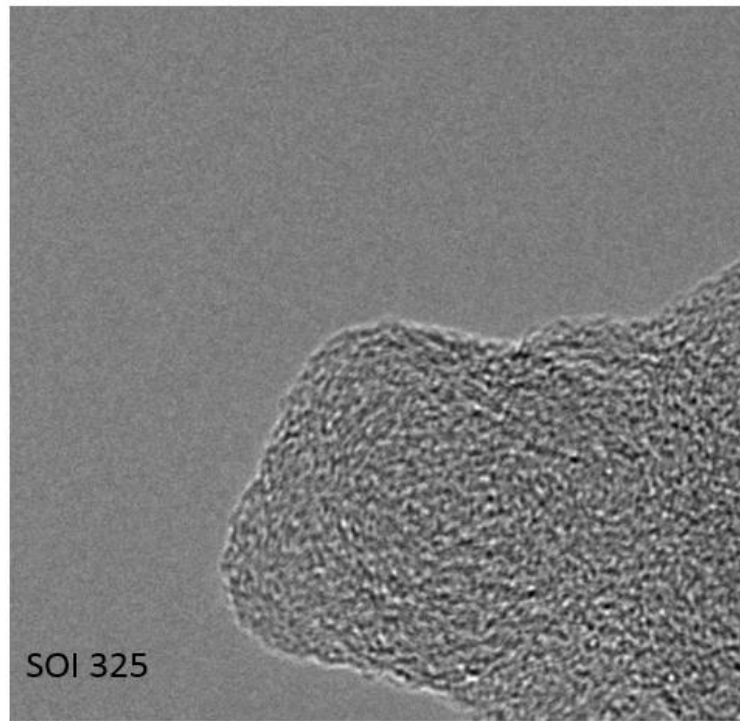


(c)

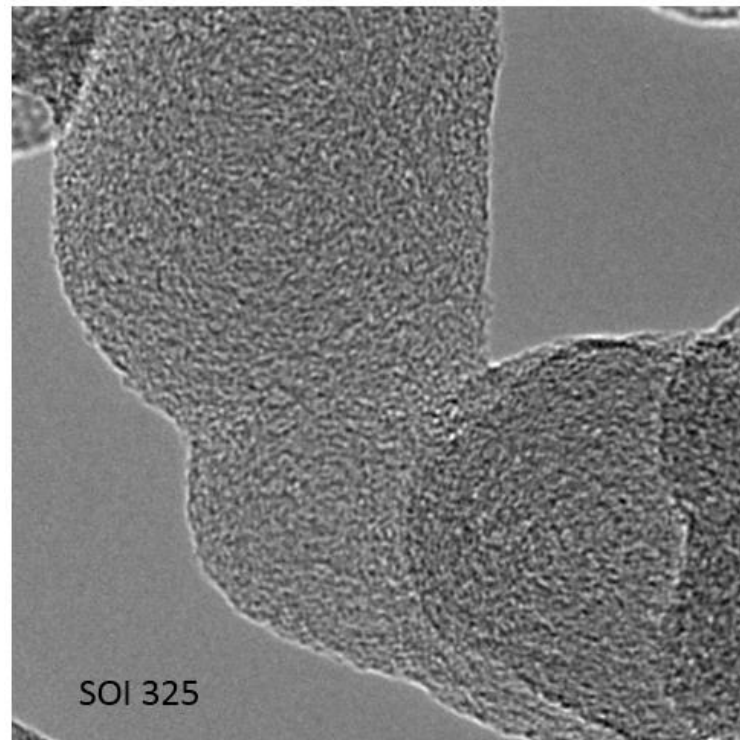


(d)

Figure 21. TEM Imaging Results from the Late Start of Injection Operating Condition: (c), (d)



(e)



(f)

Figure 22. TEM Imaging Results from the Early Start of Injection Operating Condition: (e), (f)

A well-ordered carbon particle could be identified by concentric long fringes with short interlayer distances that would layer around the nucleus of the particle like the layers of an onion. The soot from these operating conditions appears to lack this order and are highly amorphous in nature. This observation can be made for all three samples analyzed.

Previous researchers have also found soot from gasoline direct injection engines to be amorphous in nature (Miyashita, et al. 2015), (Liati, Schreiber, et al. 2016). This is likely due to higher rates of organics bound to the soot matrix, observed in GDI soot (An, et al. 2016), that prevent the growth of graphene segments, lower temperatures during formation ( $< 1250$  °C) and a lack of high temperature exposure after soot formation to support rearrangement of graphene segments to a more ordered structure (Zhu, et al. 2005). Previous works have found that the soot from gasoline is formed late in the combustion event and at lower temperatures. To help explain this, may the reader think back to the fuel puddles and films outside of the pre-mixed flame front. In these regions gasoline soot may form, as opposed to the rich fuel jet entering a diffusion flame from which diesel soot arises (Bogarrra, et al. 2017). These low temperature conditions have been found to produce highly amorphous soot regardless of fuel type as PAH formation dominates soot formation (Vander Wal and Tomasek 2004). As the factor of low temperature would be present for differing injection pressures and timings, regardless if soot formation rates were increased, it makes sense that these parameters may have minimal impact on soot nanostructure.

Previous researchers have successfully applied image analysis techniques to obtain quantitative fringe lengths and curvature values for soot samples (Yehliu, Vander Wal and Boehman 2011). However, given the highly amorphous nature of the soot samples for our

analysis, this did not seem feasible. As a result, Raman spectroscopy was utilized for a semi-quantitative comparison of soot nanostructure for the four samples. TEM analysis was not performed for the low injection pressure case as it was assumed to have a highly amorphous nanostructure given its similarity to the previous conditions regarding the soot formation process. This was confirmed with Raman before determining to leave this nanostructure out of the TEM analysis.

### **5.3.2 Raman Spectroscopy**

Raman spectroscopy has been used in a variety of work to analyze the nanostructure of carbon samples as it is sensitive to orientation and type of carbon bonding (J. Song, et al. 2006), (Schwan, et al. 1996). In this thesis, Raman spectroscopy was performed on samples from all four operating conditions: low injection pressure, early start of injection, late start of injection and baseline. The Origin 2016 Peak Analysis toolset was used for all curve fittings. An example, through the baseline case, of the curve fitting and peak identification results are given in Figure 23. All other spectra with overlaid curve fits are given in Appendix A for transparency.



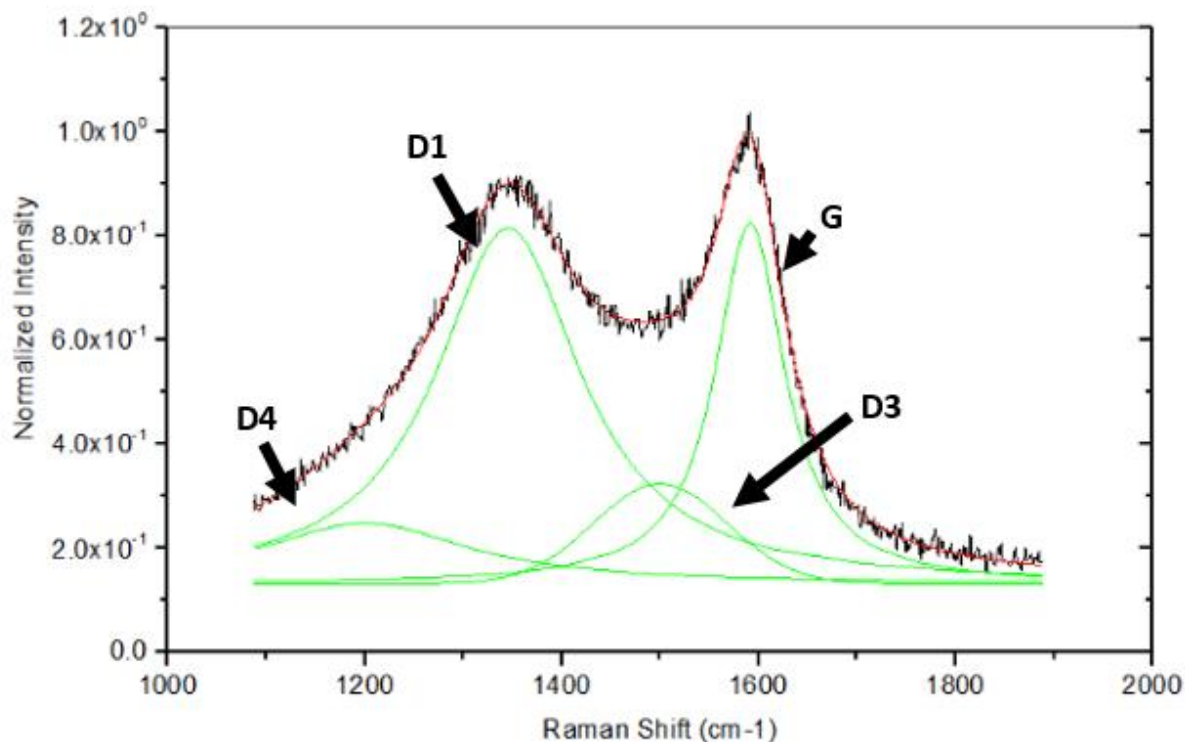


*Figure 23. Peak Analysis Performed on Baseline Raman Spectra*

The various D peaks represent some aspect of nanostructure disorder whereas the G peak represents the graphitic portion of the sample. The D1 peak has the highest peak intensity and largest area of the D peaks and represents the disordered graphitic lattice. The ratio of areas for the D1 and G peak and the ratio of peak intensities for the D1 and G peak are commonly used to compare the nanostructure of carbon samples and so used in this work. The values for the  $A_{D1}/A_G$  (ratio of areas for the two peaks) and  $I_{D1}/I_G$  (ratio of intensity for the two peaks) are given in Figure 24. A higher ratio of either would suggest a more disordered, or less graphitic, nanostructure.

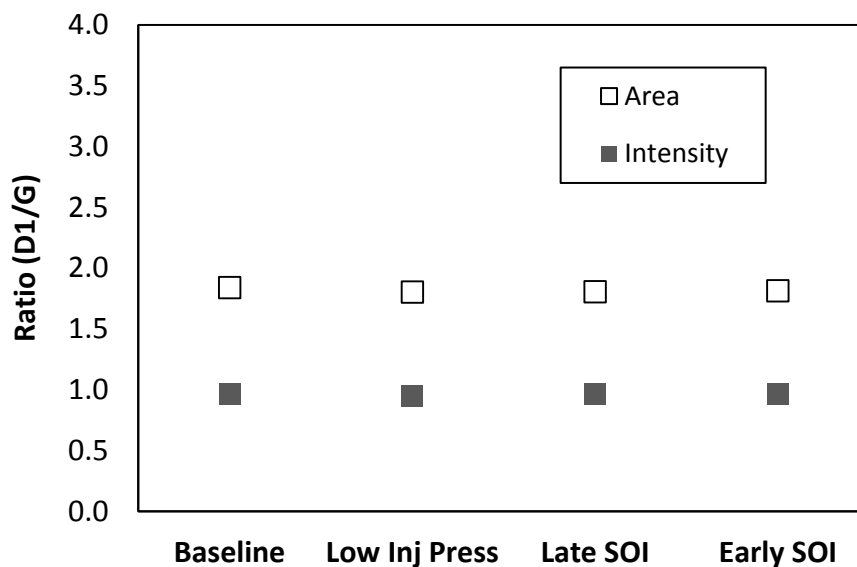


Figure 24.  $A_{D1}/A_G$  and  $I_{D1}/I_G$  ratio for the Four Operating Conditions

Error bars based on the standard deviation of the five measurement samples are included, however the variability was found to be small, smaller than the outline of the marker itself. It may be important to note that this deviation even included samples taken from different parts of the bulk soot loaded in the instrument. The four conditions are very similar in their nanostructure as suggested by the close ratio values. It is also noted that the area of the D1 peak, disordered nanostructure, is close to double that of the G peak, graphitic nanostructure, though intensity peaks are nearly 1:1. This aligns closely with the TEM images suggesting that the GDI soot nanostructure from the four different operating conditions are quite amorphous with little observable differences.

## **5.4 Surface Area**

Some works have indicated that active surface area, effective surface area based on the material's ability to take on an electrical charge, will relate to carbon oxidation (Radovic, Walker and Jenkins 1983). The correlation of reactivity to specific surface area is uncertain (Ye, et al. 2016), (Leidenberger, et al. 2012) despite active surface area being a function of specific surface area. Given these uncertain findings and the lack of evaluation regarding surface area for gasoline particles, it seemed important for this thesis. For this work, specific surface area was reviewed as it is easier to measure than active surface area. This was performed first through TEM images to review if any differences in particle size existed. As the TEM results suggested a difference in surface area would exist, the soot samples underwent BET analysis using a Nova 4200e BET surface analyzer.

### **5.4.1 Primary Particle Size - TEM**

TEM images were taken with a JEOL 3011 ultra-high resolution capable transmission electron microscope set at magnifications between 60k and 85k for analysis of primary particle size. Figure 25 presents the results in images from the four operating conditions.

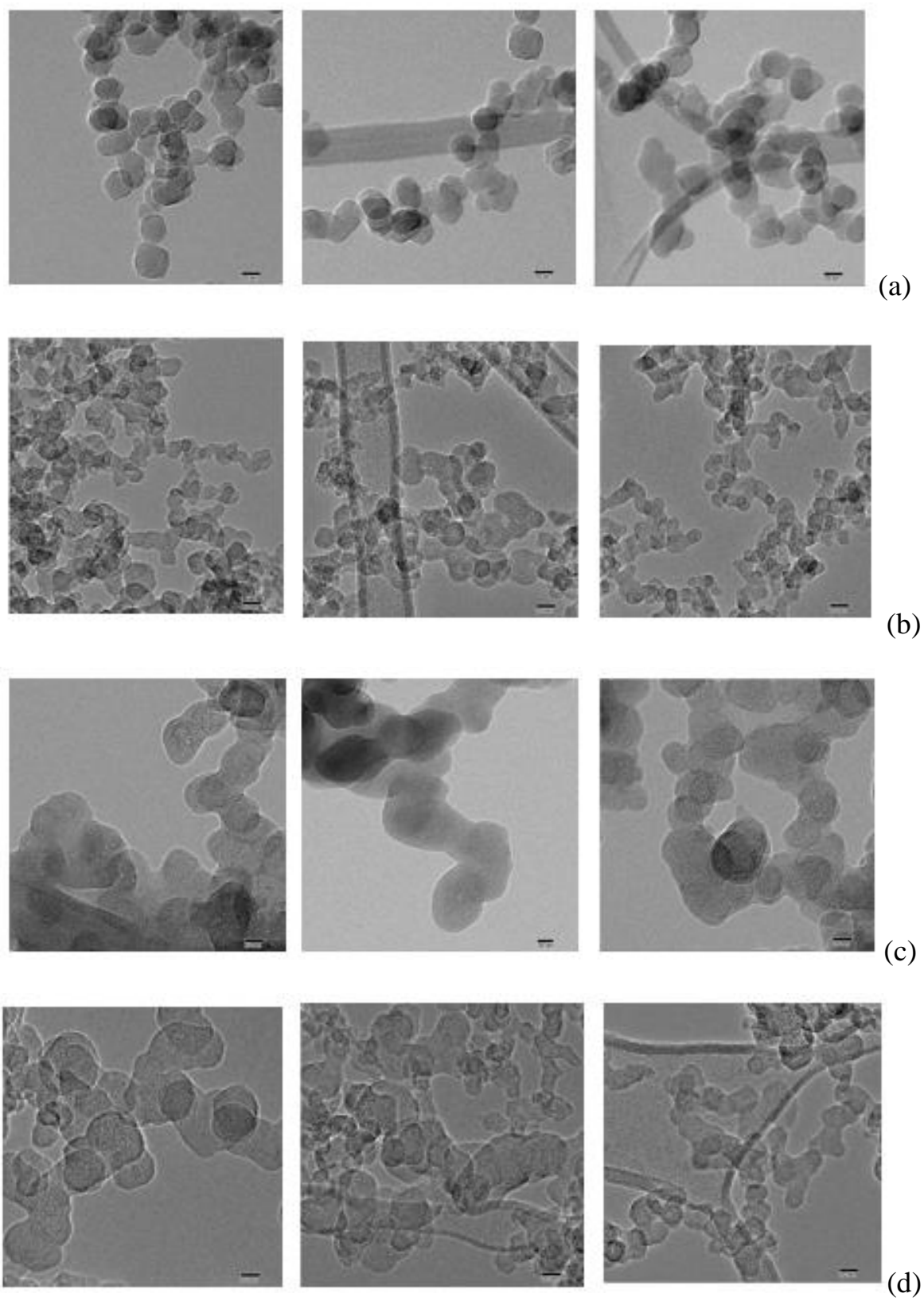


Figure 25. TEM Images of Primary Particles at 60k-85k for (a) Baseline (b) Late Start of Injection (c) Early Start of Injection (d) Low Injection Pressure.

In reviewing primary particle size for the various operating conditions as given in Figure 25, it becomes apparent that changes in fuel introduction parameters influence primary particle size. The baseline condition was comprised of aggregates of similar particle size, mostly near 20nm - 25nm, with some smaller primary particles present on occasion. As the fuel was introduced later, for the late start of injection case, the primary particles become smaller, mostly 10nm – 15nm in diameter, though there are still some particles present at this condition that are close to the average size of those from the baseline condition, just much fewer in number. As the fuel was injected earlier than the baseline condition, early start of injection, the primary particle size changed dramatically. Though there remained many particles near the 20nm size range, a number of the primary particles were in a 30nm to 50nm size range. The low injection pressure condition produced a mixture of particles unlike the other conditions. Many of the particles appeared to have a smaller primary particle size, similar to the late start of injection, while many other particles were noticeably larger, larger even than the baseline condition, reaching 30nm to 50nm. It may be assumed that the primary particle size average and trend of decrease in surface area as the average primary particle diameters increase are as follows: Late SOI < Baseline < Early SOI, while making any guess as to the placement of the low injection pressure condition is tricky given its odd mix of particle sizes. Detailed analysis regarding the primary particle size was not pursued as the end goal was a surface area value that would be obtained directly.

In addition, previous researchers such as Seong et al. have looked at the effect of injection timing, though not injection pressure, on primary particle size for a gasoline direct injection engine in detail (Seong, Lee and Choi 2013). Seong et al. also found that the baseline injection timing produced primary particles near 20 nm, while the late injection timing resulted

in smaller primary particles, 10nm – 20nm in size. It was also found that the early injection timing resulted in larger primary particles, increasing the average from 20nm to 29 nm. Furthermore, a steep increase in large particle sizes, near 50nm and 60nm, was noted. The primary particle sizes and the impact to those sizes by injection timing as identified in our work and the work by Seong et al. (Seong, Lee and Choi 2013) seem to be in good agreement, thus providing confidence in our quick assessment.

In the work by Seong et al., it was discussed that the differences in primary particle sizes are likely a result of a complex soot formation process within the GDI engine. It may be expected at conditions where fuel/air mixing is impaired, such as events when injection timing and pressure are adjusted, more particles will nucleate and this should result in larger primary particles as these particles collide. However, this was mostly the case for the early start of injection and some particles for the low injection pressure. It is odd that such small particles would arise from the low injection pressure and late start of injection condition. This may be due to exposure of these nucleated particles to low temperature regions early in the soot formation process where growth in particle size is quenched. For the late start of injection, quenching may be uniformly present as the soot formation region may be assumed mostly along the cylinder wall, but for the low injection pressure condition, it may be present in some areas and not others given the stratification of the fuel within the chamber, thus causing the large variations in observed primary particle size.

It is also interesting to note that the primary particle sizes observed here are similar to those found in diesel works, with most primary particles between 5nm and 25 nm (Liati, Dimopoulos, et al. 2013), (Lapuerta, Martos and Herreros 2007) at normal operating conditions.

Furthermore, it should be expected that the surface area would be different for these four operating conditions given such variations in primary particle size.

### 5.4.2 BET

Aggregate particle specific surface area is a product of primary particle size and primary particle overlap within the soot particle agglomerate. The larger the particle size, the lower the specific surface area. The more the particles overlap, the lower the specific surface area (Lall, et al. 2008).

To evaluate the specific surface area from the soot produced at the four operating conditions a Nova 4200e BET surface analyzer was used to perform BET analysis. The results of this analysis are given in Figure 26.

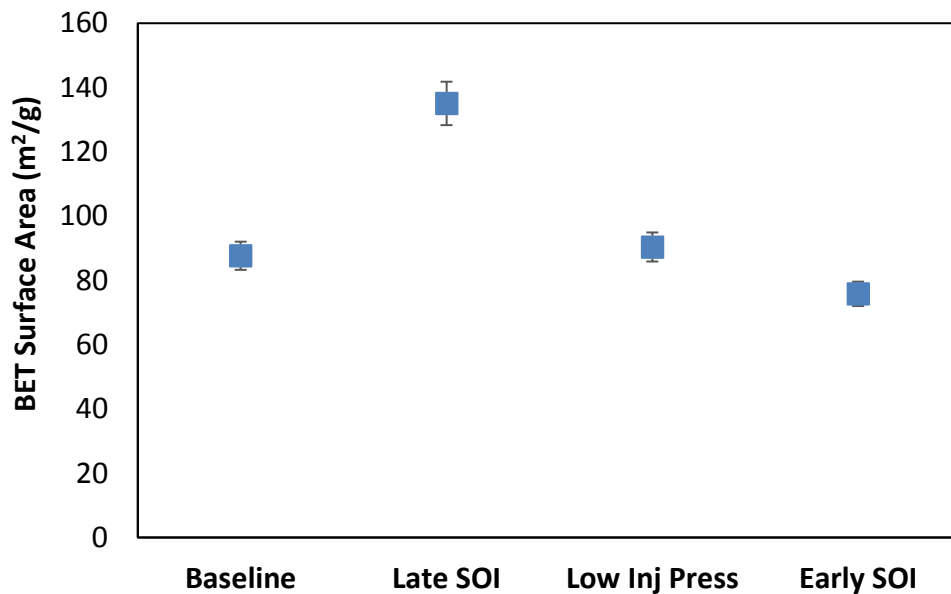


Figure 26. BET Surface Area

It is interesting to note that the trend in measured surface area did in fact match the proposed trend regarding estimated average primary particle size. The late start of injection conditions had the smallest primary particles and the highest surface area, with the baseline operating condition following with the next highest primary particle sizes and a decrease in surface area and the early start of injection condition following with the largest primary particle sizes and lowest surface area. It is also worth mentioning again that particle overlap will play a role in surface area, however, for all conditions in this work particle overlap seemed to be low as the primary particles formed branched aggregate particles with a high radius of gyration. As the primary particle size average was difficult to determine for the low injection pressure due to the mix of various large and small primary particles, the BET surface area for this condition was especially of interest. Regarding this condition, the specific surface area is slightly higher than baseline and quite lower than the late start of injection, suggesting that the average primary particle size was likely closer to the baseline condition.

In determining if the specific surface area correlated with reactivity, Figure 27 was generated. It compares the BET measured surface area to the  $t_{10-90}$  time measured during soot oxidation at 500 °C in ultra-high purity air.



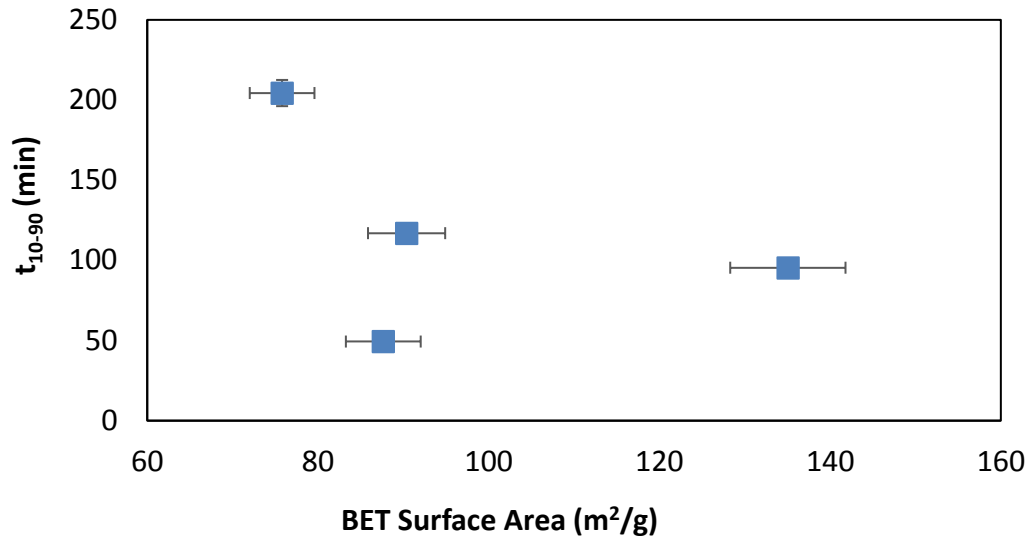


Figure 27. Comparison of Soot Reactivity to BET Surface Area

There is no observable trend with reactivity differences. If a correlation did exist, it would likely suggest a higher surface area would correlate to a higher soot reactivity, as more sites may be present for oxygen adsorption. It appears that surface area is not an important factor regarding the soot oxidation rate for these four samples.

## 5.5 Volatile Organic Fraction

The volatile organic fraction (VOF) often consists of unburned lubricating oils and hydrocarbons that coat the carbonaceous soot particles (Neoh, Howard and Sarofim 1984). For this work, the volatile organic fraction portion of the soot was evaluated through a devolatilization process completed using the TGA and inert Nitrogen gas at 500 °C.

Results from this analysis are given in Figure 28. The values for the volatile organic fraction of the soot are relatively low for engine out soot particles, with all values being less than 10%. The highest organic fraction occurs at the late start of injection condition, this is to be

expected as the late injection timing is the most likely to have high rates of unburned hydrocarbons given the inadequate time for fuel/air mixing.

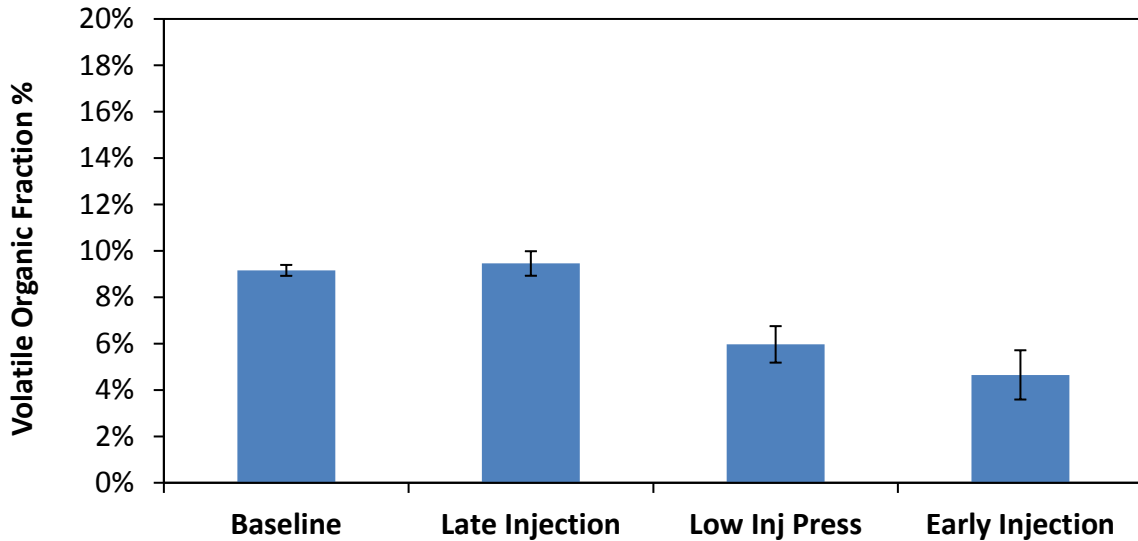


Figure 28. Average Volatile Organic Fraction for the Four Operating

Though low injection pressure does effect fuel atomization, creating bigger fuel droplets, it should not create the problems with fuel/air mixing seen by injecting the fuel late. The early injection timing will only aid with the fuel/air mixing process, with the exception of the fuel within the liquid puddle on the piston top. Therefore, it may be assumed that engine-out hydrocarbon values are relatively similar between the low injection pressure, early injection and baseline conditions. Given this, the volatile organic fraction order following the late injection event is likely a product of engine out soot rates. For the soot collected at the early injection timing, the ratio of soot mass to present hydrocarbons that may condense on the particle is much higher than for the low injection pressure case, and as would follow, the ratio of soot mass for

the low injection pressure case to surrounding hydrocarbons is higher than for the baseline case. This phenomenon may be responsible for the observed trend in volatile organic fractions.

It may also be mentioned that the trend somewhat matches surface area as measured by BET, as the highest surface area was found for the late injection condition and was lowest for the early injection case, though the baseline and low injection pressure conditions were close in BET and are quite different here. However, both the low injection pressure and baseline conditions fell in between the other two conditions for both the BET surface area and VOF analysis. These statements are presented to suggest that perhaps the surface area may measure the area available for hydrocarbons to condense and factors that relate to differences in specific surface area may additionally be factors contributing to variations in the VOF. The VOF did correlate slightly to the reactivity as measured by the  $t_{10-90}$  for the condition of air at 500 °C. This comparison is made in Figure 29. Previous works have suggested that increases in unburned hydrocarbons adsorbed onto the particle outer surface and filling the micropores may lead to increases in soot reactivity (Kandas, et al. 2005). Higher rates of porosity may develop after the de-volatilization process, thus resulting in higher internal surface area and possibly the formation of larger and turbostratic crystallites in the direction normal to the graphene layer as layers within the soot rearrange (Walker 1990). It seems unlikely this is contributing to the reactivity differences within samples given the one anomaly at the late start of injection condition and as VOF values are so low and close to each other.

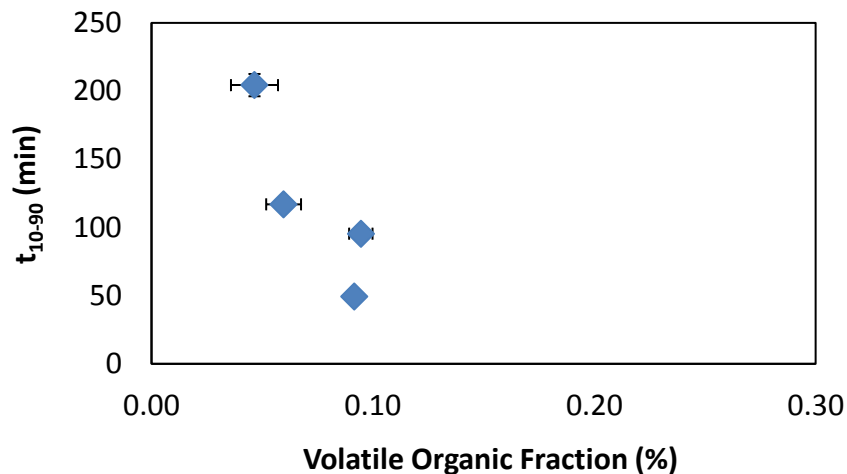


Figure 29. Comparison of Reactivity against VOF for the Soots from the Four Engine Operating Conditions

## 5.6 Chemical Composition

The  $Sp^2/Sp^3$  carbon hybridization, oxygen atomic percentage and oxygen surface functional groups were evaluated using XPS. Surface functional groups,  $Sp^3/Sp^2$  ratios and oxygen content of soot have been correlated to reactivity differences with soot oxidation. These research works suggest increases in soot reactivity match increases in levels of surface functional groups,  $Sp^2/Sp^3$  ratios and oxygen content (J. Song, et al. 2006), (Sun 2017).

Composition of the particulate samples regarding oxygen and carbon atomic based content are given in Figure 30 for the various operating conditions. Values are semi-quantitative and derived from areas integrated under the intensity peaks taken during the survey scan.

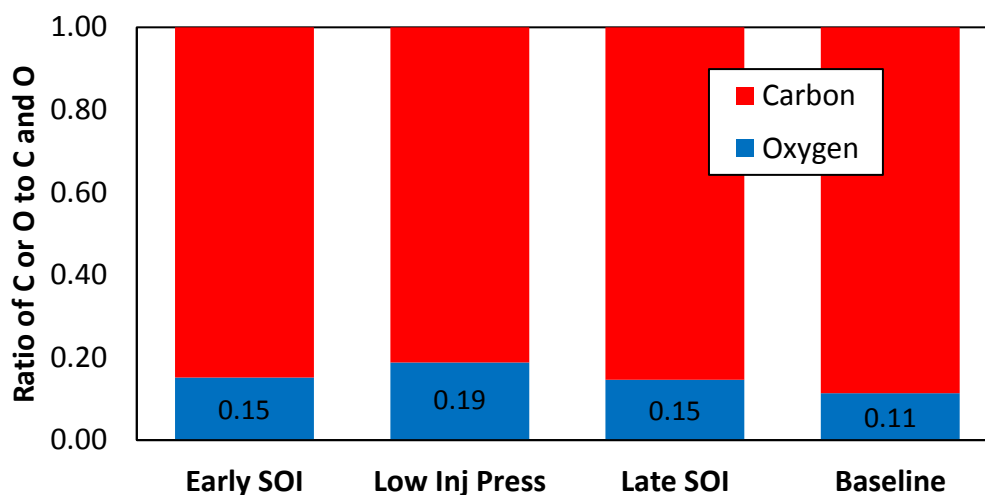


Figure 30. Carbon and Oxygen Values for Four Operating Conditions based on XPS

The values in Figure 30 represent the ratios of carbon (red) and oxygen (blue) to the total amount of carbon and oxygen found in the sample by XPS survey scans. The elemental contribution of oxygen is decently high, as may be expected by the highly amorphous nature and likely bonding of surface functional groups observed for the nascent soot nanostructure found for these gasoline soot particles. Previous works have reported an oxygen percentage anywhere from 2% to 25% for combustion derived soot (Vander Wal, Bryg and Hays 2011).

Core scans were taken over the C 1s and O 1s peaks to resolve more information regarding carbon and oxygen bonding. Peak deconvolution was performed to determine the amounts of the various carbon bonding. A peak deconvolution example is given from the analysis done with the early injection timing sample in Figure 31 and Figure 32.

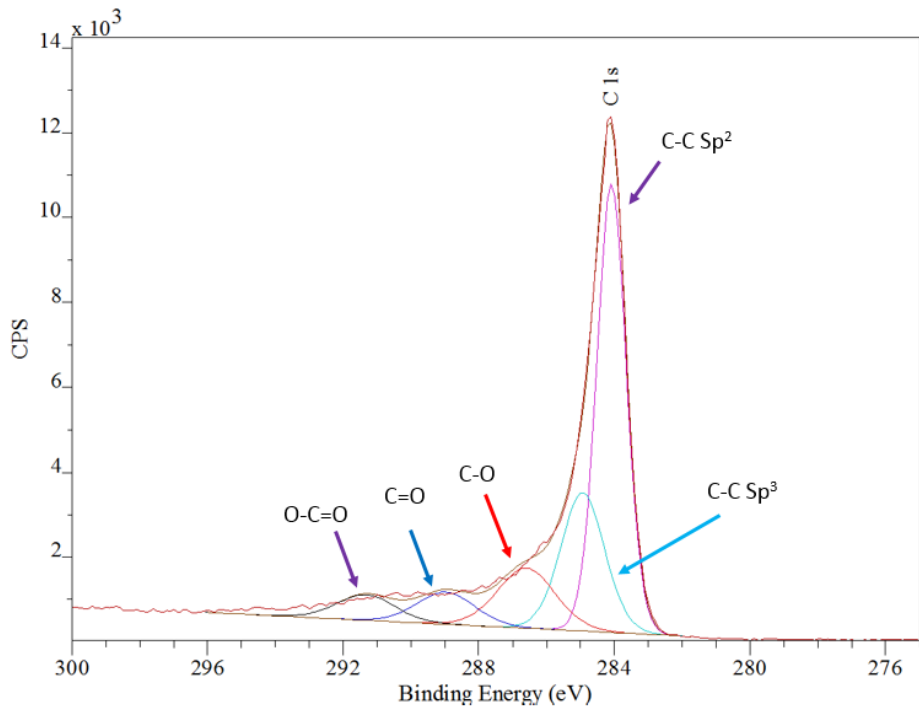


Figure 31. Peak Deconvolution for the C1s Peak (Early SOI Sample)

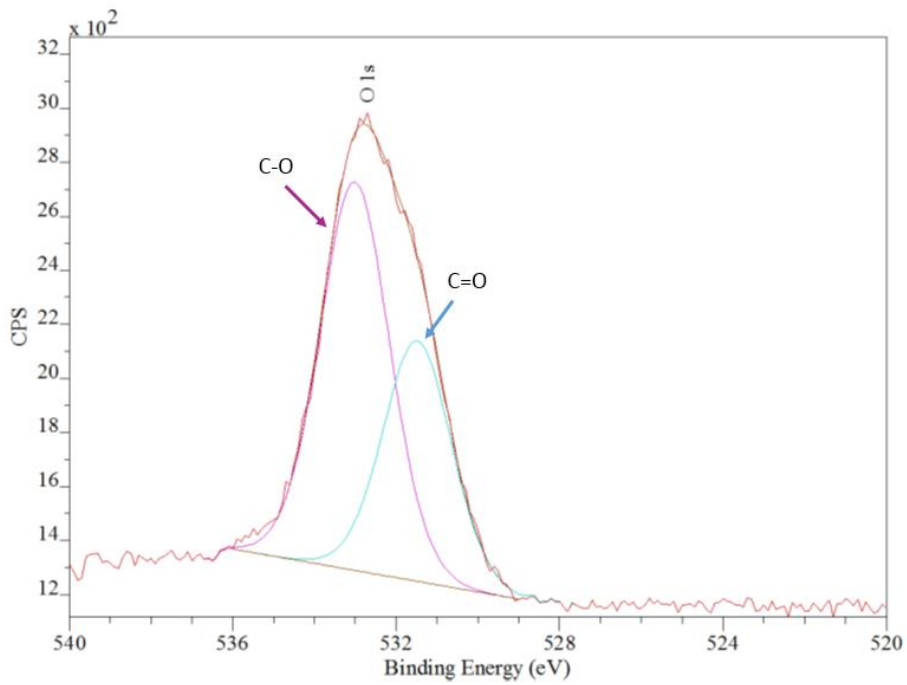


Figure 32. Peak Deconvolution for the O1s Peak (Early SOI Sample)

All other samples followed the same process and their deconvolution plots are given in Appendix B for transparency.

Fitting for the following bondings: C-C, C-O, C=O and O-C=O are commonly used for carbonaceous combustion matter as it is typically composed of aliphatic based C-C bonding, aromatic C-C bonding and various oxygen functional groups most dominantly through carboxylics, carbonyls, alcohols, ethers and phenolic species (Vander Wal, Bryg and Hays 2011), (Lee, et al. 2009).

Values for the respective bonding groups as a percentage of the carbon content and a percentage of the oxygen content are given in Figure 33. To help with the reader interpreting this data, we shall give an example. If the oxygen content was found to be 20 atomic percent during the survey scan and the C=O bonding was 50 atomic percent of the oxygen core scan, then the percentage of C=O bonding from oxygen would be given at 10% in Figure 33, 50% of 20%.

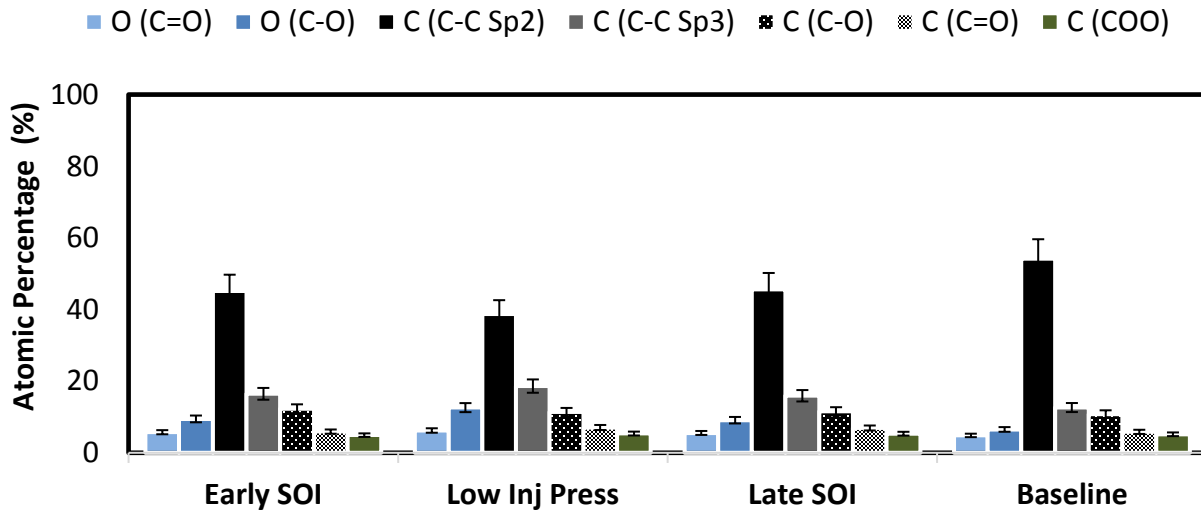


Figure 33. Atomic Percentage of Various Bonding States for both Oxygen and Carbon

Functional groups found within literature for combustion derived carbonaceous matter were found to be ordered in the following way: C=O < C-O < C-C (Cain, et al. 2010) and this trend was observed with the gasoline derived soot in this thesis. The Sp<sup>2</sup> and Sp<sup>3</sup> C-C bondings resolved from the first carbon peak made up over half of the carbon content followed always by C-O, C=O and O-C=O (represented by COO) respectively. This was true for all cases. The Sp<sup>2</sup> and Sp<sup>3</sup> carbon peaks are often discussed in terms of an aromatic and graphitic carbon bonding for the Sp<sup>2</sup> carbon and an aliphatic and amorphous carbon bonding for the Sp<sup>3</sup> carbon. Within literature the nature and cause of the two different peaks is still under investigation but consistently it is defined as a structural effect caused by differences in the soot matrix chemical composition. It has been proposed with supporting work by Raman and TEM imaging that the Sp<sup>2</sup> carbon is related to a crystalline structure and longer fringe lengths within the carbon whereas the disordered regions and shorter fringe lengths were related to Sp<sup>3</sup> carbon (Yang, et al. 2017), (Gaddam and Vander Wal 2013). This carbon hybridization is thought to occur during the surface growth process and soot matrix addition from either an aliphatic or an aromatic component. Previous works have found that nascent soot particles are aromatic in nature and grow in mass through a hydrogen-abstraction-carbon-addition (HACA) process, however aliphatic compounds are often present and integrate themselves within the soot matrix during the particle growth process (Oktem, et al. 2005), contributing to the Sp<sup>3</sup> hybridization.

The amount of Sp<sup>3</sup> hybridized carbon was quite high for the samples. Once again suggesting the soot is quite disordered. It is interesting to note that the ratio of Sp<sup>3</sup>/Sp<sup>2</sup> bonding is similar for all samples, with a slightly higher value for the low injection pressure case and the lowest value for the baseline case. An interesting comparison of these ratios may be made with



the Raman spectra analysis using the D3 peak fit at  $1500\text{ cm}^{-1}$  as it represents  $\text{Sp}^3$  carbon or stretched C-C bonds. Figure 34 provides a comparison of the peak area percent for the  $\text{Sp}^3/\text{Sp}^2$  peaks from both types of analysis,  $A_{\text{D3}}/A_{\text{G}}$  from Raman and the area ratio of  $\text{Sp}^3/\text{Sp}^2$  peaks in the XPS C 1s core scans.

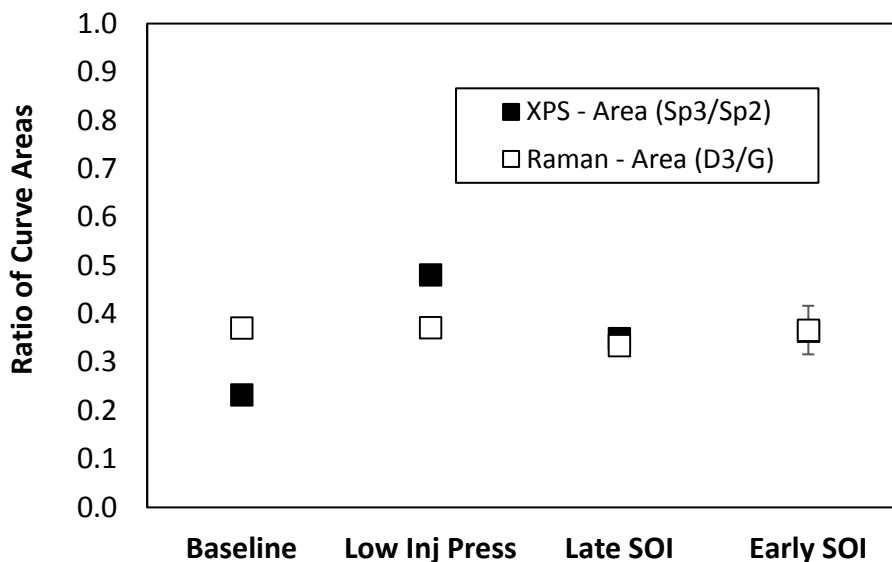


Figure 34. Comparison of  $\text{Sp}^3$  Results from XPS and Raman

Both methods produce results suggesting a similar value, roughly 30% to 45% with a few outliers from the XPS analysis. For the XPS analysis, there is a slight increase in  $\text{Sp}^3$  content for the low injection pressure case and decrease in  $\text{Sp}^3$  content for the baseline case. Whereas for Raman, there was little variation between samples. It is safe to say the values are quite similar and the range presented, 30% to 45%, is likely accurate. Any trends within the data should be taken with caution.

It may also be noted by Figure 35 that there is no relationship between surface area (particle size) and the  $\text{Sp}^3/\text{Sp}^2$  ratio. This work is not alone in suggesting a lack of dependence on

particle size for  $Sp^3/Sp^2$  ratio despite this hybridization occurring during the soot formation process (Cain, et al. 2010). However, this is the first work to analyze the size dependence effect for the combustion process within a gasoline engine. The lack of dependence on size or surface area suggests that though some conditions may promote large and rapid particle growth, such as early injection timing, this does not relate to an enhanced aliphatic content within the soot matrix as no moderate differences in the  $Sp^3$  content was observed.

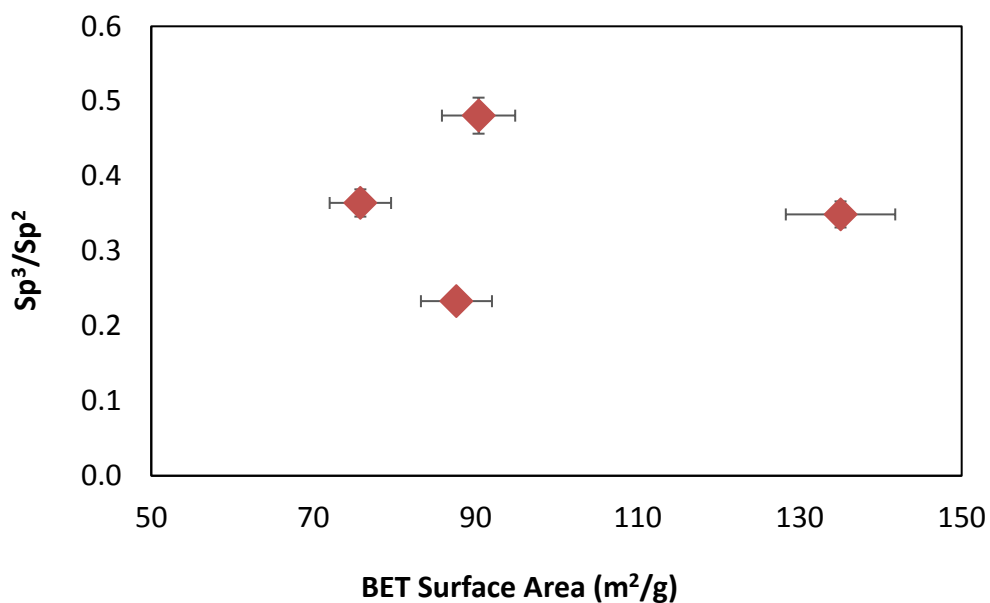


Figure 35. Comparison of  $Sp^3/Sp^2$  with the BET Surface Area (m<sup>2</sup>/g)

As the  $Sp^3/Sp^2$  ratio should relate to differences in nanostructure, it may also relate to the oxygen content as more disordered soot was proposed to possess higher levels of surface functional groups and oxygen bonding. Interestingly enough, as shown in Figure 36, there is some correlation to the  $Sp^3/Sp^2$  ratio and oxygen content, with an increase in  $Sp^3/Sp^2$  ratio following increases in the oxygen percentage for the PM samples. Though it should be mentioned again that no differences in nanostructure was found through Raman analysis of the

D1/G peaks or through visual inspection of TEM images for ordered graphene segments, suggesting that little difference in nanostructure may actually exist.

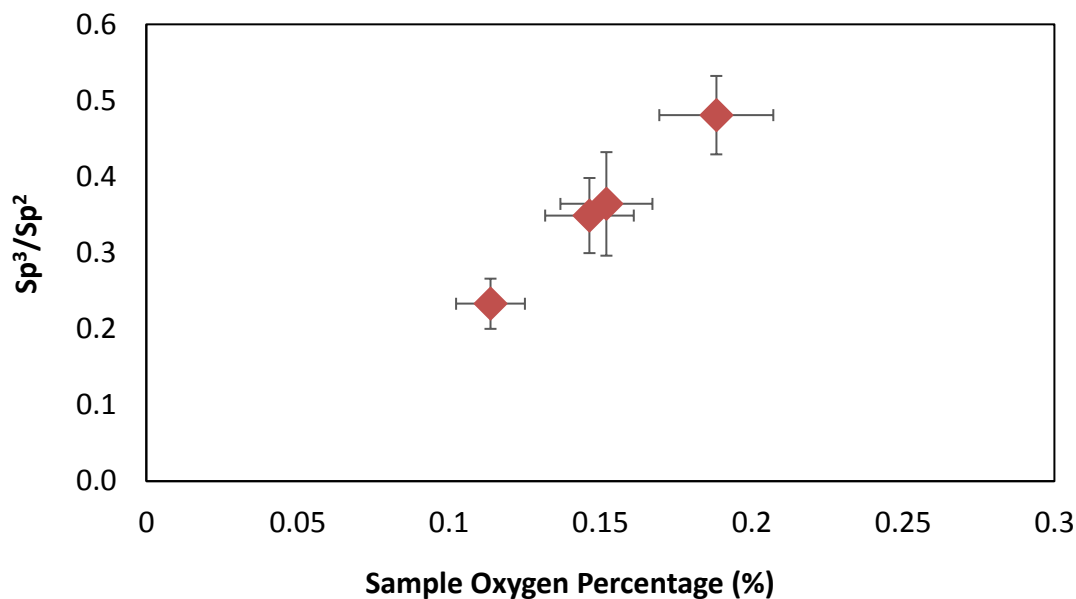


Figure 36. Comparison of  $Sp^3/Sp^2$  ratios to Sample Oxygen Percentage for the Four Operating Conditions

Other researchers have reviewed the  $Sp^3/Sp^2$  ratio observed for gasoline soot from differing operating conditions. This variation was found to be dependent on fuel/air mixing within the combustion chamber (Gaddam and Vander Wal 2013) and possibly caused by higher rates of volatile organic carbons adsorbed during soot formation (Lee, et al. 2013). Fuel rich conditions and conditions with poor mixing, late injection of fuel, led to significant  $Sp^3$  carbon and matrix bound organics. As the baseline case held the lowest  $Sp^3/Sp^2$  ratio from the XPS analysis, and the highest fuel/air mixing potential, it seems that the effect of fuel/air mixing is likely a cause of the observed differences. Though it should be stated again that values found in

this work overall are quite close and any trends should be taken as a suggestion and point of discussion.

$Sp^3/Sp^2$  ratio does not correlate in any way with reactivity as would be expected, as shown in Figure 37 by a comparison of  $Sp^3/Sp^2$  ratio to  $t_{10-90}$ . The increasing initial  $Sp^3/Sp^2$  ratio surprisingly trends with a decrease in reactivity. This finding indicates that if the slight differences in the relative ratios of aromatic graphitic to aliphatic amorphous carbon were true between the four conditions as suggested by differences in the  $Sp^3/Sp^2$  peaks, any influence from this is not significant enough to overcome the influence of some other factor that must be contributing to the observed changes to reactivity.

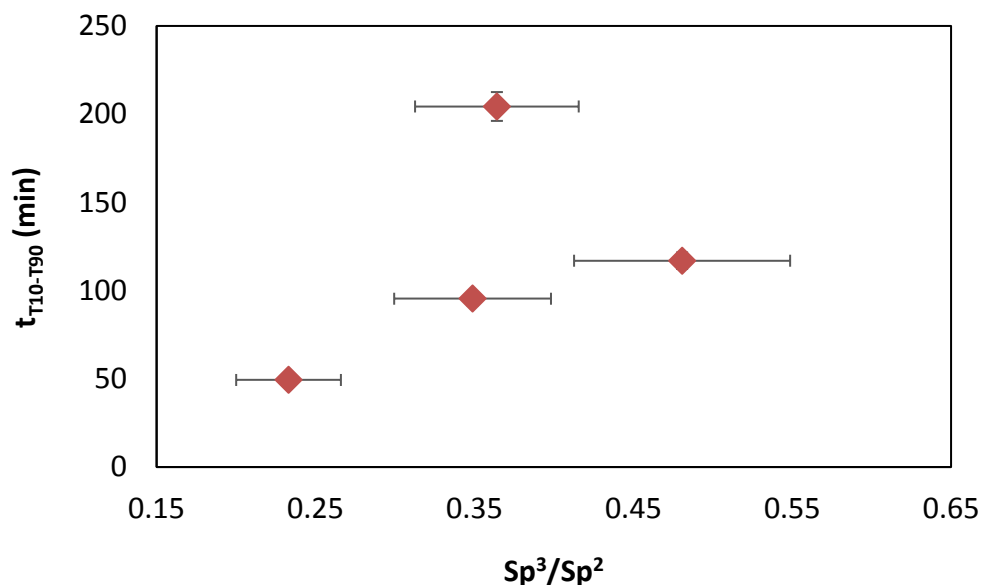


Figure 37. Comparison of Reactivity ( $T_{10-T90}$  time for 500C oxidation) to the  $Sp^3/Sp^2$  ratio

From reviewing again Figure 33, it can be observed that despite differences in the  $Sp^3/Sp^2$  bonding, the relative ratios of various carbon oxygen bonding (C-O, C=O and O-C=O)

were found to be quite similar amongst the four sample. Oxidation often proceeds through the formation of various oxygen functional groups including alcohols, aldehydes and carboxylic acids, and the presence of these groups often corresponds to different degrees of oxidation of the carbon. Given that these are all immature highly disordered soot particles that likely experience a relatively low formation temperature, it is expected their absolute concentrations of various oxygen functional groups would be so similar. Given the noted differences in  $Sp^3/Sp^2$  bonding and the lack of noted differences between the oxygen bonding, there is little relationship to be defined regarding the hybridization state and the presence of specific surface functional groups. This is not the first work to observe that patterns may not emerge between the carbon hybridization state and the surface functional groups of combustion derived carbon samples (Vander Wal, Bryg and Hays 2011).

## **5.7 Ash**

Ash refers to any non-combustible contribution to soot particles. Typically, ash is comprised of engine wear materials (Fe, Al or Si), lubrication additives (Ca, P, Na, Zn, B, Mo, etc) and any material from an upstream catalyst (Pt, Pd, Rh) (Lambert, et al. 2016). Some of these elements, such as calcium, zinc and sodium, have been found to act as a catalyst and enhance oxidation when in close contact with the soot, whereas compounds containing phosphorus have been known to inhibit oxidation, possibly through coating the soot particle and forming a physical barrier to the oxygen (Neeft, Makkee and Moulijn 1996), (McKee, Spiro and Lamby 1984). Inductively coupled plasma mass spectroscopy (ICP-MS) was used to determine the additive package in the oil and x-ray photoelectron spectroscopy (XPS) and scanning

transmission electron microscopy with energy dispersive spectroscopy (STEM-EDS) were utilized to detect the presence of ash within the soot particles.

### 5.7.1 ICP-MS

ICP-MS analysis was completed to identify the concentration of various oil additives. The results are shown in Figure 38 with error bars referencing variability in repeatability. The results from the ICP-MS analysis confirm that the engine oil used for this work, Mobil 1 5W-30 Full Synthetic High Mileage, contains decent amounts of magnesium, zinc, calcium and phosphorous. As calcium is the primary driver for enhanced oxidation of soot, it is important to know that it is present in the oil. This elemental data also guides what species to look for in the XPS and STEM+EDS analysis.

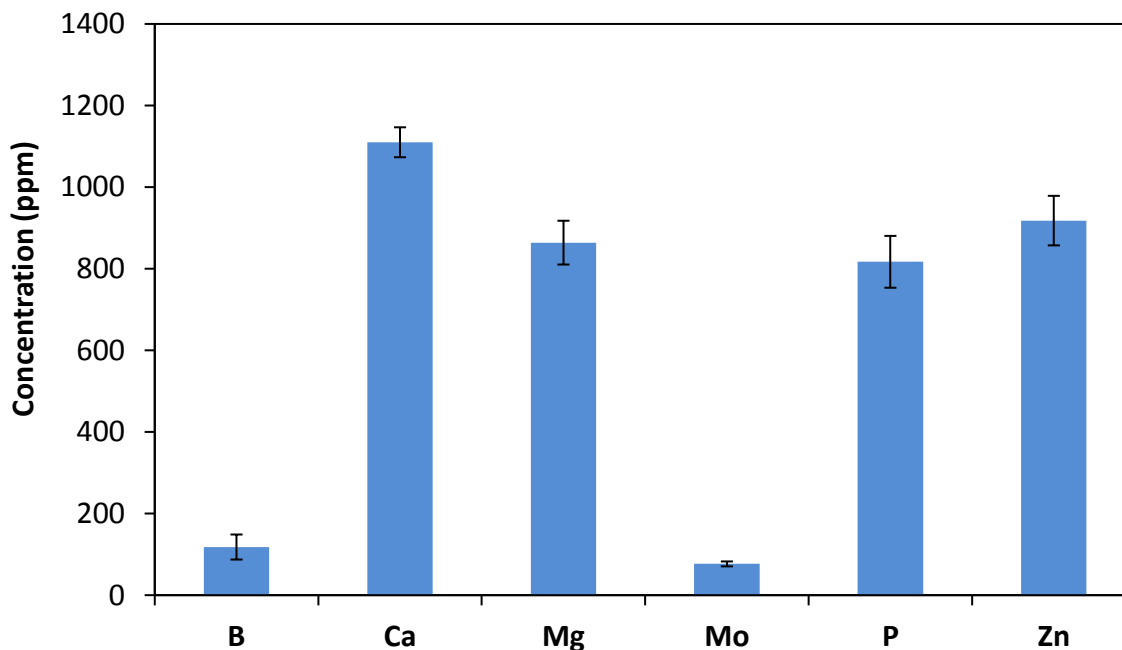


Figure 38. Concentration of Various Elements from a Sample of the Engine Oil

The formulation seems typical for a gasoline four-cylinder application given the decently high levels of calcium, magnesium, phosphorus and zinc and the presence of some boron and molybdenum (Choi and Seong 2016).

As previously mentioned, calcium enhances soot oxidation while high levels of ZDDP packages, containing phosphorus, tends to inhibit soot oxidation. Determining the effect of both ZDDP and calcium when combined in the lubrication oil has been performed by other works (Choi and Seong 2016). Given these findings, it is assumed that the calcium effect would still dominate, leading to enhanced soot oxidation when compared to the soot produced without additives in the oil, despite any opposing effect from the phosphorus. It should be mentioned that zinc has been found to be a mild soot enhancer (Neeft, Makkee and Moulijn 1996), (Neeft, Makkee and Moulijn 1996), though it was hard to determine its effect in the work mentioned as there is more phosphorous than zinc by an atomic percentage in the ZDDP package and the two elements were not separated in the study. Nevertheless, it seems any ash present in the soot particles would enhance soot oxidation given the additives contained in the oil used for this work.

### **5.7.2 XPS**

XPS analysis through a survey scan was performed on the four samples taken from the different engine operating conditions. No elements other than carbon, nitrogen and indium were detected using XPS. The detected indium comes from the background material used to hold the soot samples for analysis. The XPS technique is a surface technique, with a sample depth from 3nm to 10nm. It is also a low-resolution technique, with a detection limit typically near 1%.

Therefore, it may not be able to provide information regarding small ash particles contained within soot particles or if ash particles are small in number relative to the soot particles.

### **5.7.3 Carbonaceous Soot Concentrations**

One trend becomes apparent when considering the engine out soot concentrations from the four different operating conditions. To discuss this a plot of soot reactivity,  $t_{10-T90}$ , versus engine out soot values as measured by the AVL smoke meter is given in Figure 39. In reviewing this plot it seems there is a clear trend with soot reactivity and engine out soot levels, with reactivity decreasing as the engine-out soot level rises. This trend may be due to difference in the levels of ash content within the soot. Supposing oil consumption is relatively constant given the operating conditions explored in this work are at the same speed and load, any increase in soot emissions would mean less ash for a given amount of collected soot as the higher levels of soot dilute the constant ash concentration. Given this, we may go on to assume the higher the engine out soot level, the lower the reactivity of the soot should be as there is less relative ash. From Figure 39 it appears this may be the case even when ash levels are assumed quite low and undetectable with XPS.



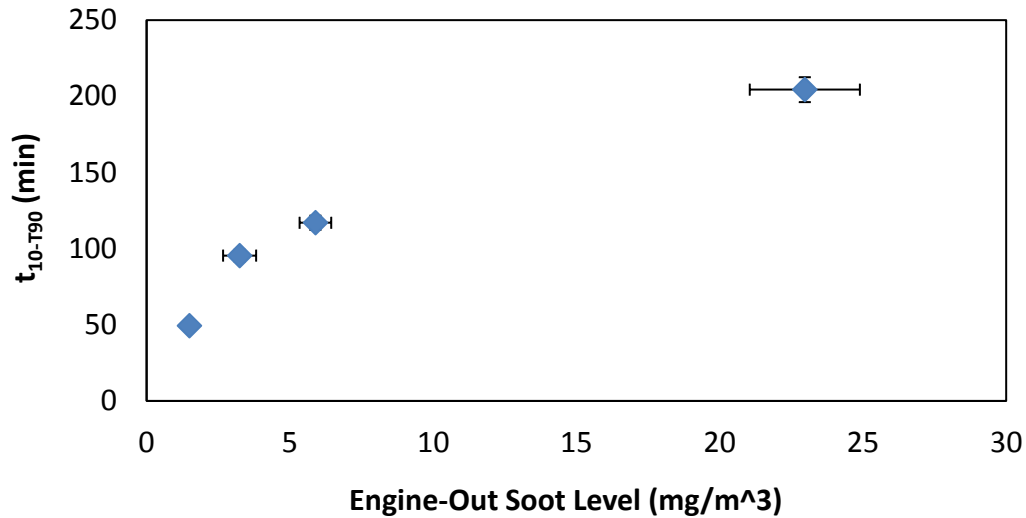


Figure 39. Soot Oxidation Time,  $t_{10-90}$ , Plotted against Engine-Out Soot Levels as Measured by the AVL Filter Smoke Meter

Previous researchers analyzing the reactivity of gasoline soot have proven that ash fraction can correlate well with engine-out soot values for hot steady-state operation, so this assumption is not much of a stretch. In their work, it was also determined that these changes in ash content did have appreciable impact to the reactivity of the soot (Choi and Seong 2015).

#### 5.7.4 STEM-EDS

STEM-EDS was performed for the baseline and early injection timing conditions respectively. These two conditions were chosen as they have the greatest difference in reactivity and therefore should prove to have the most visible trend if the theory regarding the relationship between engine out soot values and ash content is true for the four different operating conditions. STEM-EDS has quite a few advantages over XPS, and if the ash is present, this technique should be able to detect it. This technique was determined, through Monte Carlo simulations with

Casino, to collect information on elements present from the entire depth of the sample and has a detection limit near 0.1%. This is unlike the XPS by which only the surface, 3nm to 10nm in depth, is analyzed and for which the detection limit is near 1%. Ash was detected with STEM by comparing dark field and bright field digital images. For areas of interest, EDS spectra were collected.

For the baseline operating condition, multiple areas were viewed while examining hundreds of particles and only one instance of ash was detected. This low rate of ash detection matches other works by which ash concentration in gasoline soots at similar conditions varied from 0.1% to 0.6% (Choi and Seong 2015). The results from this portion of the soot are shown in Figure 40.

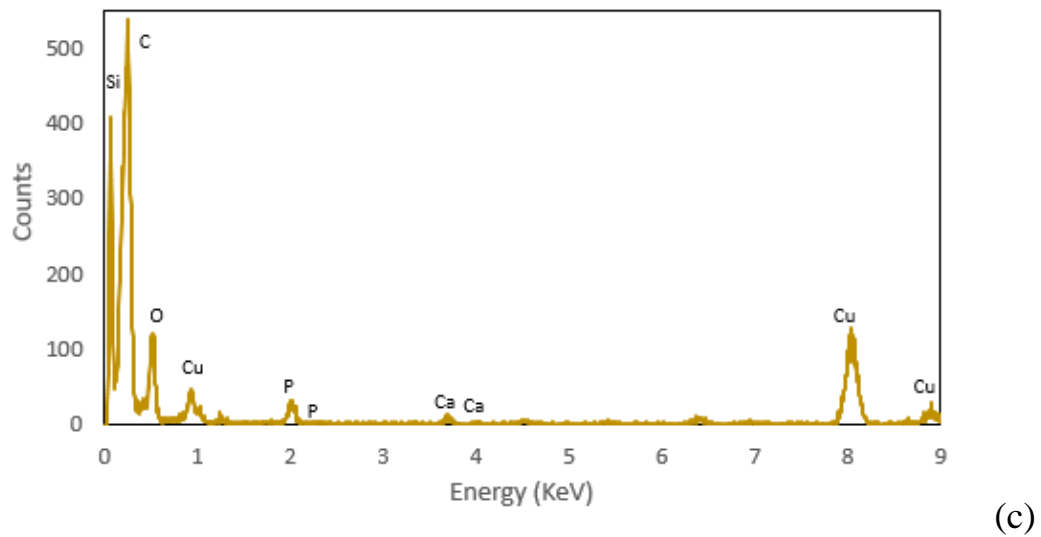
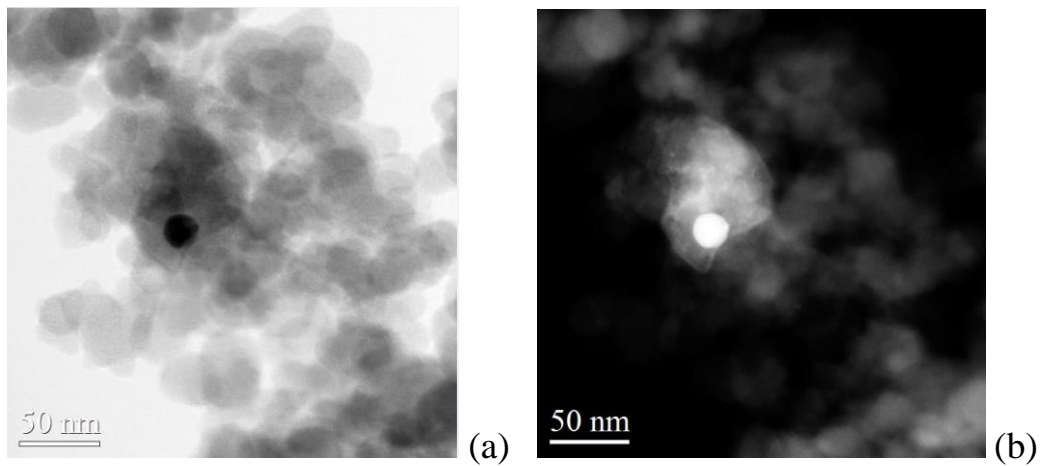


Figure 40. STEM+EDS Results Baseline: (a) Bright Field Image, (b) Dark Field Image, (c) EDS Spectra

This appears to be a cluster of ash particles embedded into the soot alongside a single metal particle. Both calcium and phosphorous are detected in the EDS spectra. Elemental mapping was performed for this area and the results are shown in Figure 41. The range of area covered by the ash particles is nearly 50nm by 70nm.

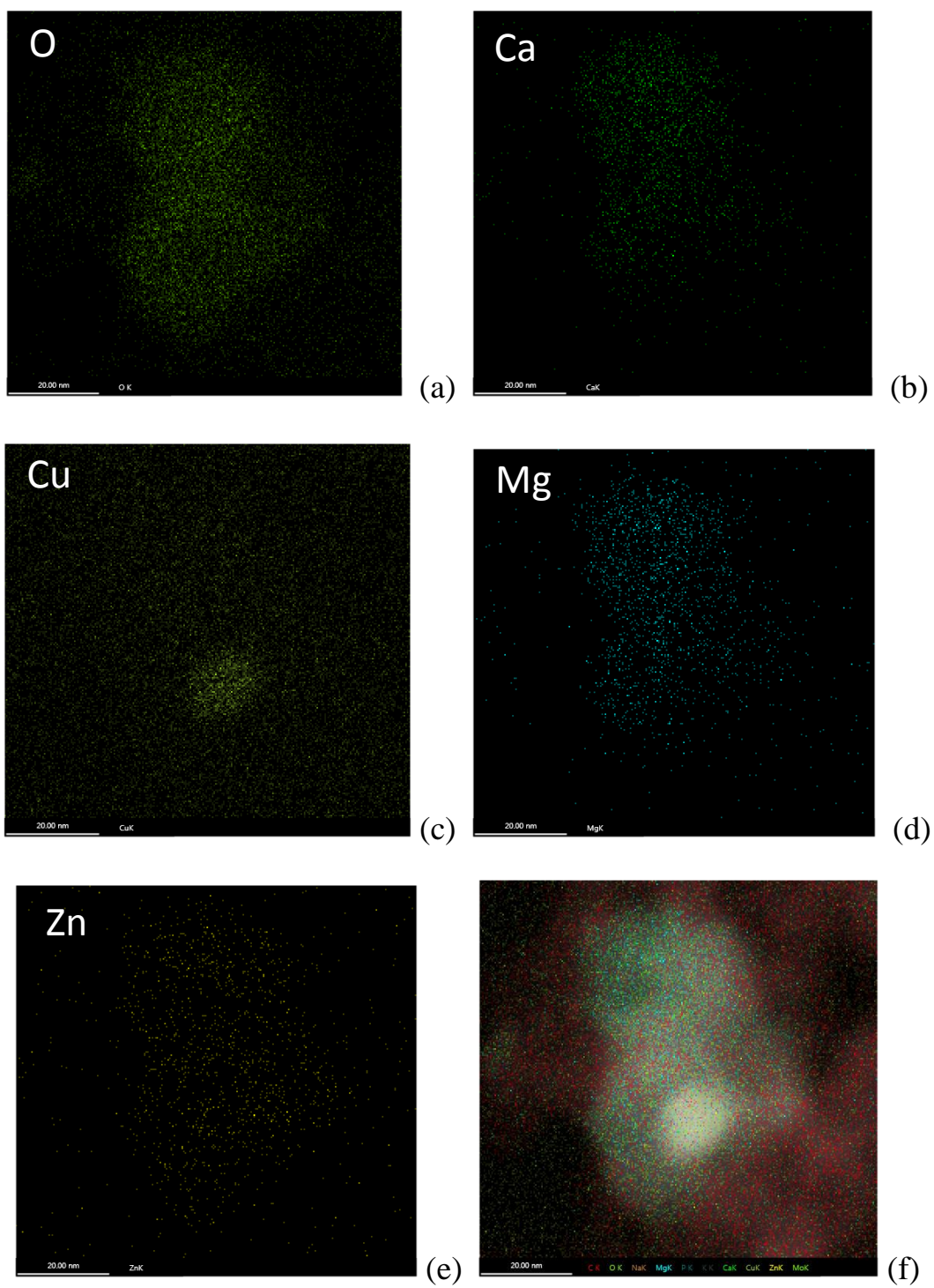


Figure 41. STEM+EDS Elemental Mapping of Baseline Sample: (a) O, (b) Ca, (c) Cu, (d) Mg, (e) Zn, (f) Overlay

Previous researchers have reviewed ash and soot particle interactions using soot produced from diesel engines. Within these works, lubricant and engine wear derived ash particles were emitted as small particles typically between 10 nm and 30nm. The particles were present both as free particles and bound to soot particles of all sizes (Mayer, et al. 2010). The interaction of the soot and ash have received mixed answers in literatures. Some works have suggested ash would be present in many of the individual particles as small embedded ash particles within the soot (Choi and Seong 2015), while others have found localized areas high in ash content (Sappok and Wong 2007).

In reviewing Figure 41, it appears that the single distinct particle is copper. The single copper particle may likely have originated from bearing wear that made its way to the lubrication oil and then entered the combustion chamber. Previous researchers have also postulated that engine wear metals, mostly iron, nickel, aluminum and copper, start as larger micron size particles, but they enter the engine oil and undergo a nucleation process during combustion (Israel n.d.). Contributions from the additives within the lubrication oil are clear. Within our soot sample various additives, calcium, magnesium and zinc, were spread uniformly throughout the ash filled region. Again, this ash filled region is rare as most of the soot particles contained no trace of ash. It may be assumed that the majority of particles contain no ash and a few clusters of soot particles contain many ash particles evenly distributed through a densely ash populated area.

When analyzing the early start of injection condition, no ash was detected within the regions of the soot sample analyzed. The analysis of the soot included hundreds of particles. For any region that looked like it might contain ash, EDS spectra were collected. An example of the

bright field and dark field comparison and an EDS spectra from the early start of injection condition are given in Figure 42.

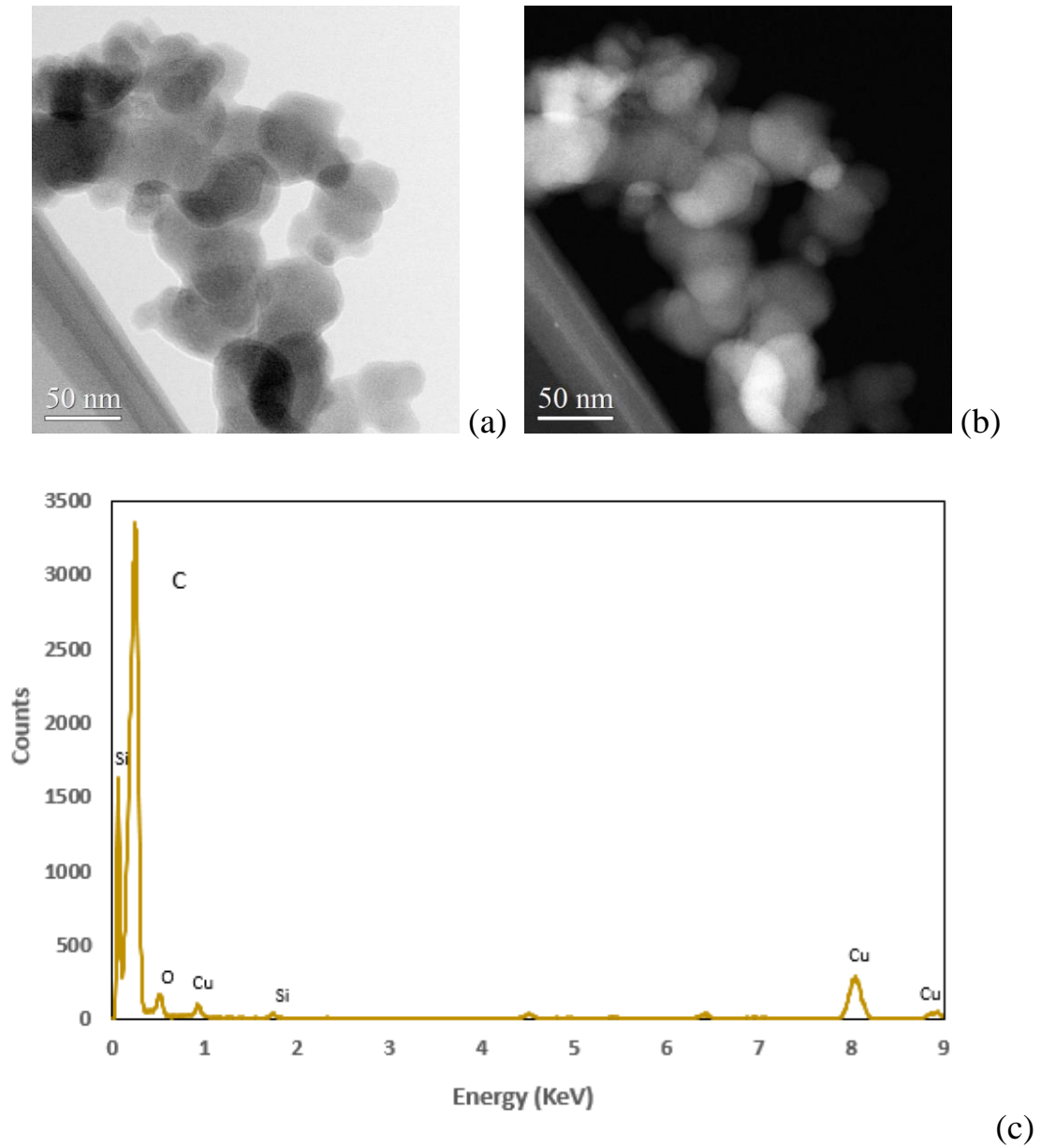


Figure 42. STEM+EDS Results Early SOI Condition: (a) Bright Field Image, (b) Dark Field Image, (c) EDS Spectra

From Figure 42 it is observed that no ash particles are detected from the soot sample area under analysis as there are no contrasting bright/dark spots, only bright/dark spots corresponding to high soot particle overlap. In addition, the EDS spectra shows no peaks other than carbon, oxygen, silicon and copper. Copper is most likely from the copper grid holding the sample and the silicon was oddly present in all samples and may be an artifact of seal materials, dirt that made its way to the intake of the engine or an artifact of the silicon detector used in the EDS. No silicon was observed in the ICP-MS analysis of the oil sample. It shall be mentioned again that peak determination included a three-sigma separation using the background signal and the presence of both an alpha and beta peak.

In addition to enhancing oxidation rate, findings from work evaluating oil dosed fuel have found that light off temperatures were reduced significantly with the presence of ash within the soot (Jung, Kittleson and Zachariah 2003). This aligns with our findings from the temperature ramp with the TGA. In reference to the model soot, light off temperatures were reduced for all conditions except the early start of injection, for which no ash was detected.

These findings with STEM+EDS do not confirm that no ash is present in the soot produced from the early injection timing condition. As oil was likely burned at an equal rate for this condition, it would seem unlikely that no ash is present in any of the bulk sample. It is likely, however, that this level of ash is extremely low. It is also interesting to note that much of this soot was formed on the piston top, not in a region such as the cylinder walls where interaction with the lubrication material would be likely.

## 5.8 Summary

Various properties of the particulate matter samples relating to reactivity were evaluated. Nanostructure was similar and highly disordered for all samples. Surface area was dependent on primary particle size and varied greatly but was not correlated to reactivity. The volatile organic fraction and the surface functional groups were similar between the four samples. Ash content was identified as being the most likely contributor to variations in reactivity.

Ash content could not be detected using XPS, as the detection limit and depth of the technique may both be too low. However, using STEM+EDS, ash content was determined for the most reactive condition and was not detected for the least reactive condition. Ash particles appear in embedded clusters within certain soot areas, leaving most soot particles without ash.



## **Chapter 6. Partial Oxidation Results**

The TGA was utilized to partially oxidize soot from the early start of injection and baseline operating condition, the least and most reactive conditions respectively, to an oxidized state of 40% mass loss and 75% mass loss.

### **6.1 Particle Characteristics during Oxidation**

An evolution in particle size, particle interactions and nanostructure is expected to take place during the oxidation process. TEM imaging and XPS analysis of carbon and oxygen bonding were used to review these evolutions for the gasoline soot produced for this work.

#### **6.1.1 Nanostructure and Particle Interactions**

TEM images were taken for the two operating conditions to evaluate changes to primary particle size, particle to particle interactions and to evaluate any changes to particle nanostructure. Results from images taken at magnification rates ranging from 65k to 80k are given in Figure 43.

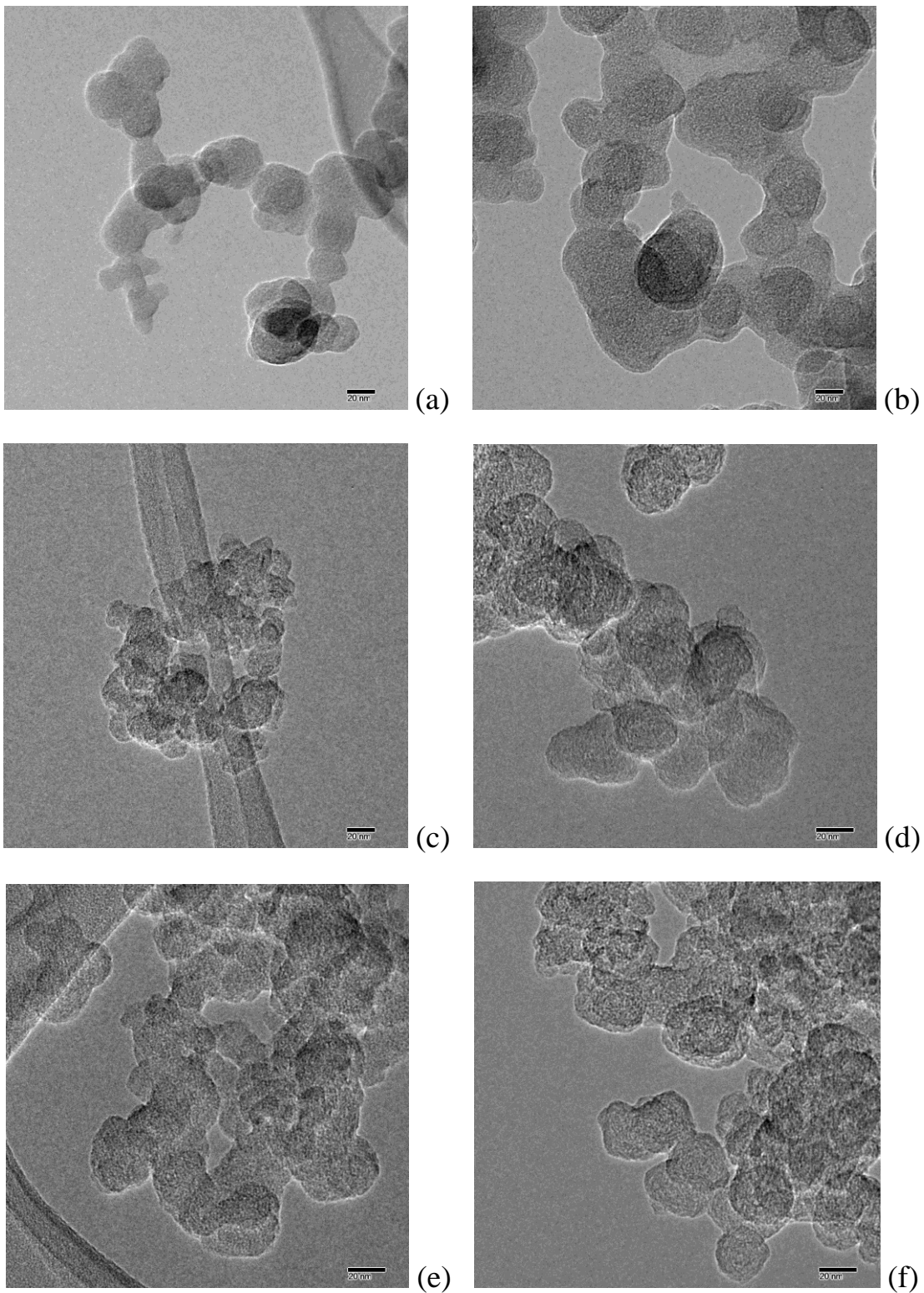


*Figure 43. TEM Images Taken of the Soot Oxidation Process: (a) Baseline 0% - 65k, (b) Early SOI 0% - 65k, (c) Baseline 40% - 65k, (d) Early SOI 40% - 80k, (e) Baseline 75% - 80k, (f) Early SOI 75% - 80k*

The soot particles at the 0% oxidation case are branched with independent particles and little particle overlap. Upon oxidation of the soot, many of the particles exhibit agglomeration identified by high particle overlap and compact aggregate particles. Interestingly, after reviewing the baseline case at the 75% oxidation level, it was determined the primary particle size had actually grown as the particles had merged into larger highly non-spherical particles. It is difficult to determine the exact outline of a specific primary particle. In fact, during the partial oxidation events the remaining soot in the TGA crucible formed a pellet capable of free standing. The initial soot placed in the crucible was a very loose powder. An image of this pellet from the crucible is given in Figure 44.

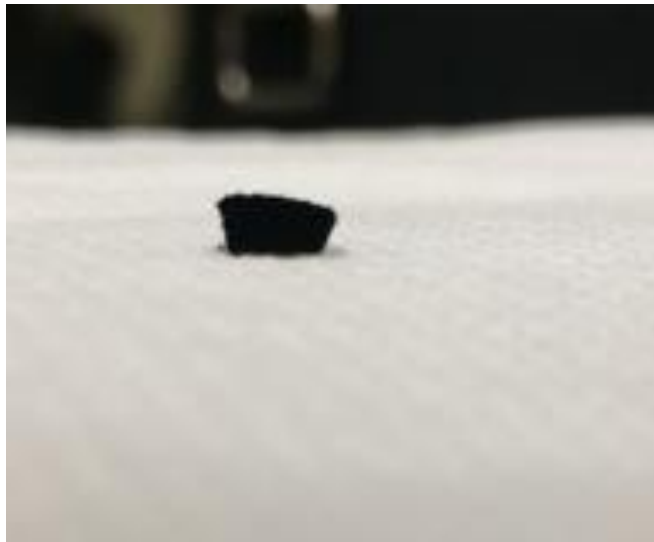


*Figure 44. Pellet of Early SOI 40% Oxidized Soot from TGA Crucible*

This agglomeration of soot may be explained by the high “attractive interaction forces” between soot particles uncovered by other researchers using atomic force microscopy (Kamp, et al. 2014). It was found that soot-soot attraction exhibited the highest attraction force of all

potential interactions (soot-soot, soot-ash, soot-DPF, ash-ash and ash-DPF). Additionally, researchers from this same group installed a high-resolution stereo microscope to view soot oxidation events within the single channel of a DPF (Sappok, Govani, et al. 2013). During the oxidation process, the soot cake was observed to crack as “soot islands” formed. As oxidation continued, these soot islands appeared to slide across the DPF surface and shrink inward as they were compelled by the strong attractive surfaces within the soot. This is consistent with the previous TEM images in our work that suggest the gasoline soot particles are migrating and combining with each other to form non-spherical large particles with high particle overlap.

The nanostructure is also of interest when reviewing the soot oxidation process. Rearrangement of the soot nanostructure during oxidation and the oxidation pathway taken within the particle have an impact on soot oxidation rates and understanding this process may provide access to understanding the factor contributing to differences in reactivity. Some researchers have observed soot particles that are oxidized from the outside in, shrinking core, (T. Ishiguro, et al. 1991) while others have observed soot particles that are oxidized from the inside out, hollowing out (J. Song, et al. 2006). The evolution in nanostructure during oxidation is also not consistent among soot samples. In some works, the nanostructure became more ordered during the soot oxidation process as the more amorphous and likewise more reactive carbon oxidized preferentially while the longer graphene segments actually exhibited growth and loss of curvature (Strzelec, et al. 2017), (J. Song, et al. 2006), (Ishiguro, Suzuki and Fujitani 1991), (Gaddam, Vander Wal and Chen, et al. 2015). This phenomenon was typically seen to occur most strongly with biodiesel-based soot. It was postulated from other works that oxidation might remove interstitial carbon thereby disengaging cross-links between lamella and activating edge

sites for what was termed “vegetative growth” into longer and straighter lamella (Vander Wal, Yezerets and Currier 2007). While for other soot particles, such as soot produced from a neat Fischer-Tropsch diesel, the nanostructure became slightly more disordered during oxidation (J. Song, et al. 2006). The differences in the nanostructure evolution during oxidation may be due to the presence of surface functional groups and organic volatiles. High levels of functional groups may lead to re-arrangement of graphene segments allowing oxygen access to inner portions of the soot particle and high organic fractions may enhance porosity within the soot as they are removed easily during high temperatures. Access of oxygen to the inner soot layers allows for the interstitial carbon removal required for the formation of long graphene segments and allows oxidation of internal short disordered graphene segments to occur before the outer layers of the soot particles are removed (J. Song, et al. 2006).

For this work, the nanostructure of the gasoline soot particles formed at the baseline operating condition and at the early start of injection condition appeared to become more disordered during oxidation and showed no signs of internal burning. TEM images are shown for the 0%, 40% and 75% oxidation states in Figure 45.

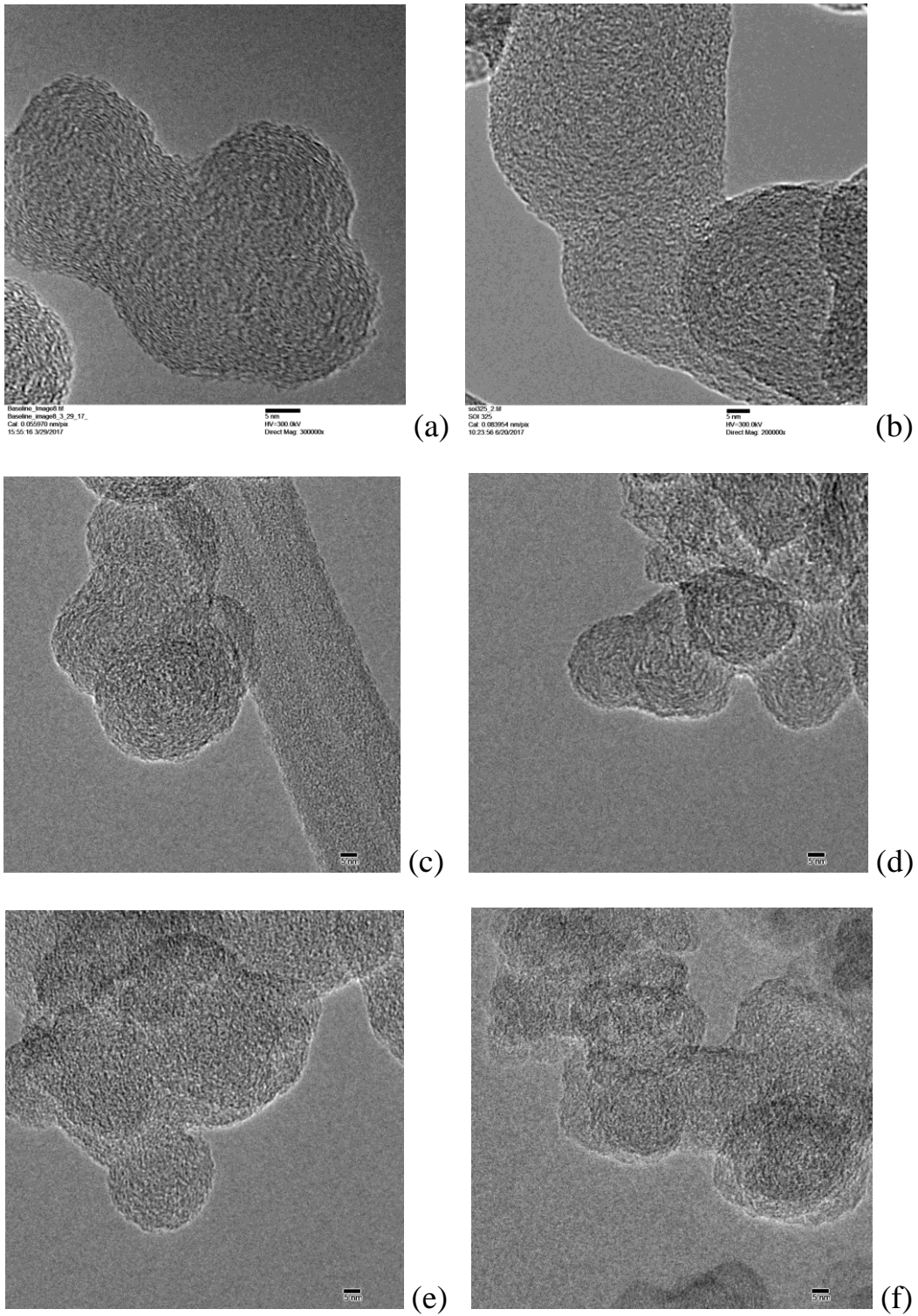


*Figure 45. TEM Images Taken at a Magnification at 300k of the Soot Oxidation Process: (a) Baseline 0% - 300k, (b) Early SOI 0% - 200k, (c) Baseline 40% - 160k, (d) Early SOI 40% - 160k, (e) Baseline 75% - 160k, (f) Early SOI 75% - 160k*

Though some graphene segments of length were present on the outer edges of the soot particles that had not been oxidized, the oxidized soot samples show a highly amorphous nature with no presence of any graphene segments of notable length. The soot is highly disordered and remains disordered throughout the oxidation process. Perhaps there is little re-arrangement in the soot layers and the soot is being oxidized from the outer, possibly a bit more graphitic layer, into the inner more amorphous layers of the nascent gasoline soot particles. It is also evident that the particles are merging into each other, suggesting that perhaps when this outer region is removed, cohesive forces and the highly amorphous nature of the soot with its highly disordered short graphene segments may result in easy melding between particles.

### **6.1.2 Chemical Composition**

The enhanced disorder during soot oxidation for the baseline and early start of injection conditions viewed qualitatively through the TEM images was confirmed through XPS analysis of the partially oxidized samples and core scans taken over the C1s peak to resolve the  $Sp^2$  and  $Sp^3$  bonding. The  $Sp^2$  peak represents an aromatic and graphitic carbon bonding while the  $Sp^3$  peak represents an aliphatic and amorphous carbon bonding. The results are given in Figure 46.

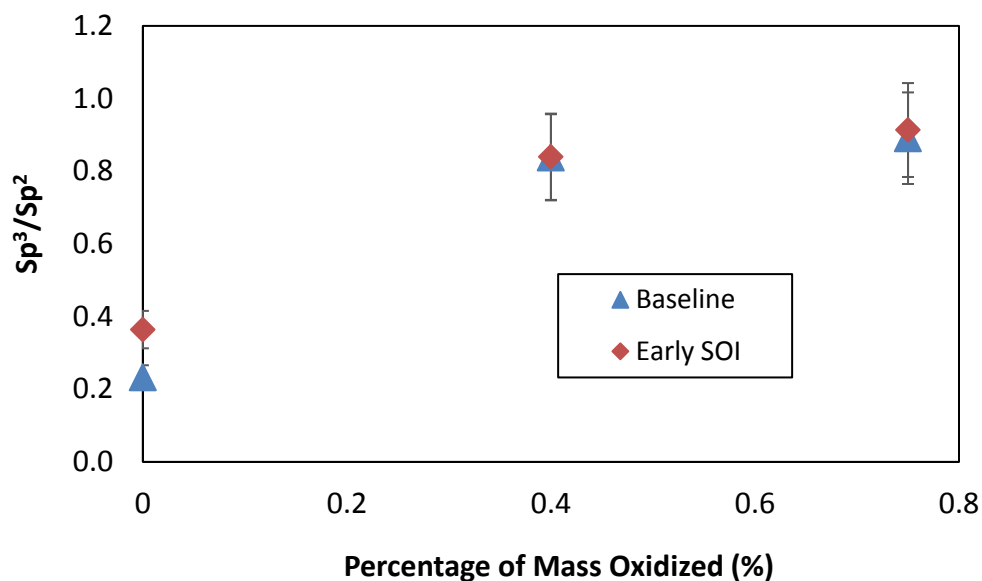
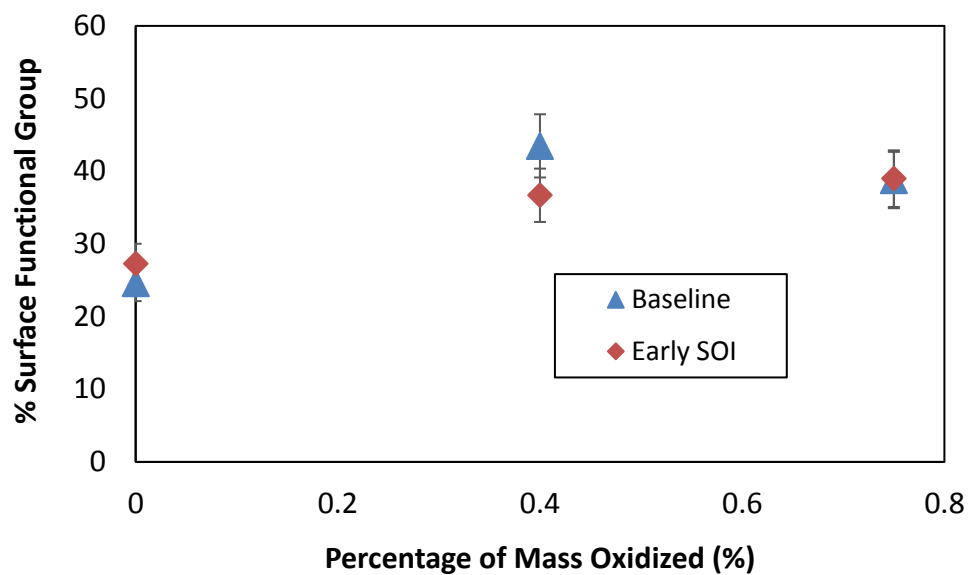


Figure 46.  $Sp^3/Sp^2$  Ratio during Soot Oxidation for the Baseline and Early Start of Injection Condition

There is an increase in the  $Sp^3/Sp^2$  ratio of carbon bonding even when considering the measurement error. This confirms the TEM results suggesting that the internal structure of the gasoline particles may be more disordered and that the soot particles appear more amorphous during the oxidation process.

Oxidation often occurs through the formation of various oxygen functional groups including alcohols, aldehydes and carboxylic acids. Therefore, the presence of these groups often corresponds to different degrees of oxidation of the carbon. This was confirmed through evaluation of the fraction of oxygen containing surface functional groups to total bonds given by deconvolution of XPS C 1s core scans. The results are shown in Figure 47.





*Figure 47. Surface Functional Groups present for the Baseline and Early SOI Condition during Oxidation*

The content of oxygen containing surface functional groups seems to grow, even when considering experimental error. This would align with the suggestion these groups are involved with oxidation. However, it may be that these groups are present within the soot matrix even prior to combustion. Other researchers have found matrix bound organics present within GDI soot (Gaddam and Vander Wal 2013). This follows the concept that these particles are burning from the outside in, and the inner portion of the particles are highly amorphous and possess higher fractions of surface functional groups.

## 6.2 Ash Content

Ash content was examined again using XPS survey scans for the partially oxidized sample, with the hope that a higher ash-soot ratio may result in detection of ash elements. This

was followed by detection of ash and elemental mapping to determine soot-ash interactions through STEM+EDS.

### **6.2.1 XPS**

Partially oxidized soot samples from the baseline and early start of injection event at oxidation levels of 40% and 75% were analyzed using XPS. As was found in the non-oxidized soot, no elements other than carbon, oxygen and indium were detected. The detection limit is 1% and the depth of analysis is between 3nm and 10nm, thus suggesting the ash quantity near the surface and the relative amounts of ash relative to soot are still too low for detection with this technique.

### **6.2.2 STEM+EDS**

The presence of ash was determined for the baseline and early start of injection soot at a 75% oxidation level using STEM+EDS. Various areas of the TEM grid with particles present were analyzed by comparing bright field and dark field images for the presence of metal elements. Any metal element could be identified as a dark spot on the bright field image and a corresponding bright spot on the dark field image. An EDS spectra was obtained for any area of interest. When reviewing the 75% oxidized baseline soot, it was easy to spot areas containing ash. An example of the bright and dark field images and EDS spectra for the baseline case containing ash is given in Figure 48.

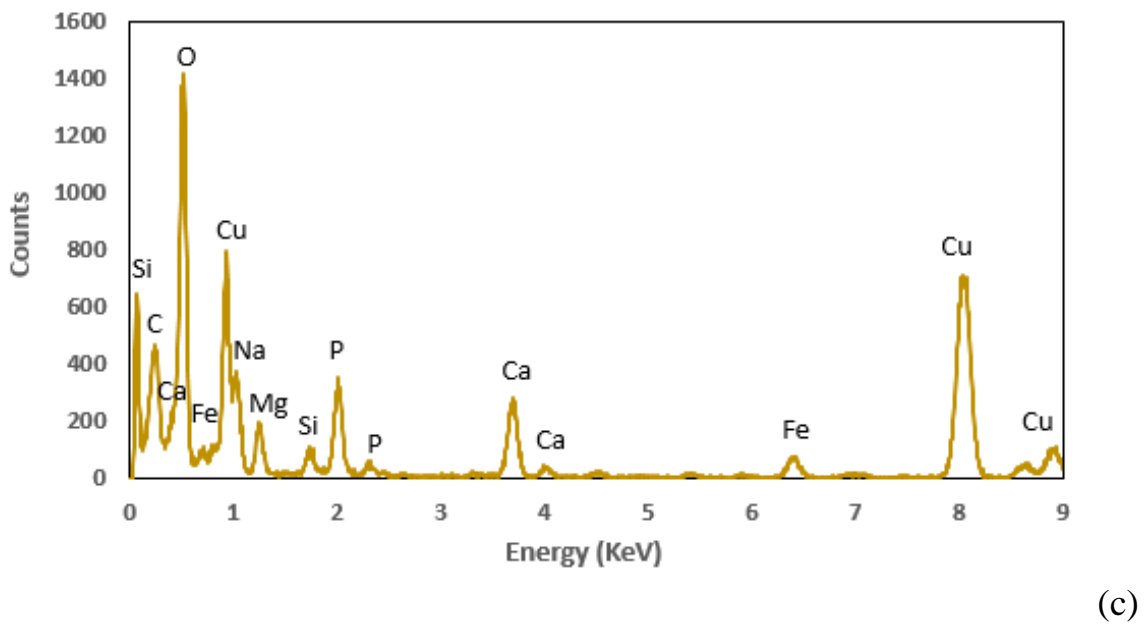
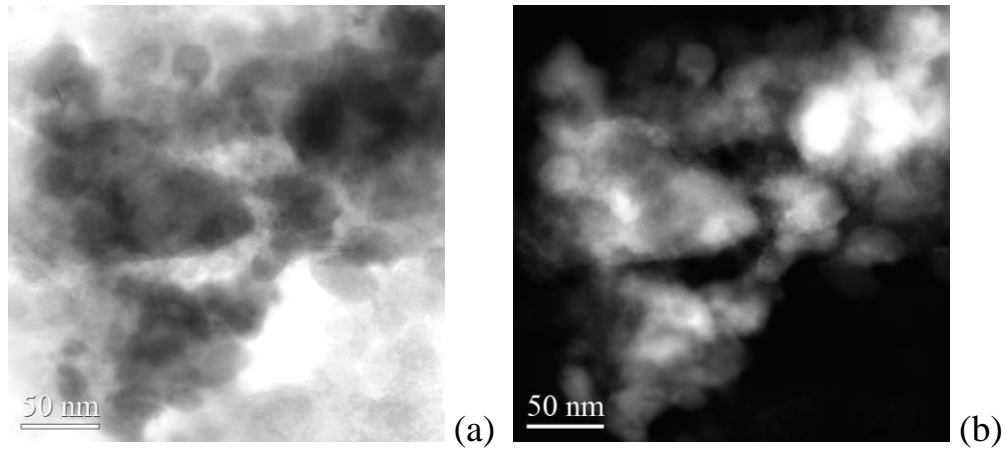
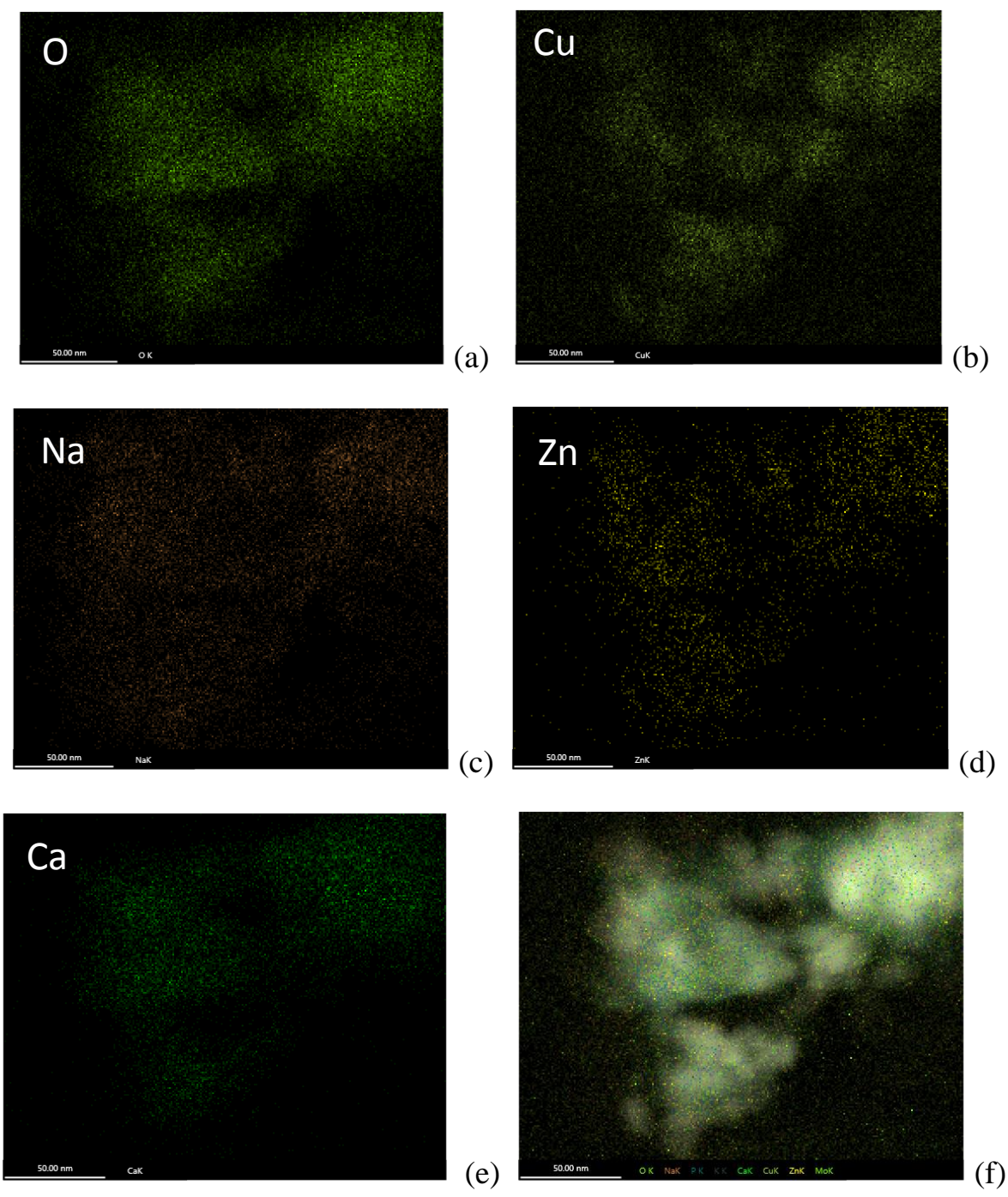


Figure 48. STEM+EDS Results Baseline Condition 75% Oxidized: (a) Bright Field Image, (b) Dark Field Image, (c) EDS Spectra

There appears to be a growth in regions containing ash as the ash containing particles move closer to each other. This aligns with other researchers who have discovered ash particle growth in diesel particulate filters during the soot oxidation event. As the loose soot, containing ash particles, shrink into more dense structures, the ash particles begin to combine and adhere to

each other (Sappok, Govani, et al. 2013). This adhesion makes sense as ash particles have a higher attractive force for fellow ash particles over fellow soot particles (Kamp, et al. 2014). It should also be noted that there is still high soot to ash contact and the ash regions are still separated by soot particles, thus suggesting the ash is still playing a strong role in enhancing soot oxidation. From the EDS spectra, sodium calcium, phosphorus, silicon, copper, magnesium and iron are detected. Sodium, calcium, phosphorus and magnesium are from the oil additive. The iron is likely from engine wear that had made its way to the lubricating oil. The copper may be from bearing materials or a background component from the TEM grid. Silicon was present in all samples and may be an artifact of seal materials, dirt that made its way to the intake of the engine or an artifact of the silicon detector used in the EDS. Elemental mapping of the sample area is performed and given in Figure 49.



*Figure 49. STEM+EDS Elemental Mapping of Baseline Sample: (a) O, (b) Cu, (c) Na, (d) Zn, (e) Ca, (f) Overlay*

The oil additives shown in the elemental mapping, calcium, zinc and sodium, are distributed nearly evenly through-out much of the region analyzed, though calcium seems to have some measure of concentration in the more densely populated areas.

Dark and bright field image comparisons for the early start of injection condition were made for over a hundred particles. Again, no ash was detected. An EDS spectra was collected for any region that looked interesting. The results of one such image and the resulting EDS spectra are given in Figure 50.

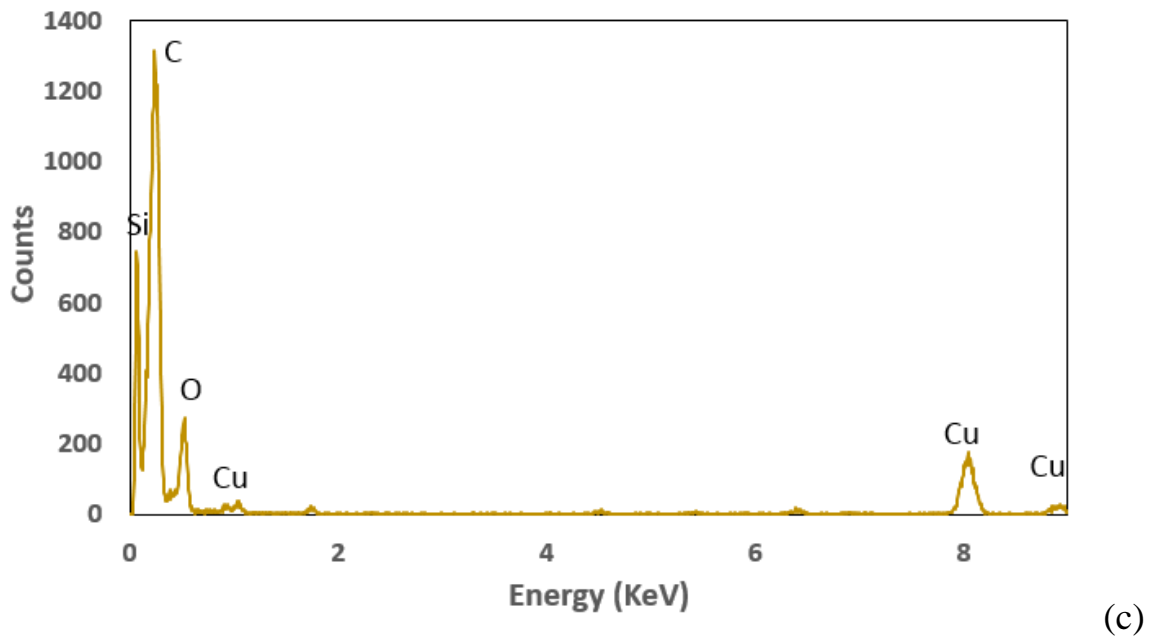
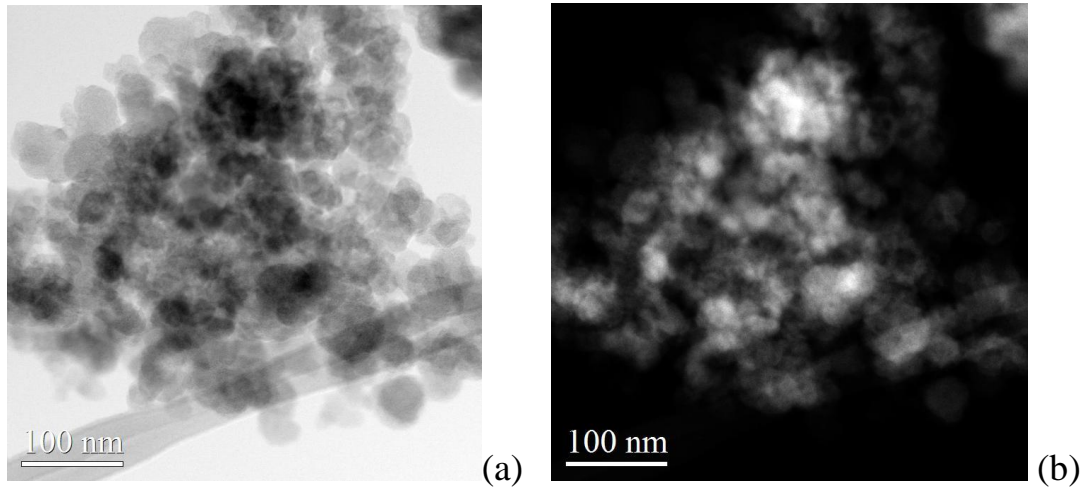


Figure 50. STEM+EDS Results Early SOI Condition 75% Oxidized: (a) Bright Field Image, (b) Dark Field Image, (c) EDS Spectra

No presence of any ash components were detected. The only elements other than oxygen and carbon were copper, possibly tied to the copper grid holding the sample for this case, and the silicon, possibly from dirt in the intake air or from the silicon detector in the EDS.

## 6.3 Summary

Soot samples from the most and least reactive conditions were evaluated for primary particle interaction, nanostructure changes and soot-ash interactions following partial oxidation at 40% and 75%.

The particles seem to meld into each other and form close contact with each other during the soot oxidation process, as shown in TEM images of primary particles fusing together. In fact, partially oxidized samples formed freestanding soot pellets from the loose powder by which they started in the TGA crucible. In addition, the soot morphology tends to become more disordered with higher observed values of oxygen containing surface functional groups during oxidation, for both conditions analyzed. This was determined qualitatively through TEM images and confirmed quantitatively through  $Sp^3/Sp^2$  bonding ratios and oxygen bonding percentages acquired through XPS analysis and peak deconvolution. No ash was detected through the XPS technique, likely as the levels are below the detection limits for depth and resolution.



Upon analysis with STEM+EDS at the 75% oxidation of the more reactive baseline condition, ash was detected at a much higher rate relative to the 0% oxidation sample. However, no ash was present in the early start of injection condition at 75% oxidation. Within the baseline sample at 75% oxidation, ash particles appear to start navigating toward each other as three distinct ash regions were identified within one imaged soot region. The soot appears to be in close contact with the ash and the ash regions are still separated by soot particles, confirming that the ash is still playing a key role in soot reactivity, even at a late stage of oxidation.



## Chapter 7. Ash Influence on the Oxidation Process

The confirmation of ash, imaging of ash-soot interactions and oxidation characteristics given through the TGA work have led to interesting insight into how the ash may be contributing to the enhanced soot reactivity. Proposed mechanisms are presented in this chapter. It may be noted that previous works have reported ash as a percentage of sample ranging from near 0% to 1.35% for gasoline engines (Choi and Seong 2015), and it may be assumed the levels are similar for this work.

The TGA data of isothermal oxidation at 500 °C will be used for the discussion of these concepts. The rate of change of the normalized mass,  $dm_n/dt$ , as a function of the normalized mass,  $m_n$ , were plotted for the soots from differing operating conditions. In Figure 51, the influence of a very slight amount of ash is reviewed. The early start of injection condition represents the amorphous GDI soot without the presence of ash. Although it is likely some ash is present, the amount must be negligible given the inability to detect ash even at the 75% oxidation state and the observed oxidation similarities to the model soot regarding light off temperature and oxidation rates. The low injection pressure condition represents the amorphous GDI soot with small amounts of ash present, small enough to enhance oxidation but not enough to show unique oxidation characteristics.

-  Ash-Soot Agglomeration
-  Soot Particle Agglomeration

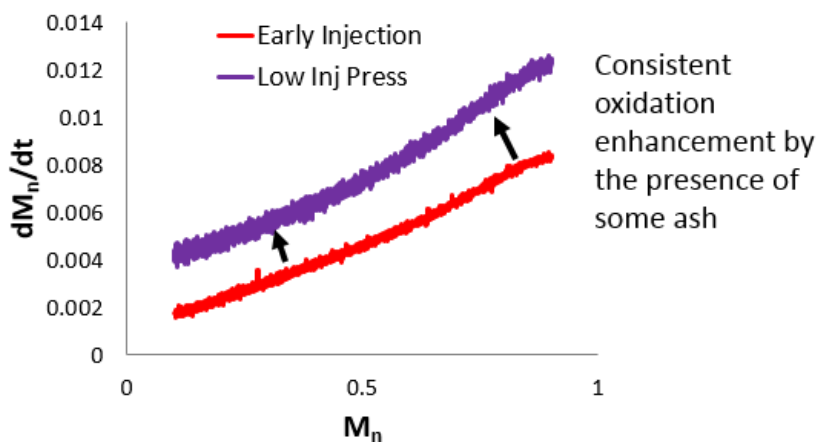
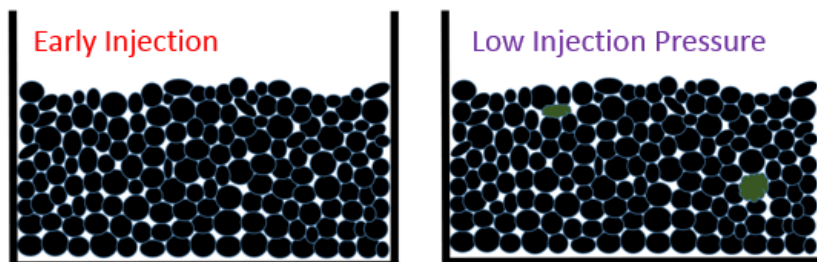


Figure 51. Influence of Small Amounts of Ash on Soot Reactivity

It is proposed that the presence of very small amounts of ash, far less than 1%, enhance oxidation at an even level throughout the entire oxidation process. Furthermore, at this low level of ash, there is little contribution from high rates of soot/ash contact. Though some of the soot must be in close contact with ash, and as there is a slight difference in the change in oxidation rate at the start of oxidation, it is having a potential impact. However, these values must be so small that this contribution to reactivity is negligible and rather the reactivity is enhanced by the presence of the ash, not its contact with the soot.

The late start of injection condition will represent a situation for which more ash is present with respect to the low injection pressure, and for which enough ash is present to perceive unique oxidation characteristics given the interactions of the ash and soot. It is proposed that at this condition enough ash is present to observe the effect of the close contact of soot and ash on changes with the oxidation rate. A discussion on this is given in Figure 52 using plots of the oxidation rate.

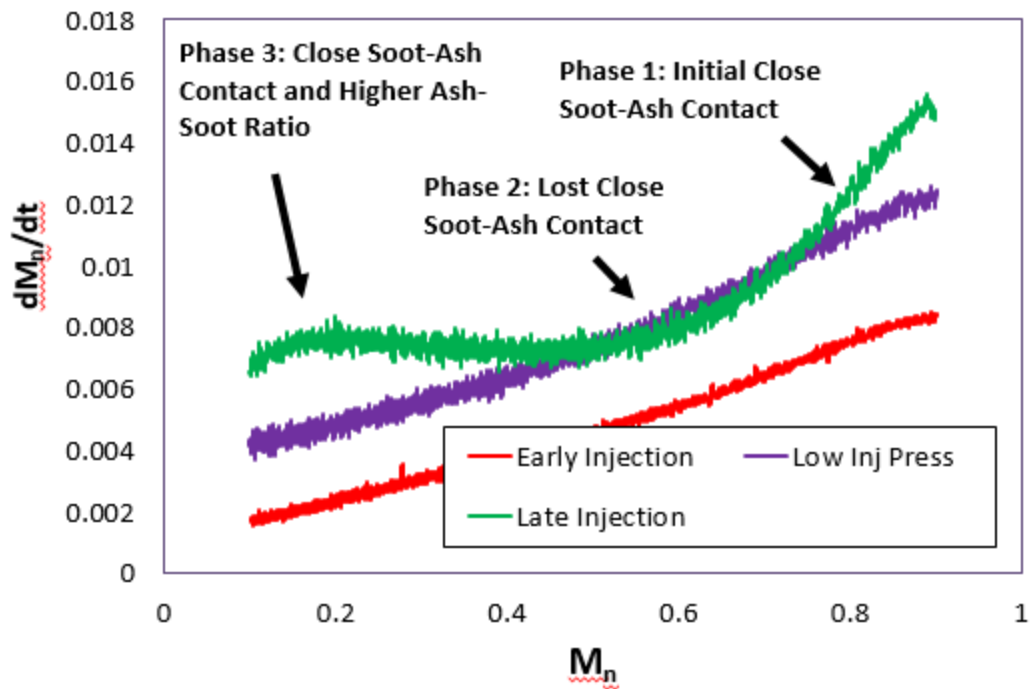


Figure 52. Determination of Phases of Oxidation

There is an enhanced rate of soot burn at both the initial and final stages of the soot oxidation. It is proposed that for early stages of oxidation, there are higher rates of close ash-soot contact, where reactivity is significantly enhanced. As oxidation proceeds, this close contact is removed as the soot in contact with the ash oxidizes. In research works reviewing the impact of

fuel doped with calcium metals, among others, on diesel soot oxidation a clear two stage oxidation was observed. The rate of the second stage was much slower than the first and consistent despite changes in the amount or type of metal added to the fuel (Miyamoto, Hou and Ogawa 1988). It was determined that the first stage was a rapid oxidation process derived from close soot-ash contact while the second slower stage was a result of the loss in soot-ash contact as the soot near the calcium particles was oxidized. This same dynamic is likely occurring for these gasoline soot particles.

However, the third phase of oxidation was not observed in the previous works mentioned. After the close contact is lost and oxidation continues, the soot particles begin to gravitate towards each other, re-forming close contact with the ash and soot as the particles meld into each other propelled by high values of “interparticle attractive forces”. This time there is close contact of the ash to soot as well as higher ash to soot ratios as compared to the early stages of the oxidation process, thus shifting the oxidation rate to a higher value. A value that continues to climb as ash-soot contact remains close and the ash-soot ratio increases due to soot oxidation. It seems likely the ash megastructures seen at the end of oxidation by other works (Sappok, Govani, et al. 2013) will not form until the very end of the oxidation process, leaving much of the ash in contact with soot for the entirety of the oxidation process. The cartoon in Figure 53 illustrates the proposed model describing the soot-ash interaction and ash-soot ratio during the oxidation process.

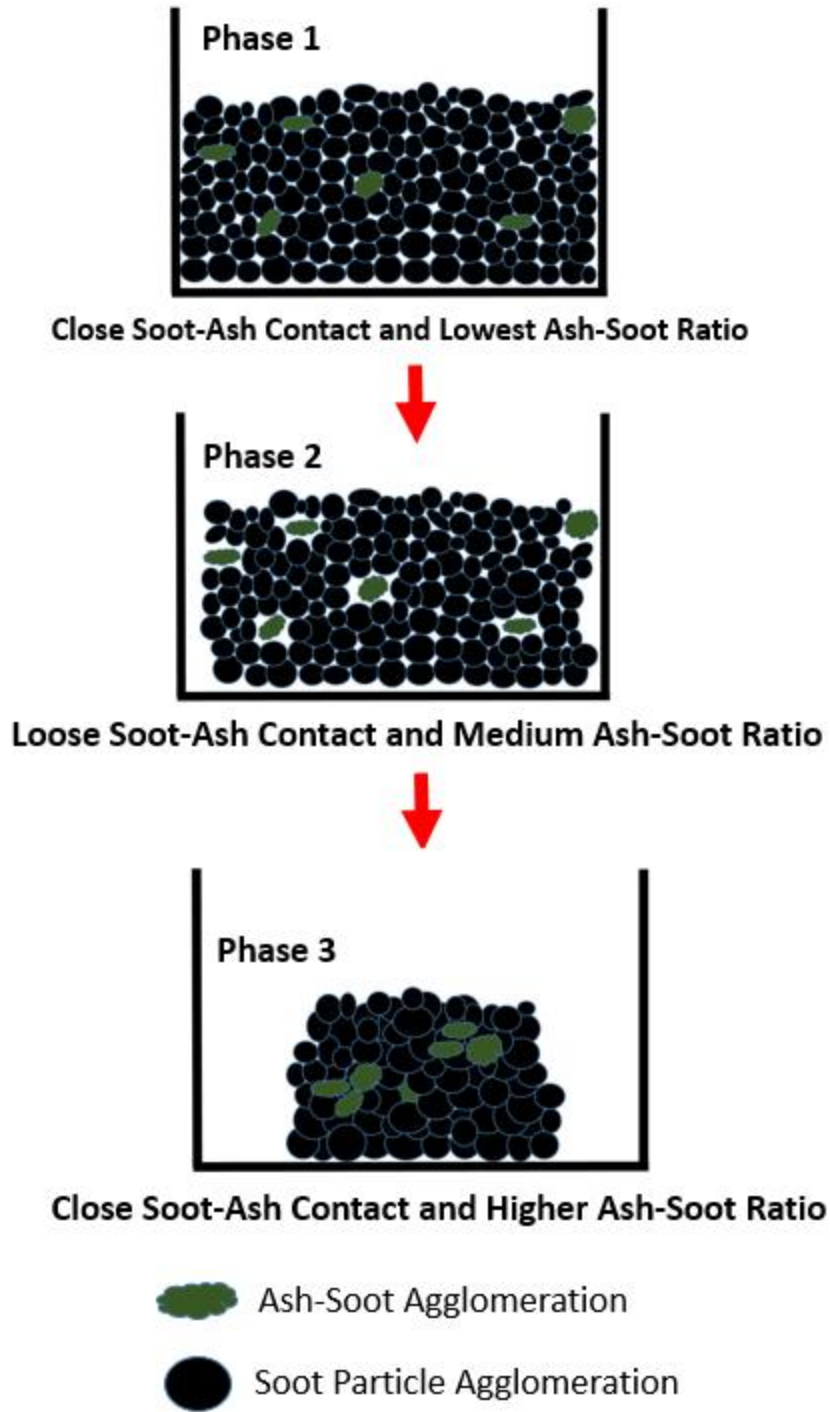


Figure 53. Cartoon Illustrating the Soot-Ash Interaction during the Soot Oxidation Process

The baseline case represents a condition where higher values of ash to soot exist beyond the late start of injection condition. Oxidation rates versus normalized soot mass values are given in Figure 54.

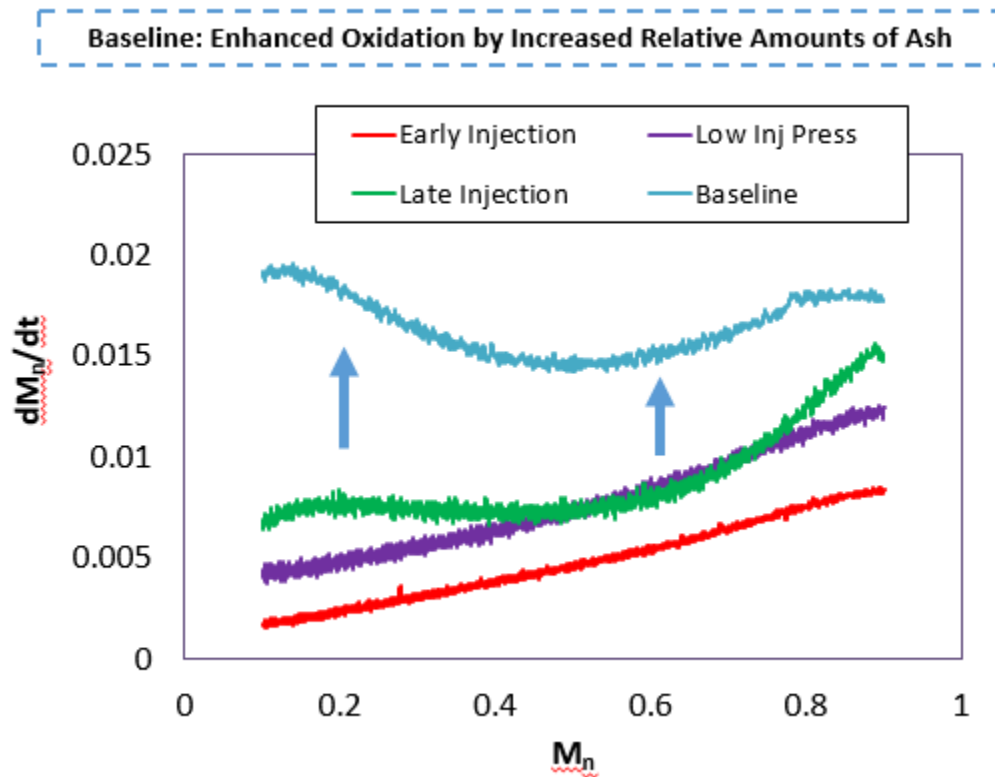


Figure 54. Influence of Baseline Ash Amounts on the Oxidation Process

The baseline condition has a large shift in reactivity but holds the same observed three phases, suggesting the same soot-ash interaction changes are occurring during the oxidation process, just to a higher extent given the higher levels of ash.

It may be interesting to note that the late start of injection condition is most likely producing soot from a fuel film on the cylinder wall, thereby suggesting a potentially higher rate of ash integration and oil consumption. Though it may not be a high enough rate to reach the

baseline condition, it might explain why the phenomenon is present for the late start of injection and not for the low injection pressure, as they may have very different ash levels, though still within the trend mentioned through-out this work.

## Chapter 8. Conclusions

As gasoline particulate filters gain a presence in the automotive sector due to inadequate fuel/air mixing and stringent particulate emissions requirements, it is important the reactivity of the soot collected on the GPF is understood to allow accurate models to be developed. These models are important for understanding passive and active regeneration as both soot dependent filtration efficiency (determined by passive regeneration) and adequate substrate protection during high temperature regeneration events (determined by active regeneration) are important model outcomes.

The impact of fuel injection timing and pressure on soot reactivity were chosen for this work given their strong influence on soot formation rates. Reactivity was explored through isothermal and ramped oxidation events. The following order in reactivity was determined, from most reactive to least reactive: Baseline > Late SOI > Low Inj Press > Early SOI. The light-off temperature was lower, with respect to the model soot, for all conditions except the early start of injection. In addition, linear regressions needed to determine reaction kinetic parameters could be obtained for the early start of injection condition but not for the other conditions as their reaction rates seemed to depend not only on temperature but also on the amount of soot present.



A variety of particulate matter properties influence reactivity and are a product of formation conditions and in-cylinder species. These properties include: nanostructure, surface area, volatile organic fraction, surface functional groups and ash content.

It was determined that under all operating conditions the gasoline soot particles were nascent, immature and possessed very similar nanostructures. It is likely they were formed in low temperature regions of the combustion. This was qualitatively determined with TEM images and quantitatively confirmed through order/disorder peak comparisons with Raman spectroscopy and  $Sp^3/Sp^2$  ratios determined by deconvolution of XPS core scans.

The surface area of the particles was quite different as the operating parameters did produce primary particles of different sizes. With respect to the baseline condition, the late start of injection produced smaller particles, low injection pressure produced both larger and smaller particles and the early start of injection produced much larger particles. The differences in primary particle size resulted in differences in surface area as to be expected. Small particles correlate to a high specific surface area and large particles correlate to a low specific surface area. However, there was no correlation between surface area and reactivity.

Volatile organic fraction (VOF) and surface functional groups (SFG) were similar between the four operating conditions with standard deviations of 2% between conditions for both VOFs and SFGs and average values of 7% and 27% respectively.

Soot reactivity was found to trend well with engine-out soot values. If ash content is assumed a function of engine out soot values, given all operating conditions are at the same speed and load and therefore should have similar oil consumption, then reactivity values are found to trend with ash content. Though determination of ash content was approached with XPS

survey scans, no ash was detected, likely due to the detection limit (1%) and depth limit (3nm – 10nm) of the technique. STEM+EDS was employed to detect ash and review soot and ash interactions at the most and least reactive conditions, baseline and early start of injection respectively. Ash particles were detected for the baseline case but not for the early start of injection condition. This provides further evidence that the ash is the contributor to reactivity and near zero values of ash are present for the case of early injection timing, thus the reason it follows the characteristics of the model soot while the others deviate. The elemental mapping and dark and bright field images from the STEM+EDS determine that the ash is found within concentrated regions of a small percentage of soot particles. In this concentrated region, the ash is in close contact and spread within the soot. These ash rich soot regions possess a uniform distribution of noncombustible oil elements and engine wear metals.

The oxidation process was reviewed through analysis of partially oxidized samples from the most and least reactive conditions, baseline and early start of injection respectively. TEM images were taken during the oxidation process to capture nanostructure evolution. The particles become more amorphous in appearance and possess increasing levels of oxygen containing surface functional groups during the oxidation process. This was determined through deconvolution of bonding within the C 1s core scans taken with the XPS. This may indicate the inner portion of the gasoline soot particles are more amorphous in nature and contain significant levels of matrix bound organics.

The primary particles appear to grow during oxidation as they meld into each other, forming non-spherical larger particles. In fact, the initial loose soot powder placed in the TGA

crucible formed a “free-standing carbon pellet” when partially oxidized. It is proposed that high soot-soot “attractive interaction forces” draw the particles together during oxidation.

STEM+EDS with elemental mapping was again performed to review ash presence and soot-ash interactions. Again, no ash was detected for the early start of injection condition, further confirming it contains near zero ash levels. Various ash-containing areas were detected for the baseline case. At this highly oxidized state, groups of ash embedded soot regions are seen near each other though still separated by soot. The ash is in good contact with the soot and various ash elements are evenly distributed within the soot particles.

Given the oxidation rates from isothermal and ramped oxidation and understandings on soot-ash interactions during and prior to the oxidation process, a new model for the influence of ash on reactivity for GDI soot is presented. This model is applicable for soot from a standard gasoline direct injection engine and covers variations in key levels of ash-soot ratios. GDI soot containing little to no ash matches the oxidation rate profile of a model soot, Printex-U, and reaction rates can be obtained quite easily given the fairly linear rate by which the oxidation rate changes. With the presence of some ash, oxidation is uniformly enhanced as a very small portion of the soot is in close contact with this ash. As ash levels increase, there enters a point when enough of the soot is in close contact with the ash that there is an observable impact on the initial and final oxidation rates. At and beyond this ash level, soot oxidation is marked by three oxidation phases.

Initially, there is an enhanced oxidation rate by soot in close contact with ash. This impact is diminished, and the second phase is entered, as the soot in close contact is oxidized, returning the oxidation rate to a lower, but still higher than if no ash was present, value.

However, as the oxidation process continues, the third phase is entered as the soot particles begin to agglomerate and meld into each other. During this process, the ash is brought back to close contact with the soot particles, and oxidation rates begin to rise. As this process continues, the ash-soot ratio continues to increase thereby causing a continuing rise in the oxidation rate until the oxidation process is complete. This process is the reason that small amount of ash, undetectable by XPS, as would be found in true gasoline engine operation, have such strong influences on soot reactivity.

## Chapter 9. Future Work

As with all research works, there is so much more that could be explored. Further work should be carried out to determine actual ash quantities and the differences in oil consumption rate and ash integration that may occur for different soot formation regions within the combustion chamber. In addition, the influence of fuel properties on soot reactivity should be reviewed, to see if again variations in reactivity are simply a product of soot formation rates.

This work proposes a mechanism, but an understanding of what amounts of ash correspond to the observed transitions in reactivity would be needed for further application of the lessons learned for this work. As the ash amounts are so low, nuclear magnetic resonance and inductively coupled plasma optical emission spectroscopy would be good starting points as these are great techniques for detecting metals and have no limitations regarding sample depth.

Verification of the soot and ash interactions under all soot formation conditions is also of value, as perhaps the findings from the baseline condition may not apply to low injection pressure and early start of injection.

The role of a catalytic coating on enhancing soot oxidation in conjunction with the differences observed in this work are needed as perhaps the enhanced oxidation provided by close contact to the catalyzed surface may enhance reactivity enough that the role of ash is

negligible. This is important as many GPFs are likely to have a catalytic wash coat similar to that of a three-way catalyst.

The determination of this ash effect on operating conditions for diesel engines for which low engine-out soot values is also of interest, to see if the mechanisms presented here are still present and if reactivity is dictated by ash content.

## **Appendices**

### **Appendix A**

#### **Raman Peak Deconvolutions**

Peak deconvolutions from the Raman spectra are given for the other three engine operating conditions not shown within the body of the thesis, low injection pressure, late start of injection and early start of injection. These deconvolutions were performed in the manner specified in [Section 3.6.3](#).

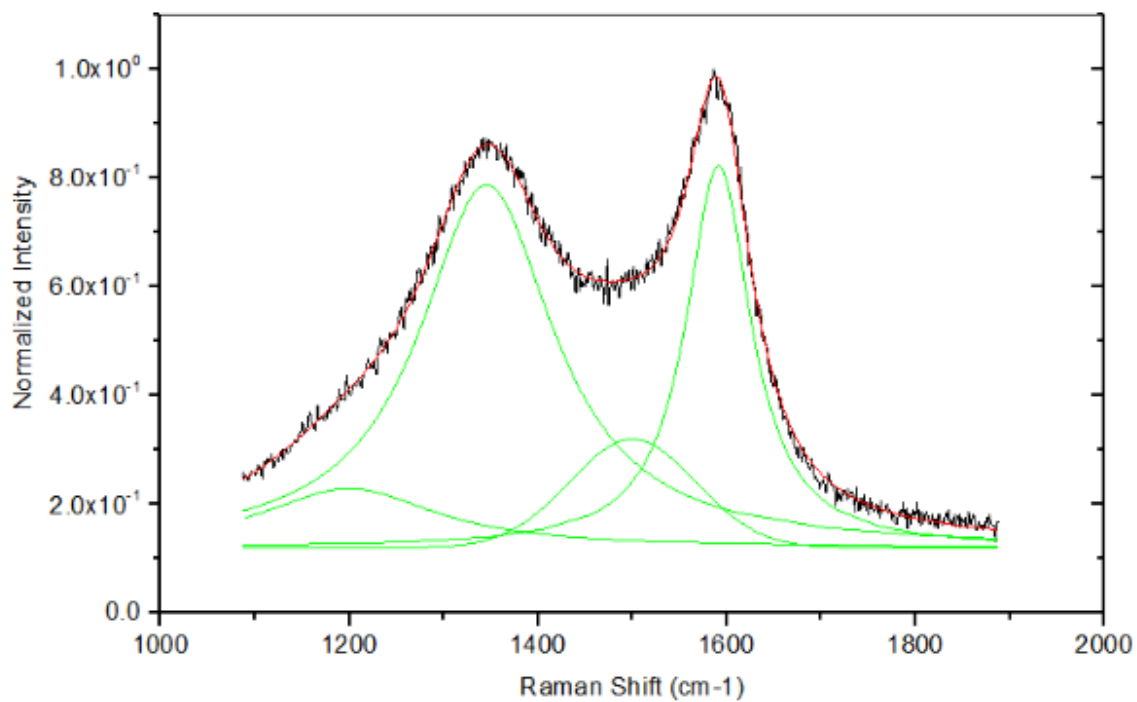


*Figure A- 1. Raman Spectroscopy Peak Deconvolution for Low Injection Pressure*

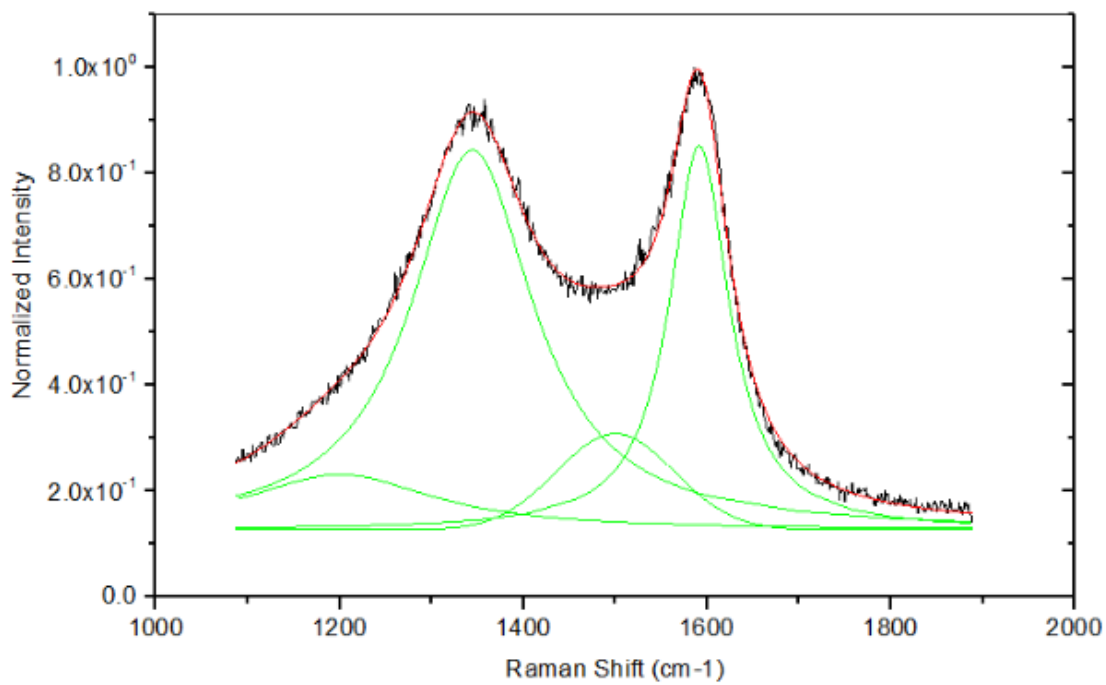


*Figure A- 2. Raman Spectroscopy Peak Deconvolution for Late Start of Injection*



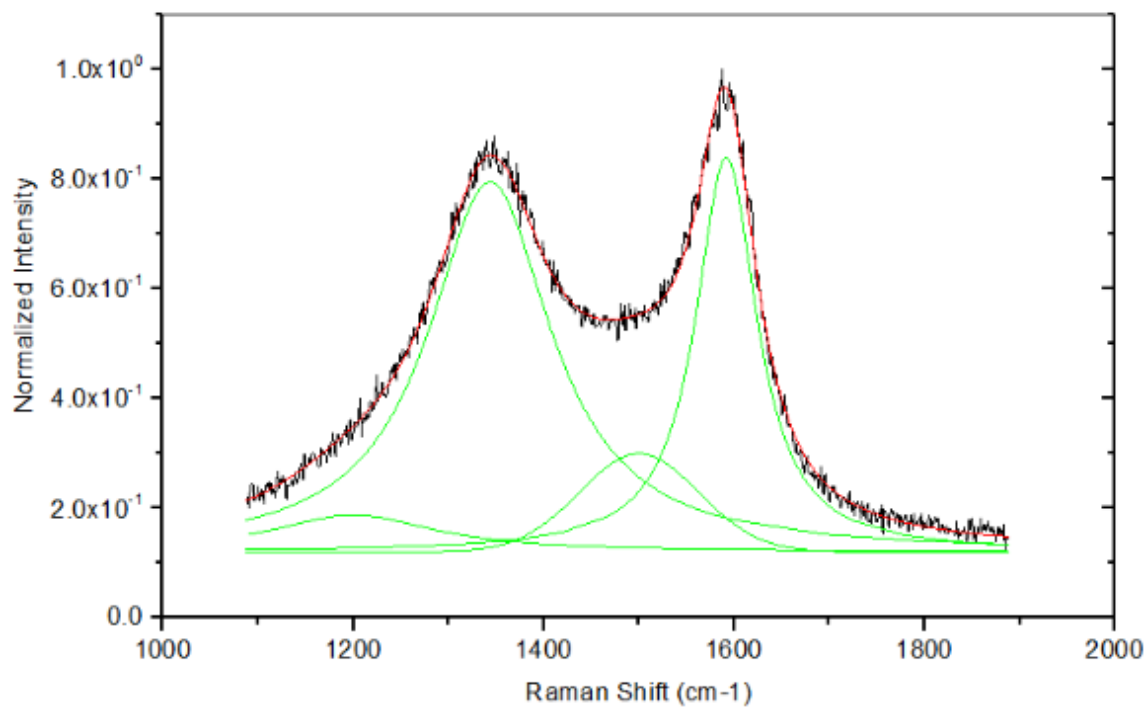
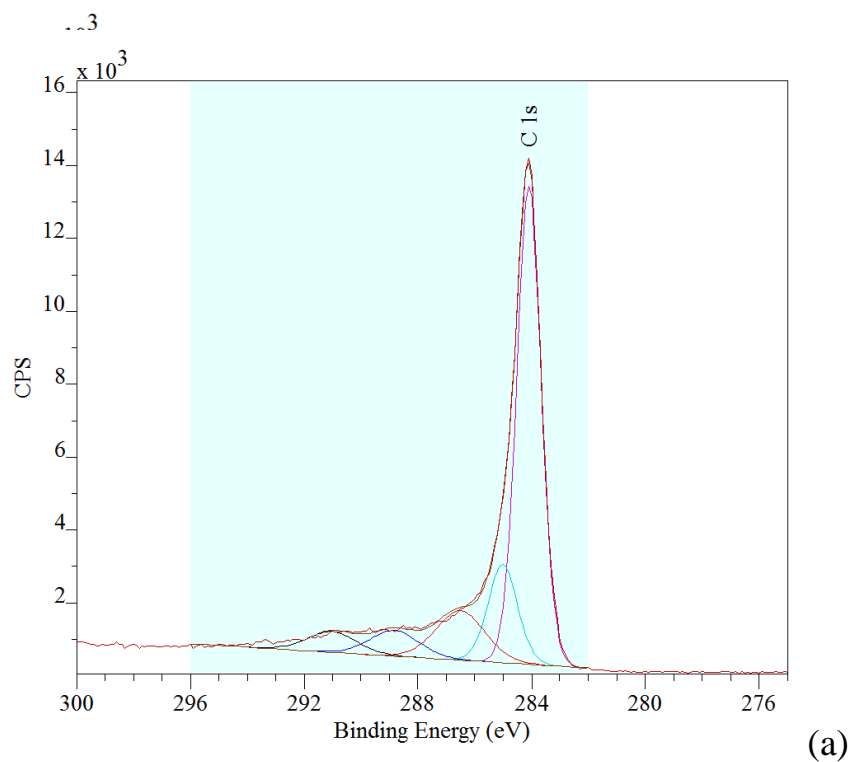


*Figure A- 3. Raman Spectroscopy Peak Deconvolution for Early Start of Injection*

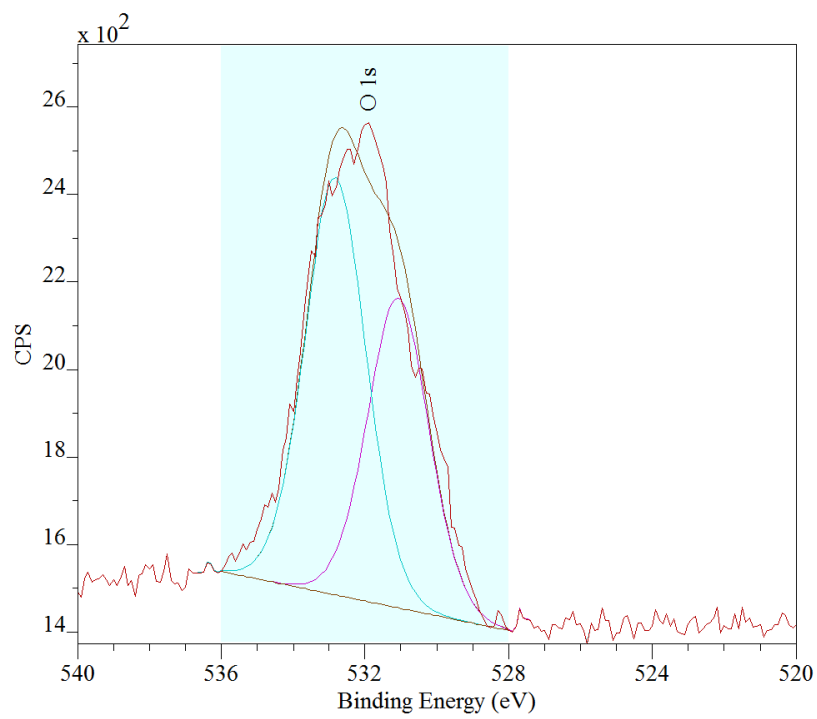
## **Appendix B**

### **XPS Peak Deconvolutions**

Peak deconvolutions are given for the baseline condition.



(a)



(b)

Figure B- 17. XPS Peak Deconvolution for Baseline Condition: (a) C 1s (b) O 1s

## Bibliography

- An, Y, S Teng, Y Pei, J Qin, X Li, and H Zhao. 2016. "An Experimental Study of Polycyclic Aromatic Hydrocarbons and Soot Emissions from a GDI Engine Fueled with Commercial Gasoline." *Fuel* 160-171.
- Biniak, S, G Szymanski, J Siedlewski, and A Swiatkowski. 1997. "The Characterization of Activated Carbons with Oxygen and Nitrogen Surface Groups." *Carbon* 1799-1810.
- Boehm, H.P. 1994. "Some Aspects of the Surface Chemistry of Carbon Blacks and Other Carbons." *Carbon* 32: 759-769.
- Bogarra, M., J. Herreros, A. Tsolakis, A. York, P. Millington, and F. Martos. 2017. "Influence of On-Board Hydrogen and Three Way Catalyst on Soot Nanostructure in Gasoline Direct Injection Engines." *Carbon* 326-336.
- Bosckhorn, H. 1994. *Soot Formation in Combustion: Mechanisms and Models of Soot Formation*. Berlin: Springer - Verlag.
- Cain, J, P Gassman, H Wang, and A Laskin. 2010. "Micro-FTIR Study of Soot Chemical Composition - Evidence of Aliphatic Hydrocarbons on Nascent Soot Surfaces." *Physical Chemistry Chemical Physics*.
- Chan, T., M. Saffaripour, F. Liu, J. Hendren, K. Thomson, J. Kubsh, R. Brezny, and G. Rideout. 2012. "Reducing Particulate Emissions for Future Gasoline Direct Injection Vehicles with a Gasoline Particulate Filter." 16th ETH-Conference on Combustion Generated Nanoparticles.
- Chiang, I.W., B.E. Brinson, A.Y. Huang, P.A. Willis, M.J. Bronikowski, J.L. Margrave, R.E. Smalley, and R.H. Hauge. 2001. "Purification and Characterization of Single-Wall Carbon Nanotubes (SWNTs) Obtained from the Gas-Phase Decomposition of CO (HiPco process)." *Physical Chemistry* 8297-8301.

- Choi, S, and H Seong. 2016. "Lube Oil-Independent Ash Chemistry on Soot Oxidation Reactivity in A Gasoline Direct Injection Engine." *Combustion and Flame* 68-76.
- Choi, S, and H Seong. 2015. "Oxidation Characteristics of Gasoline Direct Injection (GD) engine soot: Catalytic Effects of Ash and Modified Kinetic Correlation." *Combustion and Flame* 2371-2389.
- Christian, V.R., F. Knopf, A. Jaschek, and W. Schindler. 1993. "Eine neue Messmethodik der Bosch-Zahl mit erhohter Empfindlichkeit." *Motortech Z* 16-22.
- Cuesta, A, P Dhamelincourt, J Laureyns, A Martinez-alonso, and J Tascon. 1994. "Raman Microprobe Studies on Carbon Materials." *Carbon* 1523-1532.
- Diesel Filter Materials*. n.d. "Wall-Flow Monoliths."
- Donnet, J.B. 1982. "Structure and Reactivity of Carbons: From Carbon Black to Carbon Composites." *Carbon (Carbon)* 267-282.
- Egerton, R. 2005. *Physical Principles of Electron Microscopy: An Introduction to TEM, SEM and AEM*. Springer.
- Farron, C, N Mathias, D Foster, M Andrie, R Krieger, P Najt, K Narayanaswamy, A Solomon, and A Zelenyuk. 2011. "Particulate Characteristics for Varying Engine Operation in a Gasoline Spark Ignited, Direct Injection Engine." SAE.
- Frenklach, M. 2002. "Reaction Mechanism of Soot Formation in Flames." *Physical Chemistry Chemical Physics* 4 (11): 2028-2037.
- Frenklach, M, and H. Wang. 1990. "Twenty-Third Symposium on Combustion." *The Combustion Institute*.
- Gaddam, C, and R Vander Wal. 2013. "Physical and Chemical Characterization of SIDI Engine Particulates." *Combustion and Flame* 2517-2528.
- Gaddam, C, R Vander Wal, X Chen, A Yezerets, and K Kamasamudram. 2015. "Reconciliation of Carbon Oxidation Rates and Activation Energies Based on Changing Nanostructure." (Carbon).
- H.B., Palmer, and Cullis C.F. 1965. In *The Chemistry and Physics of Carbon*, 265. New York: Marcel Dekker.

- Hackley, V, and A Stefaniak. 2013. "'Real-World' Precision, Bias, and between Laboratory Variation for Surface Area Measurements of a Titanium Dioxide Nanomaterial in Powder Form." (Journal of Nanoparticle Research).
- Hartmann, G. 2007. "Antionette Engines and Aeroplanes."
- Haynes, B., W. Bartok, and A. Sarofim. 1991. "Fossil Fuel Combustion." 261-326. New York: Wiley.
- Howard, J. 1990. "Carbon Addition and Oxidation Reactions in Heterogeneous Combustion and Soot Formation." *The Combustion Institute* (Twenty-Third Symposium): 1107-1127.
- Ishiguro, T, N Suzuki, and Y, Morimoto, H Fujitani. 1991. "Microstructural Changes of Diesel Soot During Oxidation." *Combustion and Flame*.
- Ishiguro, T., N. Suzuki, Y. Fujitani, and H. Morimoto. 1991. "Microstructural Changes of Diesel Soot during Oxidation." *Combustion and Flame* 85: 1-6.
- Israel, G. n.d. "Analyse der Herkunft und Zusammensetzung der Schwebstaubimmission." (VDI Fortschritt-Berichte) 92.
- Johnson, T.V. 2014. "Review of Emerging Trends on Gasoline Emissions Control." *3rd International Conference Advanced Emission Control Concepts for Gasoline Engines*. Dusseldorf.
- Jung, H, D Kittleson, and M Zachariah. 2003. "The Influence of Engine Lubricating Oil on Diesel Nanoparticle Emissions and Kinetics of Oxidation." SAE.
- Kamp, C, A Sappok, Wang, W Bryk, A Rubin, and V Wong. 2014. "Direct Measurements of Soot/Ash Affinity in the Diesel Particulate Filter by Atomic Force Microscopy and Implications for Ash Accumulation and DPF Degredation." SAE.
- Kandas, A., I. Senel, Y. Levendis, and A. Sarofim. 2005. "Soot Surface Area Evolution During Air Oxidation as Evaluated by Small Angle X-Ray Scattering and CO<sub>2</sub> Adsorption." *Carbon* 241-251.
- Keifer, J. R., M. Novicky, M. S. Akhter, A. R. Chughtai, and D. M. Smith. 1981. "The Nature and Reactivity of the Elemental Carbon (Soot) Surface as Revealed by the Fourier Transformed Infrared (FTIR) Spectroscopy." *SPIE* 184-188.
- Kroto, H.W., J.R. Heath, S.C. O'Brien, R.F. Curl, and R.E. Smalley. 1985. "C<sub>60</sub>: Buckminsterfullerene." *Nature* (Nature) 162-165.

- Lakshminarayanan, R, H Toghiani, and C Pittman. 2004. "Nitric Acid Oxidation of Vapor Grown Carbon Nanofibers." *Carbon* 2433-2442.
- Lall, A., W. Rong, L. Madler, and S. Friedlander. 2008. "Nanoparticle Aggregate Volume Determination by Electrical Mobility Analysis: Test of Idealized Aggregate Theory Using Aerosol Particle Mass Analyzer Measurements." *Journal of Aerosol Science* 39: 403-417.
- Lambert, C, M Bumbaroska, D Dobson, J Hargas, J Pakko, and P Tennison. 2016. "Analysis of High Mileage Gasoline Exhaust Particulate Filters." *SAE Int. J. Engines* 9 (2).
- Lapuerta, M, F Martos, and J Herreros. 2007. "Effect of Engine Operating Conditions on the Size of Primary Particles Composing Diesel Soot Agglomerates." *Journal of Aerosol Science*.
- Lee, K, H Seong, S Sakai, M Hageman, and D Rothamer. 2013. "Detailed Morphological Properties of Nanoparticles from Gasoline Direct Injection Engine Combustion of Ethanol Blends." *SAE 2013-24-0185*.
- Lee, S, Y Jung, Y Kim, H Muramatsu, K Teshima, S Oishi, and M Endo. 2009. "Optical Spectroscopic Studies of Photochemically Oxidized Single-Walled Carbon Nanotubes." *Nanotechnology*.
- Leidenberger, U., W. Muhlbauer, S. Lorenz, S. Lehmann, and D. Bruggemann. 2012. "Experimental Studies on the Influence of Diesel Engine Operating Parameters on Properties of Emitted Soot Particles." *Comb. Sci. and Tech.* 184: 1-15.
- Liati, A, D Schreiber, P Dimopoulos, Y Arroyo, R Dasilva, and A Spiteri. 2016. "Electron Microscope Characterization of Soot Particulate Matter Emitted by Modern Direct Injection Gasoline Engines." *Combustion and Flame* 307-315.
- Liati, A, P Dimopoulos, D Schreiber, V Zelenay, and M Ammann. 2013. "Variations in Diesel Soot Reactivity along the Exhaust After-Treatment System, Based on the Morphology and Nanostructure of Primary Soot Particles." *Combustion and Flame* 671-681.
- Majewski, W. A. 2013. "Diesel Particulate Filters." *Dieselnet*, January 2018: <https://www.dieselnet.com/tech/dpf.php>.
- Mayer, A, A Ulrich, J Czerwinski, and J Mooney. 2010. "Metal-Oxide Particles in Combustion Engine Exhaust." SAE.
- McKee, D.W., C.L. Spiro, and E.J. Lamby. 1984. "The Inhibition of Graphite Oxidation by Phosphorous Additive." *Carbon* 3 (22): 285-290.

- Miyamoto, N, Z Hou, and H Ogawa. 1988. "Catalytic Effects of Metallic Fuel Additives on Oxidation Characteristics of Trapped Diesel Soot." SAE.
- Miyamoto, N, Z Hou, H Ogawa, and T Murayama. 1987. "Characteristics of Diesel Soot Suppression with Soluble Fuel Additives." SAE.
- Miyashita, K, Y Fukuda, Y Shiozaki, K Kondo, T Aizawa, D Yoshikawa, D Tanaka, and A Teraji. 2015. "TEM Analysis of Soot Particles Sampled from Gasoline Direct Injection Engine Exhaust at Different Fuel Injection Timings." *SAE 2015-01-1872*.
- Mohankumar, S., and P. Senthikumar. 2017. "Particulate Matter Formation and Its Control Methodologies for Diesel Engine: A Comprehensive Review." *Renewable and Sustainable Energy Reviews*.
- Myung, C. L., and S. Park. 2012. "Exhaust Nanoparticle Emissions from Internal Combustion Engines: A review." *Int. J. Automotive Technology* 9-22.
- Neeft, J, M Makkee, and J Moulijn. 1996. "Metal Oxides as Catalysts for the Oxidation of Soot from Diesel Exhaust Gases. I. An Exploratory Study." (Applied Catalysis B: Environmental).
- Neeft, J, M Makkee, and J.A. Moulijn. 1996. "Catalysts for the Oxidation of Soot from Diesel Exhaust Gases. I. An Exploratory Study." *Chemical Engineering* 2 (64): 295-302.
- Neoh, K., J. Howard, and A. Sarofim. 1984. "Effect of Oxidation on the Physical Structure of Soot." *Twentieth International Symposium on Combustion*. Pittsburgh: The Combustion Institute. 951-957.
- Nicolin, P., D. Rose, F. Kunath, and T. Boger. 2015. "Modeling of the Soot Oxidation in Gasoline Particulate Filters." *SAE 2015-01-1048*.
- Northrop, W, S Bohac, J Chin, and D Assanis. n.d. "Comparison of Filter Smoke Number and Elemental Carbon Mass from Partially Premixed Low Temperature Combustion in a Direct-Injection Diesel Engine." (ASME Journal of Engineering for Gas Turbines and Power).
- Oktem, B, M Tolocka, B Zhao, H Wang, and M Johnston. 2005. "Chemical species associated with the early stage of soot growth in a laminar pre-mixed ethylene-oxygen-argon flame." *Combustion and Flame* 364-373.
- Plee, S., and J. S. MacDonald. 1980. "Some Mechanisms Affecting the Mass of Diesel Exhaust Particulate Collected Following a Dilution Process." *SAE Technical Paper*. SAE.



- Plomp, A, D Su, K de Jong, and J Bitter. 2009. "On the Nature of Oxygen Containing Surface Groups on Carbon Nanofibers and Their Role for Platinum Depositions: an XPS and Titration Study." *The Journal of Physical Chemistry* 9865-9869.
- Radovic, L., P. Walker, and R. Jenkins. 1983. "Importance of Carbon Active Sites in the Gasification of Coal Chars." *Fuel* 62: 849-856.
- Sadezky, A, H Muckenhuber, H Grothe, R Niessner, and U Poschl. 2005. "Raman Microspectroscopy of Soot and Related Carbonaceous Materials: Spectral Analysis and Structural Information." *Carbon* 1731-1742.
- Sappok, A, and V Wong. 2007. "Detailed Chemical and Physical Characterization of Ash Species in Diesel Exhaust Entering Aftertreatment Systems." SAE Technical Paper .
- Sappok, A, I Govani, C Kamp, Y Wang, and V Wong. 2013. "In-Situ Optical Analysis of Ash Formation and Transport in Diesel Particulate Filters during Active and Passive DPF Regeneration Processes." SAE.
- Schwan, J, S Ulrich, V Batori, H Ehrhardt, and S Silva. 1996. "Raman Spectroscopy on Amorphous Carbon Films." *Journal of Applied Physics* 440-447.
- Schwarze, P., J. Ovrevik, M. Lag, M. Refsnes, P. Nafstad, R. Hetland, and E. Dybing. 2006. "Particulate Matter Properties and Health Effects: Consistency of Epidemiological and Toxicological Studies." *Hum. Exp. Toxicol.* 25: 559-579.
- Seo, J., W. Park, and M. Lee. 2012. "The Best Choice of Gasoline/Diesel Particulate Filter to Meet Future Particulate Matter Regulations." *SAE 2012-01-1255*.
- Seong, H., K. Lee, and S. Choi. 2013. "Effects of Engine Operating Parameters on Morphology of Particulates from a Gasoline Direct Injection (GDI) Engine." *SAE 2013-01-2574*.
- Smith, M, L Scudiero, J Espinal, J McEwen, and M Garcia-Perez. 2016. "Improving the Deconvolutions and Interpretation of XPS Spectra from chars by ab initio Calculations." *Carbon* 155-171.
- Sokolov, S, E Kelm, R Milovanow, D Abdullaev, and L Sidorov. 2016. "Non-Destructive Determination of Thickness of the Dielectric Layers using EDX." Proceedings of the International Society for Optical Engineering.
- Song, J, M Alam, A Boehman, and U Kim. 2006. "Examination of the Oxidation Behaviour of Biodiesel Soot." *Combustion and Flame* 589-604.

- Song, J., M. Alam, A. Boehman, and U. Kim. 2006. "Examination of the Oxidation Behavior of Biodiesel Soot." *Combustion and Flame* 589-604.
- Spiess, J, K Wong, J Richter, and R Klingmann. 2013. "Investigations of Emissions Control Systems for Gasoline Direct Injection Engines with a Focus on Removal of Particulate Emissions." *Top Catalysis* (56): 434-439.
- Stanmore, B, J Brilhac, and P Gilot. 2001. "The Oxidation of Soot: A Review of Experiments, Mechanisms and Models." *Carbon* 2247 - 2268.
- Strzelec, A, R Vander Wal, S Lewis, T Toops, and C Daw. 2017. "Nanostructure and Burning Mode of Light-Duty Diesel Particulate with Conventional Diesel, Biodiesel and Intermediate Blends." (*International Journal of Engine Research*) 18.
- Su, J., W. Lin, J. Sterniak, M. Xu, and S. Bohac. 2014. "Particulate Matter Emission Comparison of Spark Ignition Direct Injection (SIDI) and Port Fuel Injection (PFI) Operation of a Boosted Gasoline Engine." *Journal of Engineering for Gas Turbines and Power*.
- Sun, C. 2017. "Nanostructure and Reactivity of Soot Produced from Partially Premixed Charge Compression Ignition (PCCI) Combustion and Post Injection." *PhD. Thesis University of Michigan - Ann Arbor*.
- Tanuma, S, T Shiratori, T Kimura, K Goto, S Ichimura, and C Powell. 2005. "Experimental Determination of Electron Inelastic Mean Free Paths in 13 Elemental Solids in the 50 to 5000 eV Energy Range by Elastic-Peak Electron Spectroscopy." *Surface and Interface Analysis*.
- Vander Wal, R, and A Tomasek. 2003. "Soot Oxidation Dependence Upon Initial Nanostructure." *Combustion and Flame* 1-9.
- Vander Wal, R, V Bryg, and M Hays. 2011. "XPS Analysis of Combustion Aerosols for Chemical Composition, Surface Chemistry and Carbon Chemical State." *Analytical Chemistry* 1924-1930.
- Vander Wal, R, Vander, and A. Tomasek. 2004. "Soot Nanostructure: Dependence Upon Synthesis Conditions." *Combustion and Flame* 129-140.
- Vander Wal, V, A Yezerets, and N Currier. 2007. "HRTEM Study of Diesel Soot Collected from Diesel Particulate Filters." (*Carbon*) 45.
- Walker, P. L. 1990. "Carbon: An Old but New Material Revisited." *Carbon* 28: 261-279.

- Wild, U, N Pfander, and R Schlogl. 1997. "Species Analysis of Automotive Carbon Particles: Application of XPS for Integral Analysis of Filter Samples." *Fresenius J Anal Chemistry* 420-428.
- XPS, Casa. 2013. "XPS Spectra."
- Yang, S, Y Yang, H Peng, G Wang, G Ding, and X Xiaoming. 2017. "Insights into the Oxidation Mechanism of Sp<sup>2</sup>-Sp<sup>3</sup> Hybrid Carbon Materials." *Langmuir*.
- Ye, P., C. Sun, M. Lapuerta, J. Agudelo, R. Vander Wal, A. Boehman, T. Toops, and S. Daw. 2016. "Impact of rail pressure and biodiesel fueling on the particulate morphology and soot nanostructure from a common rail turbocarged direct injection diesel engine." *International J. of Engine Research* 193-208.
- Yehliu, K, R Vander Wal, and A Boehman. 2011. "Development of an HRTEM Analysis Method to Quantify Carbon Nanostructure." *Combustion and Flame* 1837-1851.
- Yue, Z, W Jiang, L Wang, S Gardner, and C Pittman. 1999. "Surface Characterization of Electrochemically Oxidized Carbon Fibers." *Carbon* 1785-1796.
- Zhang, S., and W. McMahon. 2012. "Particulate Emissions for LEV II Light Duty Gasoline Direct Injection Vehicles." *SAE Technical Paper 2012-01-0442*.
- Zhao, F., M.C. Lai, and D. Harrington. 1999. "Automotive Spark Ignited Direct Injection Gasoline Engines." *Progress in Energy and Combustion Science* 437 - 562.
- Zhong, D, S He, P Tandon, and M Moreno. 2012. "Measurement and Prediction of Filtration Efficiency Evolution of Soot Loaded Diesel Particulate Filter." SAE.
- Zhou, J, Z Sui, J Zhu, P Li, D Chen, Y Dai, and W Yuan. 2007. "Characterization of Surface Oxygen Complexes on Carbon Nanofibers TPD, XPS and FTIR." *Carbon* 785-796.
- Zhu, J, K Lee, A Yozgatligil, and M Choi. 2005. "Effects of Engine Operating Conditions on Morphology, Microstructure and Fractal Geometry of Light-Duty Diesel Engine Particulates." *Proceedings of the Combustion Institute*.